

Adsorption and Catalytic Oxidation Reaction  
on Platinum-Group Metal Surfaces under  
Near Ambient Pressure Conditions

March 2016

Ryo Toyoshima

# Adsorption and Catalytic Oxidation Reaction on Platinum-Group Metal Surfaces under Near Ambient Pressure Conditions

A thesis submitted in partial fulfilment of the requirements for the degree  
of Doctor of Science (Hakase (Rigaku))



**Keio University**

Graduate School of Science and Technology  
School of Fundamental Science and Technology

March 2016

Ryo Toyoshima

# Abstract

Catalytic reactions proceeding on Pt-group metal (PGM) surfaces have been used for various applications in the modern society. However, the reaction mechanisms of not a few PGM catalysts have not been fully understood yet at the atomistic level. One of the most critical issues to be overcome for achieving the understanding is that most of the surface science techniques used so far need ultrahigh vacuum (UHV) environments, though the real catalysts usually operate under atmospheric or higher pressure conditions (so-called pressure gap). In this thesis, by means of new surface science techniques applicable to near realistic conditions, adsorption and catalytic oxidation reactions of simple molecules, i.e., carbon monoxide (CO) and nitric oxide (NO), on PGM and its alloy surfaces were studied over a pressure range from UHV to sub-Torr. As a result, high-pressure-induced adsorption states and catalytically active phases under near ambient pressure conditions were elucidated. This thesis consists of the following five chapters.

## Chapter 1: General Introduction

The scientific background and the aim of this study are described. After an overview of previous studies on heterogeneous catalysis is given, molecule-substrate interactions are explained from several viewpoints such as physical and chemical properties of metal surfaces and molecules. Then advantages of surface science approaches and recently developed in-situ techniques are shortly reviewed. Finally the aim of this study is given.

## Chapter 2: Research Methods

The experimental and theoretical techniques and apparatus employed in the present study (X-ray photoelectron spectroscopy, infrared reflection absorption spectroscopy, low-energy electron diffraction and density functional theory calculations) are explained.

## Chapter 3: Adsorption of Simple Molecules on Platinum-Group Metal Surfaces

Pressure dependence of adsorption state of CO or NO on PGM surfaces, i.e. Pt(111), Rh(111), Pd(111), Pd(100) and Pd(110), was investigated at room temperature. It was revealed that in most of the adsorption systems the adsorption structure is reversibly controlled by background pressure and at elevated pressures high-density phases are formed. CO adsorption on Pd-Au alloy surfaces was also studied and it was found that pressure-induced site-switching takes place, which can be explained in terms of pressure-induced surface free energy.

## Chapter 4: CO Oxidation Reaction on Low-Index Pd Surfaces: Experimental Evidence of an Alternative View for Active Phases

Catalytic oxidation of CO on low-index Pd surfaces under near ambient pressure conditions is described. In-situ observations of CO<sub>2</sub> formation rate and surface states of Pd under various temperatures and pressures reveal that under the most active conditions the Pd surfaces are covered by high-density oxygen phases which can be formed in both metallic and oxide surfaces. The high catalytic activity of the high-density oxygen is an alternative view of active species for CO oxidation under realistic conditions.

## Chapter 5: Concluding Remarks

Conclusions of this thesis and future perspective of mechanistic studies on catalytic reactions are described.



# Contents

<b>Chapter 1</b>	<b>General Introduction</b> .....	1
1.1	Heterogeneous Catalysis.....	1
1.2	Molecule-Surface Interactions.....	3
1.2.1	Surface.....	3
1.2.2	Molecule.....	4
1.2.3	Oxidation.....	7
1.2.4	Alloying.....	8
1.3	In-Situ Surface Science Techniques.....	8
1.3.1	Morphologic Approach.....	8
1.3.2	Spectroscopic Approach.....	9
1.4	Aim of This Thesis.....	12
	References.....	15
<b>Chapter 2</b>	<b>Research Methods</b> .....	19
2.1	X-ray Photoelectron Spectroscopy.....	19
2.2	Infrared Reflection Absorption Spectroscopy.....	22
2.3	Low Energy Electron Diffraction.....	24
2.4	Experimental Apparatus.....	25
2.4.1	Near-Ambient-Pressure X-ray Photoelectron Spectroscopy.....	25
2.4.2	Polarization Modulation Infrared Reflection Absorption Spectroscopy.....	27
2.5	Density Functional Theory.....	29
2.5.1	Basic Theory.....	29
2.5.2	Adsorption Energy.....	30
2.5.3	Surface Free Energy.....	30
2.5.4	Core-Level Shift.....	31
	References.....	32
<b>Chapter 3</b>	<b>Adsorption of Simple Molecules on Platinum-Group Metal Surfaces</b> .....	33
3.1	The Reversible Dense CO Overlayer Formation on Pt(111) Surface.....	33
3.1.1	Introduction.....	33
3.1.2	Experiment and Computational Methodology.....	34
3.1.3	Results and Discussion.....	34
3.1.4	Conclusion.....	40
	References.....	41
3.2	The Irreversible Phase Transition of Adsorbed NO on Rh(111) Surface.....	43
3.2.1	Introduction.....	43

3.2.2 Experimental and Computational Methodology.....	44
3.2.3 Results and Discussions.....	45
3.2.4 Conclusions.....	52
References .....	53
3.3 CO and NO Adsorption on Low-Index Pd Surfaces.....	55
3.3.1 Introduction.....	55
3.3.2 Experimental and Computational Methodology.....	56
3.4.3 Results and Discussions.....	57
3.3.4 Conclusions.....	67
References .....	69
3.4 CO Adsorption on Pd <sub>70</sub> Au <sub>30</sub> (111) Alloy Surface: A Remarkable Enhancement of Top Site Occupation .....	71
3.4.1 Introduction.....	71
3.4.2 Experiment and Computational Methodology .....	72
3.4.3 Results and Discussion .....	72
3.4.4 Conclusions.....	80
References .....	81
Chapter 4 CO Oxidation Reaction on Low-Index Pd Surfaces: Experimental Evidence of An Alternative Reaction Mechanism.....	83
4.1 Introduction .....	83
4.2 Experiment and Computational Methodology.....	84
4.3 Results and Discussion .....	85
8.4 Summary and Discussion .....	97
References .....	99
Chapter 5 Concluding Remarks.....	101
References .....	105
Publications.....	107
Acknowledgements .....	109
Appendix A .....	111
Appendix B .....	113
Appendix C .....	115
Appendix D.....	117

## Chapter 1

### General Introduction

#### 1.1 Heterogeneous Catalysis

The chemical reactions proceeding on surfaces of heterogeneous catalysts play a crucial role in various aspects of human activities; for example, synthesis of useful industrial materials, energy conversion and pollution control, which are prerequisite for conservation and sustainable development of the modern society. Catalysis was first reported as a drastic enhancement of water formation on Pt surfaces by Döbrenner in 1823.<sup>1</sup> The understanding of physical origin of heterogeneous catalysis is one of key issues in surface science and indispensable to improve catalyst performance (i.e. high selectivity, high conversion rate and long life) and thus to promote such important human activities. Figure 1.1 shows a model reaction path of a catalytic surface reaction, where the surface provides a smaller activation-energy path to convert the reactant compound(s) ( $E_a < E_a'$ ). The elementary steps (adsorption, activation, reaction and desorption) proceed in parallel on the surface.

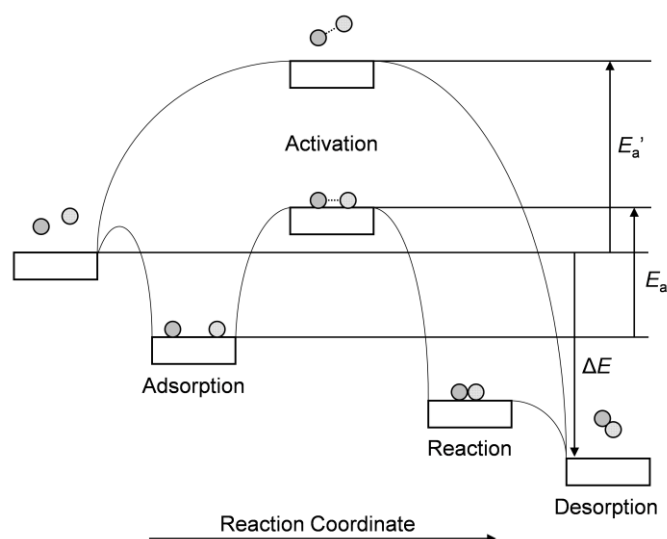


**Figure 1.1.** The schematic reaction paths with and without catalyst. The  $E_a$  and  $E_a'$  mean the activation energy ( $E_a < E_a'$ ), whereas,  $\Delta E$  means heat of formation. The catalytic reaction is described by a combination of several elementary steps.

The three way catalyst (TWC), which is usually made of Pt-group metals (PGMs), is one of the

important heterogeneous catalysts. It is widely used to convert harmful chemical compounds in the exhaust gas to harmless ones at a time, e.g. oxidation of carbon monoxide (CO) to carbon dioxide (CO<sub>2</sub>) and reduction of nitrogen oxides (NO<sub>x</sub>) to N<sub>2</sub>. Oxidation of CO on PGM surfaces has been extensively studied in the field of surface science for the fundamental understanding of the heterogeneous catalysis as well as the technological development.

So far much effort has been dedicated to the understanding of the heterogeneous catalysis at the atomistic level since a pioneering work by Langmuir.<sup>2</sup> He proposed that both of reactants adsorb on the surface, then react and desorb. This process is now called as the Langmuir-Hinshelwood (LH) mechanism. On the other hand, the Eley-Rideal (ER) mechanism is also considered; only one reactant species adsorbs on the surface, then the other reactant in gas phase directly attacks the surface species.<sup>3</sup> A highlight of in-situ observation of heterogeneous catalysis was reported by Ertl and co-workers. They observed the real-time evolution of catalytic reaction and demonstrated that the adsorbed CO and O on Pt(111) surface react on domain boundary by the LH mechanism.<sup>4</sup>

In most of the cases, the reaction mechanism has been studied under the ultrahigh vacuum (UHV) conditions, due to the technical limitation and in order to realize clean well-defined environments. However, realistic industrial catalysts work under atmospheric pressures, besides contaminant species, for instance, CH<sub>x</sub> and water, also coexist. The discrepancy of the pressure condition may be crucial to understand the real catalyst, because a high pressure environment provides a special reactant species on the surface, and/or transforms the catalyst surface itself, which is called as pressure gap problem. The chemical and structural identifications of surfaces before and after catalytic reaction partly elucidates the behavior of the catalysts during the reaction, where the technical constraint is not so significant. However the catalytic surface may not keep unchanged after the reaction (Figure 1.2). To understand the reaction mechanism, it is essentially important to observe the whole reaction processes with an in-situ manner.

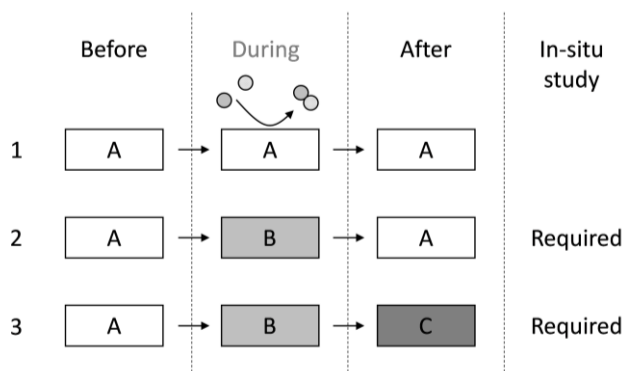


**Figure 1.2.** Possibility of material evolution before, during and after catalytic reactions. If the active surface is only formed under the reaction conditions, the in-situ observation is requested.

Recently, in-situ monitoring studies on CO oxidation under higher pressure conditions have

proposed an alternative reaction path namely Mars-van Kreveln (MvK) mechanism,<sup>5</sup> where the adsorbed oxygen forms the oxide state, then the other reactant (reducing compound) reacts with the lattice oxygen atom as discussed later. The possible reaction mechanisms are summarized in Figure 1.3. One open question is whether the oxidized surface, which is formed under oxidative conditions, is catalytically active or not. Under the UHV conditions, it has been concluded that (surface) oxides are inactive due to the weak interaction with molecules. It is strongly required that the in-situ observations of the catalytic surface reactions are conducted under (near) ambient pressure conditions to overcome the pressure gap issue.

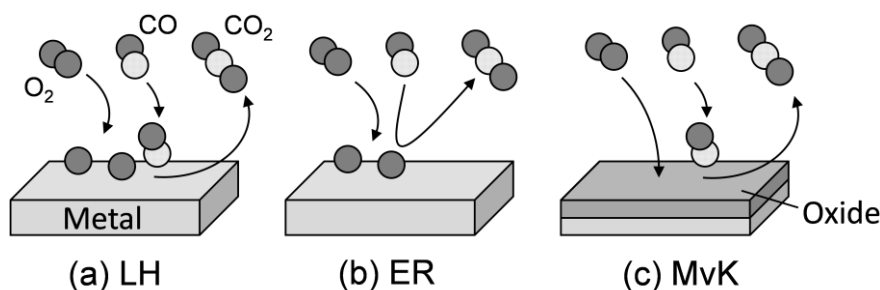


**Figure 1.3.** Reaction mechanisms proposed for CO oxidation reaction. (a) Langmuir-Hinshelwood (LH), (b) Eley-Rideal (ER) and (c) Mars-van Kreveln (MvK).

## 1.2 Molecule-Surface Interactions

### 1.2.1 Surface

The surface provides the adsorption site(s) to the molecule(s), and further exhibits the heterogeneous catalysis. Such a character stems from its unique electronic and structural properties compared to the bulk crystal. A crystal consists of atoms arranged with three-dimensional periodicity. The smallest cell that expresses the whole periodicity of the crystal with translational displacements is called as the unit cell. In the case of PGMs, the three-dimensional unit cell is categorized to the face centered cubic (fcc) cell (Figure 1.4), with one exception of Ru, which is categorized to the hexagonal close-packed (hcp) cell. In this thesis, single crystal surfaces were studied to focus on the fundamental understanding on the ideal model systems.

Surface is the edge of the crystal, where the three-dimensional translational symmetry is unsatisfied. The two-dimensional periodicity of the surface is different depending on how the surface is terminated even for the same crystal. Therefore it is necessary to distinguish the two-dimensional periodicities on the surface. Miller indices is a major method to express the planer periodicity of a surface. The planes are labelled by  $(hkl)$  numbers. The plane, that intersects the three particular vectors along the crystal axes, is intrinsically identified to one, here magnitudes of vectors are defined by

reciprocal values, i.e.  $1/h$ ,  $1/k$  and  $1/l$ . Examples of the low-index surface structures of the (111), (100) and (110) surfaces are shown in Figure 1.4. The coordination numbers of the surface atoms in these surface planes are different. From a thermodynamic point of view, there will be a tendency to minimize this energy by bonding with other molecules. Polycrystalline and particle surfaces are complex of these surfaces.

Even on the single crystal surfaces, there is incompleteness like steps and defects. Figure 1.5 shows local structures found on the surface. These special sites are assumed as active to the chemical reaction due to the low coordination number. In this thesis, the physicochemical property of the flat surfaces are considered, thus the surfaces were initially prepared to minimize the fraction of these incompleteness using adequate physical and chemical methods.

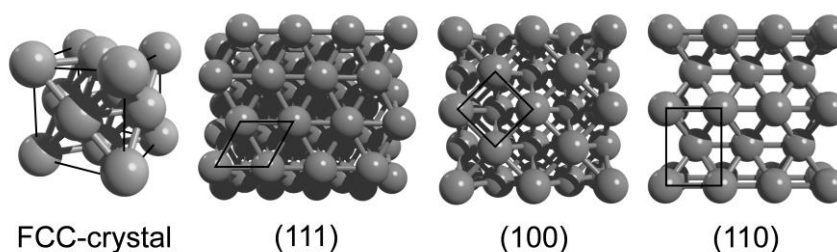


**Figure 1.4.** The unit cell and the low-index (111), (100) and (110) surfaces for fcc crystal.

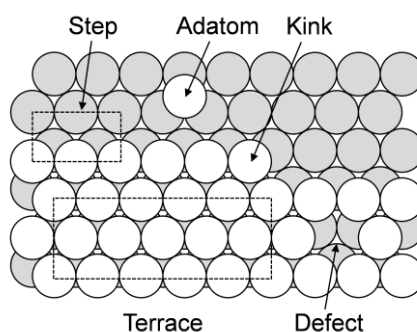


**Figure 1.5.** Local structures formed on the single crystal surfaces.

### 1.2.2 Molecule

The molecules involved in the catalytic reaction come from gas-phase to the surface, then form the chemical bond with surface metal atoms. Therefore, it is important to consider the electronic and geometric structures of the isolated and adsorbed molecules for understanding the behavior on the surface.

The molecule AB is formed, when the wavefunctions of two atom species A and B overlap. The molecular orbitals are often described by the linear combination of atomic orbitals (LCAO). The overlap of two atomic orbitals results in the two molecular orbitals (bonding and antibonding). For instance, Figure 1.6 shows the molecular orbitals of homo- (hetero-) nuclear diatomic molecules. The highest occupied molecular orbital (HOMO) and lowest unoccupied molecular orbital (LUMO) are also crucial to understand the molecule–metal interaction, which are indicated in the figure. The LUMO of O<sub>2</sub> molecule consists of antibonding orbital 2π\*. The molecular orbitals of CO molecule are more complicated, where the s and p atomic orbitals couple with each other, resulting in some additional mixing (sp hybridization). The molecular orbitals are shown in the figure. As a remarkable point, the electron densities of HOMO and LUMO levels of CO molecule are one-sided on the carbon atom. This suggests that the CO molecule adsorbs on the surface with the carbon-end-on geometry.

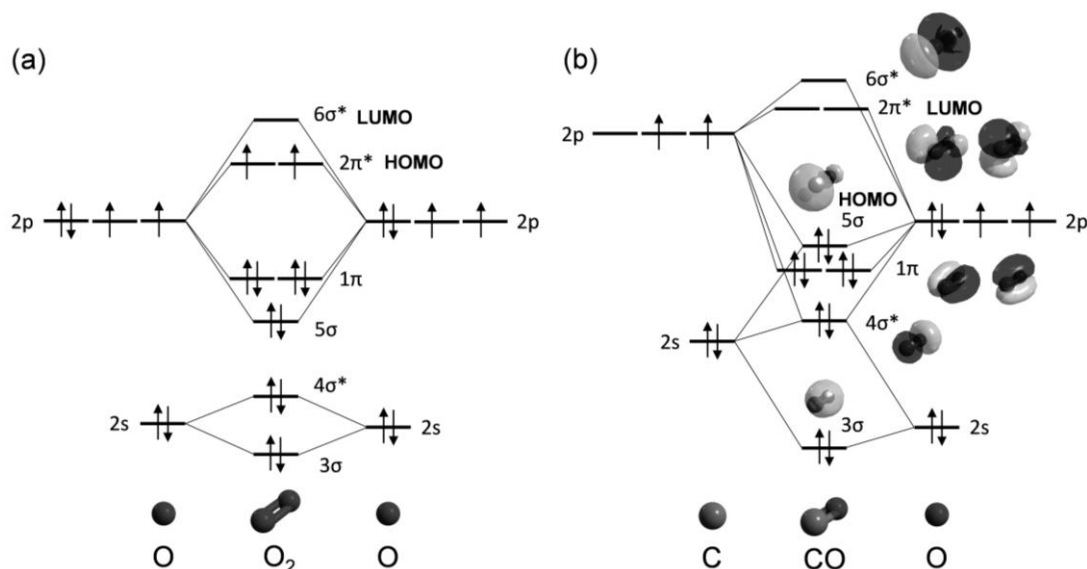


**Figure 1.6.** Molecular orbitals for diatomic molecules; O<sub>2</sub> (a) and CO (b).

The chemical interaction between molecule and metal surface is described in Figure 1.7. When the molecule approaches to the simple metal surface, where the valence structure consists of sp band, there are four types of interactions; HOMO–occupied valence, HOMO–unoccupied valence, LUMO–occupied valence and LUMO–unoccupied valence. Total electron energies are stabilized in every cases, thus the adsorption on the surface is allowed, although the interaction is weak due to its poor spatial overlap. The late transition metals have two types of valence band electrons; sp and d bands. The d band is localized on each metal atom. The interaction with the d band is well represented by orbital–orbital interaction. It results in the partial electron occupation of the antibonding 2π\* orbital,

while the donation from the bonding  $5\sigma$  orbital, leading to a strong interaction between carbon and metal atoms. As a more extreme example, when the  $O_2$  interacts with metal surface, the antibonding  $2\pi^*$  orbital is occupied by the electrons from metal, resulting in the dissociation to the two monoatomic oxygen. It is noted that the center of the gravity of d band is called as d band center, which is a key factor to explain the strengths of the interactions between different molecule–metal systems.<sup>6,7</sup>

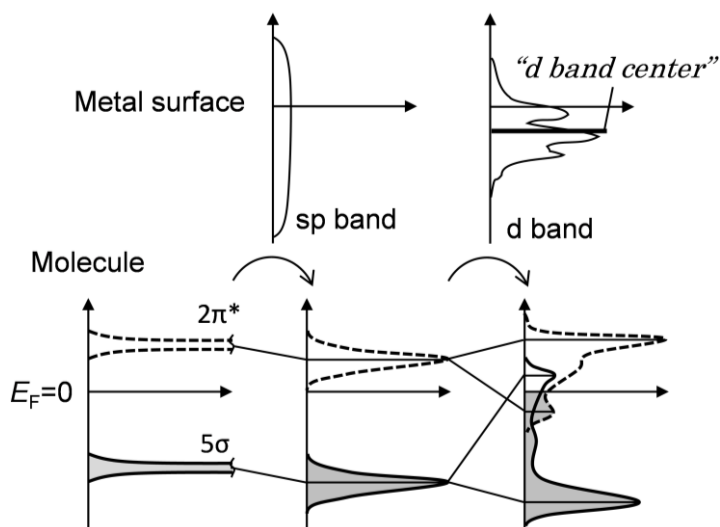


**Figure 1.7.** Schematic description of molecule-surface interaction.

The surface consists of a combination of various local structures as discussed above. Molecules adsorbed on the surface prefer to locate at high symmetry sites, because of the energetic point of view. Typical adsorption sites are shown in Figure 1.8. Here the fcc(111) surface is modeled. To maximize the total of adsorption energy, the adsorbates form various ordered periodic structures on the surfaces depending on the surface coverage. The surface periodicity is expressed by the Wood's notation. Sometimes the solid surface is reconstructed by adsorbates to gain a higher adsorption energy.

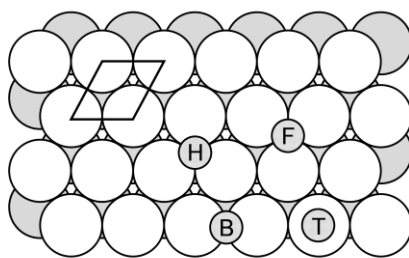


**Figure 1.8.** Possible adsorption sites on a fcc-(111) surface: top (T), bridge (B), hcp-hollow (H) and fcc-hollow (F).

### 1.2.3 Oxidation

O<sub>2</sub> molecules adsorbed on metal surfaces dissociate to the monoatomic O, then form the chemisorbed state. The chemisorbed state has several ordered periodicities depending on surface coverage. The O induced overlayer formation has been extensively investigated on PGM surfaces.<sup>8,9</sup> If enough heat is given from outside, the oxygen-metal interface forms a stronger chemical bond with a large mass transfer, i.e. oxidation. As well known, the oxide has a unique three dimensional crystal lattice due to the strong ionic bond formation (hereafter this is called as bulk oxide).

On single-crystal surfaces, another oxide group has been identified in past two decades. Lundgren et al. found that a well-ordered ultrathin oxide film was formed on Pd(111), when the surface was exposed under a relatively mild oxidation condition. This is so-called surface oxide.<sup>10,11</sup> Similar results were reported on other PGM surfaces.<sup>12-21</sup> The structural and chemical identifications have been conducted using various surface science techniques. Interestingly each surface oxide has a unique two-dimensional periodicity, which is different from the corresponding bulk oxide. It sometimes provides special adsorption sites for adsorbed molecules. The evolution of oxygen-metal interaction is described in Figure 1.9. It has been reported that the CO molecule stably adsorbs on the surface oxide layer formed on Pd(111), although the adsorption energy is smaller than that on the metallic surface.<sup>22</sup>

The chemical reactivity of these surface oxide species are not clear so far. In UHV conditions, the oxide layer is regarded as an inactive species for the catalytic CO oxidation, where the reaction proceeds via the LH mechanism. A remarkable exception is the RuO<sub>2</sub> surface, which shows the higher activity than metallic surfaces.<sup>23</sup> As the results of detailed experimental and theoretical investigations, the origin of the discrepancy comes from the availability of a special adsorption site for O and CO formed on the oxidized surface. On the other hand, under the O<sub>2</sub>-rich feed, for example, under the atmosphere, the oxide species may be formed on the PGM surfaces during the reaction.

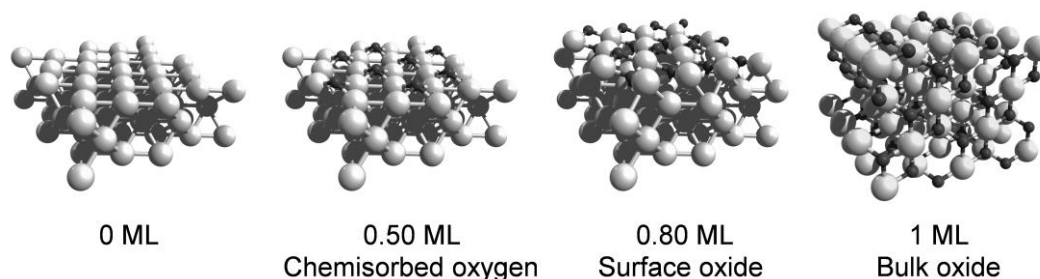


**Figure 1.9.** Evolution of oxygen covered surface depending on the oxygen coverage. Here the metal substrate is modeled by a Pd(100). The small dark and large bright balls indicate O and Pd atoms, respectively. The O surface coverages are estimated in monolayer (ML) scale, with respect to the number of surface Pd atoms.

## 1.2.4 Alloying

Alloying is a major technique to tune the catalyst performance via the modulation of electronic and geometric structure by the presence of second metal element. Alloy materials sometimes exhibit higher catalytic activity than that of monometallic one, therefore are extensively investigated in various research field, for instance, oxygen reduction reaction, chemical synthesis, steam reforming and so on.<sup>24-33</sup> The structure of alloyed surface is now paid much attention to link the catalytic activity and alloying effect.

Alloying is realized when each of the atoms is rather stabilized by the coexistence than the present alone. The stoichiometry can be altered within a certain range. If it is stabilized only at a constant ratio, it is called as intermetallic compound. Furthermore, the stoichiometry of surface layer is often independent from the bulk stoichiometry. In most of the cases, the topmost layer is consisting of more or less chemically inactive species.

The Au–Ni alloy surface is acknowledged as an active catalyst for steam reforming, which has an Au-rich surface layer.<sup>27</sup> As a unique property, the exposure to excess CO leads the surface to the phase separation of Au and Ni due to the formation of Ni carbonyl on the surface.<sup>28</sup> Pd–Au bimetallic catalysts are applied to various catalytic reactions.<sup>29-33</sup> The mixture of Au and Pd can significantly enhance the overall catalytic activity of the reaction. However, the role of alloyed Au had not been elucidated. Goodman and coworkers revealed the origin of ensemble effect of a Pd–Au surface on vinyl-acetate synthesis.<sup>31</sup> They found that the reactivity strongly depended on the Pd concentration of the surface layer; the discrete Pd clusters embedded in Au rich surfaces are the active center of the reaction.

## 1.3 In-Situ Surface Science Techniques

### 1.3.1 Morphologic Approach

Surface science techniques can investigate the atomic scale structure formed on the surface under static/dynamic conditions. Here, in-situ techniques used for studies on the surface morphology are introduced. Low-energy electron diffraction (LEED) is one of the powerful surface science tools to investigate the surface two-dimensional structures. But this is an electron in/electron out technique, thus the incident electron beam and back scattered electron are strongly decayed under higher pressures. On the other hand, X-ray diffraction (XRD) is a photon in/photon out technique and thus is applicable to studies on the surfaces under atmospheric environments. But it is generally regarded as a bulk sensitive method, because it reflects ordered lattice structure of the material. Surface XRD (SXRD) enhances scattering from the surface two-dimensional structure with grazing angle X-ray incidence. The surface periodic structure is identified via the diffraction pattern. Details of experimental setup is described in ref 34. To gain clear diffraction pattern, the surface condition should

be uniformed, thus the technique shows averaged information from the surface. The diffraction along the surface plane gives information equivalent to LEED. It can also scan the depth profile of the catalyst surface. This technique is available to various types of samples such as highly stepped and/or particle surfaces, if it has a certain level of surface periodicity. The evolution of surface chemical phase, e.g. metal or oxide, can be traced under catalytic conditions.<sup>35-39</sup> Catalytic CO oxidation is a typical model reaction for understanding catalytic reaction, therefore some research groups have investigated the system using the SXRD technique. Gustafson et al. demonstrated that the oxide evolution on Pd(100) surface during the catalytic CO oxidation reaction under a realistic pressure conditions using a two-dimensional detector and high energy X-rays.<sup>39</sup> Here, three types of chemical phases are identified during the reaction, e.g. metallic, surface oxide and bulk oxide, with three-dimensional diffraction pattern analyses. Their main conclusion is that the oxide state accelerates the catalytic performance at near realistic environments. Further detailed experiments revealed gradual growth of the oxide layer and its stability under the catalytic conditions.

Scanning tunneling microscope (STM) is a conventional tool for the atomic-scale observation, which provides direct information of surface morphology originating from adsorbates and substrates. This technique utilizes the tunneling effect; when a sharpened metal tip is approached to a conducting sample closely with the nanometer order, an electric current is detected between tip and sample without the direct contact. The amount of the current strongly depends on the distance between tip and sample. The spatial resolution is in the angstrom order, therefore this technique enables to image individual atoms (molecules), which need not be arranged with a periodicity. Nowadays, STM images can be measured over the pressure range from UHV to atmospheric environments.<sup>40-48</sup> Pressure induced surface restructurings have been successively reported. Tao et al. found that high pressure CO exposure to a stepped Pt surface reversibly causes surface restructuring even at room temperature, where triangle-shaped terraces adsorb a dense CO overlayer with a coverage of 1 monolayer.<sup>40</sup> Hendriksen et al. have reported that the surface is oxidized under high O<sub>2</sub> pressures for CO oxidation on Pt and Pd surfaces.<sup>47,48</sup> These studies suggest that the substrate surface are easily rearranged depending on the gas pressure. STM technique bridges between UHV and atmospheric conditions, but the application is limited to conductive well-ordered surfaces. Atomic force microscopy (AFM) technique is an alternative scanning probe under similar pressure conditions, which can image much more realistic (industrial) samples, i.e. particles and/or insulated materials,<sup>49,50</sup> though the spatial resolution becomes less.

### 1.3.2 Spectroscopic Approach

Vibrational spectroscopies (VSs) are adequate for measurements under atmospheric conditions and some of them are sensitive to adsorbates. Especially, sum frequency generation (SFG)-VS<sup>51-55</sup> and

polarization modulation infrared reflection absorption spectroscopy (PM-IRAS)<sup>56-58</sup> are widely applied for surface science, because of its high surface selectivity. These techniques give information on chemical bonds of adsorbates and adsorption site on the surface. SFG is a kind of non-linear optical effects and can be used as an intrinsically surface sensitive technique, because the surface does not have the reversal symmetry. Here the two incident lights (visible and mid infrared) are spatially and temporally overlapped on the surface, and the resultant SFG light is detected. IRAS is a conventional surface science technique to observe vibrational modes of adsorbates. However, the gas-phase contribution becomes dominant at higher pressure conditions. The switching p- and s-polarized infrared light exposed to the surface during the measurement enables to extract signals from the surface species only even at higher pressures (PM method). The spectrum obtained from p-polarized light contains both of surface and gas-phase information, whereas the spectrum from s-polarized light contains only gas-phase information. Electron energy loss spectroscopy (EELS) is also used in traditional surface science studies to measure adsorbate on the surface. However it is an electron probe technique, therefore the attenuation effect by background gases is crucial.

Increasing of the background pressure sometimes causes chemical and/or physical effects on exposing molecule. Hess et al. have reported the pressure induced dimer formation on NO/Pd(111) system at 400 mbar NO pressure at 300 K.<sup>57</sup> Gao et al. found that the CO adsorption site on Pd–Au alloy changes between UHV and atmospheric conditions under the catalytic oxidation condition.<sup>58</sup> These in-situ measurements clearly demonstrate that the adsorption state of molecules on the surface drastically changes depending on background pressure.

X-ray photoelectron spectroscopy (XPS) is a photon in/electron out measurement. This technique provides information on chemical state of molecule and substrate surface at once, thus is a powerful tool for understanding of catalytic reactions on the surfaces. The incident X-rays to the surface excite core-level electrons to the vacuum. By analyzing kinetic energies of emitted electrons, it is possible to investigate the chemical environment and depth profile of the interested element. The detailed principle of measurement is described later. It can access both of the well-defined single crystals and (quasi-) industrial materials. However it is intrinsically unfitted for in-situ monitoring under high background pressure conditions, since the electrons are easily scattered by gas molecules. However recent technical developments allow us measurements under pressures from UHV to 100 Torr by using the multiple-stage differential pumping and electron lens systems; near-ambient-pressure (NAP-) XPS. Synchrotron radiation and lab-X-ray source based NAP-XPS setups have been built up over the world due to its broad contribution to the various surface science fields including catalysis researches.<sup>59-63</sup> Now, numbers of desirable reviews are available for the recent technical developments and scientific achievements.<sup>64-67</sup>

To track the temporal evolution of chemical state at (near) surface region at given conditions is a highly attended topic to understand catalysis, because the catalytic performance is directly influenced

by the surface condition. In-situ oxidation and reduction of PGM surfaces have been extensively investigated using NAP-XPS techniques.<sup>68-71</sup> These researches revealed the surface oxidation proceeds on step by step manner, moreover a (chemical) hysteresis was found during the oxidation-reduction cycles; the surface oxide phase once dominates the surface during the oxidation, whereas it is not stably formed during the reduction. Because XPS can clarify the chemical state and quantify the amount of each element of species located at and near the surface, it is suitable for the observation of alloy systems. Tao et al. found that the surface elemental composition was reversibly controlled by the background gas environment on Pd–Rh alloy particles, which was explained by the chemical affinity between gas molecule and alloy surface.<sup>68</sup>

Based on the above in-situ techniques, the relationship between catalytic activity and surface chemical condition has been investigated on oxidation of CO and oxidation<sup>72-77</sup> and hydrogenation of organic molecules.<sup>78-81</sup> An early work for in-situ monitoring of CO oxidation was performed by Grass et al.; they revealed that the size of catalyst Rh particle is crucial to the catalytic performance; the RhO<sub>x</sub> species is responsible for the reactivity, and it was easily formed on smaller particles.<sup>73</sup> On the other hand, it is reported that the oxide formation is not necessary to the activity of Pt surfaces.<sup>74,77</sup> Pd is an effectual material for partial and complete hydrogenation of alkene. Teschner et al. found the Pd–C and Pd–H species, which are formed underneath the surface during the reaction, catalyze the partial and complete hydrogenation, respectively.<sup>78,79</sup> This clearly demonstrated that the catalytic selectivity strongly depends on the chemical condition of Pd catalyst and is tuned by the background environment.

Mass spectroscopy (MS) is a conventional technique to measure the catalytic performance. It intrinsically distinguishes gas-phase molecules by weight, for instance CO, 28; O<sub>2</sub>, 32; CO<sub>2</sub>, 44. It can directly measure the chemical conversion at given temperature and pressure, thus is often applied to identify the outlet gas composition from the flow (batch) reactor cell in parallel with surface sensitive tools. However, this technique basically provides averaged information from the surface. Planar laser-induced fluorescence (PLIF) is a remarkable development for the gas-phase sensitive measurement.<sup>82</sup> The gas-phase species near the sample is exposed to the sheet-shaped infrared laser pulse, and the corresponding fluorescence is probed by two-dimensional camera, for instance rovibrational transition (00<sup>0</sup>0) → (10<sup>0</sup>01) of CO<sub>2</sub>. It can provide the spatially and temporally resolved information on gas-phase species near the surface. Using this technique, catalytic performance of multiple samples can be simultaneously measured by position-dependence of the fluorescence emission, which is an advantage in comparison with the ordinary MS measurement.<sup>83</sup> The real-time evolution of catalytic CO oxidation on Pd single crystal surfaces has been carefully analyzed and the reaction kinetics has been discussed.<sup>84,85</sup> It had been predicted that the highly reactive surface consumes the reactant species immediately, and the reaction rate is controlled by the supply of the reactant gas to the surface, which is called as mass-transfer limit (MTL) regime. This technique has demonstrated the presence of the

MTL regime during the highly active conditions. It is necessary to pay attention to the MTL regime when in-situ experiments are performed for highly active catalysts.

#### 1.4 Aim of This Thesis

In this thesis, in-situ observations were applied for obtaining information on chemical interactions between molecules and metal substrates as a function of background pressure and temperature to reveal the adsorption behavior and further catalytic reaction mechanisms. The combination of experimental and theoretical techniques is employed comprehensively to earn the atomic-level understanding of surfaces and adsorbates. Particularly here I focused on adsorption and reaction of small molecules like CO and NO on PGM surfaces under near ambient pressure conditions, which are related to the TWC working under realistic conditions.

Although numbers of studies have been reported on molecular adsorption, the gas-phase species are usually ignored in traditional UHV-based investigations, so far. The adsorption (desorption) under equilibrium conditions is described by the Langmuir adsorption isotherm<sup>2</sup>, as follows;

$$\theta_A = \frac{K_A p_A}{1 + K_A p_A}, \quad (1.4.1)$$
$$K_A = \frac{k_A^+}{k_A^-}.$$

The surface coverage  $\theta_A$  of a molecular species A is determined by the background pressure  $p_A$ . Here  $k_A^+$  and  $k_A^-$  are the rate constants of adsorption and desorption, respectively. The surface coverage increases with raising the background pressure. Although the pressure dependence of the surface coverage can be sometimes explained by this model, the adsorption on actual surfaces often seems more complicated; chemical interaction effects such as adsorption site switching, molecule-molecule steric repulsion and surface restructuring contribute to the adsorption behavior. It is desirable to reveal details of the adsorbate-adsorbate and adsorbate-substrate interactions and describe the resultant adsorption structures on the surface. In particular, it is not clear how the molecules adsorb on the surface under high background pressures.

Adsorption of CO and NO on PGM surfaces is investigated by XPS and IRAS as a function of pressure (Chapter 3). Here, evolution of adsorption site and surface coverage of CO at elevated pressures is studied to understand the periodic and local structures of adsorbed CO molecules under equilibrium with high pressure gaseous CO. Then adsorption of NO on PGM surfaces is investigated. A part of NO molecules dissociate into the atomic species. It is shown that the resultant coadsorption phase is rearranged under the high-pressure NO gas exposure. Furthermore CO adsorption on a Pd-Au alloy surface is also studied to observe alloying effects on preferred adsorption site, where accessible Pd sites are limited by the rich Au segregation to the surface. Pressure-dependent site

switching of CO adsorbed on surface Pd is studied and correlated with pressure-induced chemical potential change of gas-phase CO on the basis of theoretical calculations.

As mentioned above, a great number of studies have focused on the active phases for CO oxidation on PGM surfaces under ambient pressure conditions. Based on in-situ observations of the CO oxidation reaction, the reaction mechanism under high pressure conditions has been discussed. However no consensus has emerged yet. Morphologic approaches have proposed the oxide formation during the reaction, while the vibrational studies have suggested the CO-depleted metallic surface is the active phase. In-situ identification of chemical state of the surface during the reaction is required to determine the active phase of the reaction.

XPS enables us to analyze both of substrate and adsorbate under the reaction conditions at a time. Especially it can distinguish the chemical states of catalyst surfaces, for instance, distinguish between metallic surface and oxide surface, which is crucial to understand the reaction mechanism. The catalytic CO oxidation reactions on Pd single-crystal surfaces are studied with in-situ observations under ambient pressure conditions (Chapter 4). Pd is the most used material for the TWC. Here Pd(111), (100) and (110) single-crystal surfaces are used as model catalyst systems with different surface structures to reveal the relationship between the catalytically active phase and the surface structure of catalyst.



## References

- [1] Döbreiner, J. W. *Schweigg J.* **1823**, 39, 1.
- [2] Langmuir, I. *J. Am. Chem. Soc.* **1918**, 40, 1361.
- [3] Eley, D. D.; Rideal, E. K. *Nature* **1940**, 146, 401.
- [4] Winterlin, L.; Völkening, S.; Janssens, T. V. W.; Zambelli, T.; Ertl, G. *Science* **1997**, 278, 1931.
- [5] Mars, P.; van Krevelen, D. W. *Chem. Eng. Sci.* **1954**, 3, 41-59.
- [6] Hammer, B.; Nielsen, O. H.; Nørskov, J. K. *Catal. Lett.* **1997**, 46, 31.
- [7] Grönbeck, H.; Klacar, S.; Martin, M. M.; Hellman, A.; Lundgren, E.; Andersen, J. N. *Phys. Rev. B* **2012**, 85, 115445.
- [8] Zeng, Z.-H.; Da Silva, J. L. F.; Deng, H.-Q.; Li, W.-X. *Phys. Rev. B* **2009**, 79, 205413.
- [9] Duan, Z.; Henkelman, G. *ACS Catal.* **2014**, 4, 3435.
- [10] Lundgren, E.; Kresse, G.; Klein, C.; Borg, M.; Andersen, J. N.; De Santis, M.; Gauthier, Y.; Konvicka, C.; Schmid, M.; Varga, P. *Phys. Rev. Lett.* **2002**, 88, 246103.
- [11] Zheng, G.; Altman, E. I. *Surf. Sci.* **2000**, 462, 151.
- [12] Saily, M.; Warren, O. L.; Thiel, P. A.; Mitchell, K. A. R. *Surf. Sci.* **2001**, 494, L799.
- [13] Todorova, M.; Lundgren, E.; Blum, V.; Mikkelsen, A.; Gray, S.; Gustafson, J.; Borg, M.; Rogal, J.; Reuter, K.; Andersen, J. N.; Scheffler, M. *Surf. Sci.* **2003**, 541, 101.
- [14] Kostelník, P.; Seriani, N.; Kresse, G.; Anders Mikkelsen, A.; Lundgren, E.; Blum, V.; Šikola, T.; Varga, P.; Schmid, M. *Surf. Sci.* **2007**, 601, 1574.
- [15] Wang, J. G.; Li, W. X.; Borg, M.; Gusdafson, J.; Mikkelsen, A.; Pedersen, T. M.; Lundgren, E.; Weissenrieder, J.; Klikovits, J.; Schmid, M.; Hammer, B.; Andersen, J. N. *Phys. Rev. Lett.* **2005**, 95, 256102.
- [16] Miller, D. J.; Öberg, H.; Kaya, S.; Casalongue, H. S.; Friebel, D.; Anniyev, T.; Ogasawara, H.; Bluhm, H.; Pettersson, L. G. M.; Nilsson, A. *Phys. Rev. Lett.* **2011**, 107, 195502.
- [17] Miller, D.; Casalongue, H. S.; Bluhm, H.; Ogasawara, H.; Nilsson, A.; Kaya, S. *J. Am. Chem. Soc.* **2014**, 136, 6340.
- [18] Li, W. X.; Österlund, L.; Vestergassrd, E. K.; Vang, R. T.; Matthiesen, J.; Pedersen, T. M.; Lægsgaard, E.; Hammer, B.; Besenhacher, F. *Phys. Rev. Lett.* **2004**, 93, 146104.
- [19] Butcher D. R.; Grass, M. E.; Zeng, Z.; Aksoy, F.; Bluhm, H.; Li, W. X.; Mun, B. S.; Somorjai, G. A.; Liu, Z. *J. Am. Chem. Soc.* **2011**, 133, 20319.
- [20] Gustafson, J.; Mikkelsen, A.; Borg, M.; Lundgren, E.; Köhler, L.; Kresse, G.; Schmid, M.; Varga, P.; Yuhara, J.; Torrelles, X.; Quirós, C.; Andersen, J. N. *Phys. Rev. Lett.* **2004**, 92, 126102.
- [21] Blomberg, S.; Lundgren, E.; Westerström, R.; Erdogan, E.; Martin, N. M.; Mikkelsen, A.; Andersen, J. N.; Mittendorfer, F.; Gustafson, J. *Surf. Sci.* **2012**, 606, 1416.
- [22] Martin, N. M.; Van den Bossche, M.; Grönbeck, H.; Hakanoglu, C.; Zhang, F.; Li, T.; Gustafson, J.; Weaver, J. F.; Lundgren, E. *J. Phys. Chem. C* **2014**, 118, 1118.
- [23] Over, H.; Kim, Y. D.; Seitsonen, A. P.; Wendt, S.; Lundgren, E.; Schmid, M.; Varga, P.; Morgante, A.; Ertl, G. *Science* **2000**, 287, 1474.
- [24] Stamenkovic, V. R.; Fowler, B.; Mun, B. S.; Wang, G.; Ross, P. N.; Lucas, C. A.; Markovic, N. M. *Science* **2007**, 315, 493.
- [25] Bandarenka, A. S.; Varela, A. S.; Karamad, M.; Calle-Vallejo, F.; Bech, L.; Perez-Alonso, F. J.; Rossmeisl, J.; Stephens, I. E. L.; Chorkendorff, I. *Angew. Chem. Int. Ed.* **2012**, 51, 11845.
- [26] Divins, N. J.; Angurell, I.; Escudero, C.; Pérez-Dieste, V.; Llorca, J. *Science* **2014**, 346, 620.
- [27] Besenbacher, F.; Chorkendorff, I.; Clausen, B. S.; Hammer, B.; Molenbroek, A. M.; Nørskov, J. K. Stensgaard, I. *Science* **279**, 1913.
- [28] Vestergaard, E. K.; Vang, R. T.; Kundsén, J.; Pedersen, T. M.; An, T.; Lægsgaard, E.; Stensgaard, I.; Hammer, B.; Besenbacher, F. *Phys. Rev. Lett.* **2005**, 95, 126101.
- [29] Maroun, F.; Ozanam, F.; Magnussen, O. M.; Behm, R. J. *Science* **2001**, 293, 1811–1814.
- [30] Scott, R. W. J.; Sivadinarayana, C.; Wilson, O. M.; Yan, Z.; Goodman, D. W.; Crooks, R. M. *J. Am. Chem. Soc.* **2005**, 127, 1380.
- [31] Chen, M.; Kumar, D.; Yi, C.-W.; Goodman, D. W. *Science* **2005**, 310, 291.
- [32] Yu, W.-Y.; Mullen, G. M.; Flaherty, D. W.; Mullins, C. B. *J. Am. Chem. Soc.* **2014**, 136, 11070.
- [33] Hutchings, G. *Chem. Commun.* **2008**, 44, 1148.

- [34] van Rijn, R.; Ackermann, M. D.; Balmes, O.; Dufrane, T.; Geluk, A.; Gonzalez, H.; Isern, H.; de Kuiper, E.; Petit, L.; Sole, V. A.; Wermeille, D.; Felici, R.; Frenken, J. W. M. *Rev. Sci. Instrum.* **2010**, *81*, 014101.
- [35] Hendriksen, B. L. M.; Ackermann, M. D.; van Rijn, R.; Stoltz, D.; Popa, I.; Balmes, O.; Resta, A.; Wermeille, D.; Felici, R.; Ferrer, S.; Frenken, J. W. M. *Nat. Chem.* **2010**, *2*, 730.
- [36] van Rijn, R.; Balmes, O.; Resta, A.; Wermeille, D.; Westenström, R.; Gustafson, J.; Felici, R.; Lundgren, E.; Frenken, J. W. M. *Phys. Chem. Chem. Phys.* **2011**, *13*, 13167.
- [37] Hellman, A.; Resta, A.; Martin, N. M.; Gustafson, J.; Trincherro, A.; Carlsson, P.-A.; Balmes, O.; Felici, R.; van Rijn, R.; Frenken, J. W. M.; Andersen, J. N.; Lundgren, E.; Grönbeck, H. *J. Phys. Chem. Lett.* **2012**, *3*, 678.
- [38] Kasper, N.; Nolte, P.; Stierle, A. *J. Phys. Chem. C* **2012**, *116*, 21459.
- [39] Gustafson, J.; Shipilin, M.; Zhang, C.; Stierle, A.; Hejral, U.; Ruett, U.; Gutowski, O.; Carlsson, P.-A.; Skoglundh, M.; Lundgren, E. *Science* **2014**, *343*, 758.
- [40] Jensen, J. A.; Rider, K. B.; Salmeron, M.; Somorjai, G. A. *Phys. Rev. Lett.* 1998, *80*, 1228.
- [41] Vestergaard, E. K.; Thostrup, P.; An, T.; Lægsgaard, E.; Stensgaard, I.; Hammer, B.; Besenbacher, F. *Phys. Rev. Lett.* **2002**, *88*, 259601.
- [42] Longwitz, S. R.; Schnadt, J.; Vestergaard, E. V.; Vang, R. T.; Lægsgaard, E.; Stensgaard, I.; Brune, H.; Besenbacher, F. *J. Phys. Chem. B* **2004**, *108*, 14497.
- [43] Tao, F.; Dag, S.; Wang, L.-W.; Liu, Z.; Butcher, D. R.; Bluhm, H.; Salmeron, M.; Somorjai, G. A. *Science* **2010**, *327*, 850.
- [44] Tao, F.; Dag, S.; Wang, L.-W.; Liu, Z.; Butcher, D. R.; Salmeron, M.; Somorjai, G. A. *Nano Lett.* **2009**, *9*, 2167.
- [45] Zhu, Z.; Butcher, D. R.; Mao, B.; Liu, Z.; Salmeron, M.; Somorjai, G. A. *J. Phys. Chem. C* **2013**, *117*, 2799.
- [46] Vang, R. T.; Wang, J.-G.; Knudsen, J.; Schnadt, J.; Lægsgaard, E.; Stensgaard, I.; Besenbacher, F. *J. Phys. Chem. B* **2005**, *109*, 14262.
- [47] Hendriksen, B. L. M.; Frenken, J. W. M. *Phys. Rev. Lett.* **2002**, *89*, 046101.
- [48] Hendriksen, B. L. M.; Bobaru, S. C.; Frenken, J. W. M. *Surf. Sci.* **2004**, *552*, 229.
- [49] Herbschleb, C. T.; van der Tuijn, P. C.; Roobol, S. B.; Navarro, V.; Bakker, J. W.; Liu, Q.; Stoltz, D.; Cañas-Ventura, M. E.; Verdoes, G.; van Spronsen, M. A.; Bergman, M.; Crama, L.; Taminiau, I.; van Baarle, G. J. C.; Frenken, J. W. M. *Rev. Sci. Instrum.* **2014**, *85*, 083703.
- [50] Roobol, S. B.; Cañas-Ventura, M. E.; Bergman, M.; van Spronsen, M. A.; Onderwaater, W. G.; van der Tuijn, P. C.; Koehler, R.; Ofitserov, A.; van Baarle, G. J. C.; Frenken, J. W. M. *Rev. Sci. Instrum.* **2015**, *86*, 033706.
- [51] Dellwig, T.; Rupprechter, G.; Unterhalt, H.; Freund, H.-J. *Phys. Rev. Lett.* **2000**, *85*, 776.
- [52] Rupprechter, G.; Dellwig, T.; Unterhalt, H.; Freund, H.-J. *J. Phys. Chem. B* **2001**, *105*, 3797.
- [53] McCrea, K.; Parker, J. S.; Chen, P.; Somorjai, G. *Surf. Sci.* **2001**, *494*, 238.
- [54] Unterhalt, H.; Rupprechter, G.; Freund, H.-J. *J. Phys. Chem. B* **2002**, *106*, 356.
- [55] Rupprechter, G.; Unterhalt, H.; Morkel, M.; Galletto, P.; Hu, L.; Freund, H.-J. *Surf. Sci.* **2002**, *502-503*, 109.
- [56] Ozensoy, E.; Hess, C.; Loffreda, D.; Sautet, P.; Goodman, D. W. *J. Phys. Chem. B* **2005**, *109*, 5414.
- [57] Hess C.; Ozensoy, E.; Yi, C.-W.; Goodman, D. W. *J. Am. Chem. Soc.* **2006**, *128*, 2988.
- [58] Gao, F.; Wang, Y.; Goodman, D. W. *J. Am. Chem. Soc.* **2009**, *131*, 5734.
- [59] Grass, M. E.; Karlsson, P. G.; Aksoy, F.; Lundqvist, M.; Wannberg, B.; Mun, B. S.; Hussain, Z.; Liu Z. *Rev. Sci. Instrum.* **2010**, *81*, 053106.
- [60] Tao, F. *Chem. Commun.* **2012**, *48*, 3812.
- [61] Schnadt, J.; Knudsen, J.; Andersen, J. N.; Siegbahn, H.; Pietzsch, A.; Hennies, F.; Johansson, N.; Mårtensson, N.; Öhrwall, G.; Bahr, S.; Mähld, S.; Schaff, O. *Synchrotron Rad.* **2012**, *19*, 701.
- [62] Kaya, S.; Ogasawara, H.; Näslund, L.-Å.; Forsell, J.-O.; Casalongue, H. S.; Miller, D. J.; Nilsson, A. *Catal. Today* **2013**, *205*, 101.
- [63] Roy, K.; Vinod, C. P.; Gopinath, C. S. *J. Phys. Chem. C* **2013**, *117*, 4717.
- [64] Salmeron, M.; Schlögl, R. *Surf. Sci. Rep.* **2008**, *63*, 169.
- [65] Tao, F.; Salmeron, M. *Science* **2011**, *331*, 171.

- [66] Tao, F.; Zhang, S.; Nguyen, L.; Zhang, X. *Chem. Commun.* **2012**, *41*, 7980.
- [67] Starr, D. E.; Liu, Z.; Hävecker, M.; Knop-Gericke, A.; Bluhm, H. *Chem. Soc. Rev.* **2013**, *42*, 5833.
- [68] Tao, F.; Grass, M. E.; Zhang, Y.; Butcher, D. R.; Renzas, J. R.; Liu, Z.; Chung, J. Y.; Mun, B. S.; Salmeron, M.; Somorjai, G. A. *Science* **2008**, *322*, 932.
- [69] Westerström, R.; Messing, M. E.; Blomberg, S.; Hellman, A.; Grönbeck, H.; Gustafson, J.; Martin, N. M.; Balmes, O.; van Rijn, R.; Andersen, J. N.; Deppert, K.; Bluhm, H.; Liu, Z.; Grass, M. E.; Hävecker, M.; Lundgren, E. *Phys. Rev. B* **2011**, *83*, 115440.
- [70] Mao, B.-H.; Chang, R.; Lee, S.; Axnanda, S.; Crumlin, E.; Grass, M. E.; Wang, S.-D.; Vajda, S.; Liu, Z. *J. Chem. Phys.* **2013**, *138*, 214304.
- [71] Ketteler, G.; Ogletree, D. F.; Bluhm, H.; Liu, H.; Hebenstreit, E. L. D.; Salmeron, M. *J. Am. Chem. Soc.* **2005**, *127*, 18269.
- [72] Blume, R.; Niehus, H.; Conrad, H.; Böttcher, A.; Aballe, L.; Gregoratti, L.; Barinov, A.; Kiskinova, M. *J. Phys. Chem. B* **2005**, *109*, 14052.
- [73] Grass, M. E.; Zhang, Y.; Butcher, D. R.; Park, J. Y.; Li, Y.; Bluhm, H.; Bratlie, K. M.; Zhang, T.; Somorjai, G. A. *Angew. Chem. Int. Ed.* **2008**, *47*, 8893.
- [74] Chung, J.-Y.; Aksoy, F.; Grass, M. E.; Kondoh, H.; Ross Jr., P.; Liu, Z.; Mun, B. S. *Surf. Sci. Lett.* **2009**, *603*, L35.
- [75] Blomberg, S.; Hoffmann, M. J.; Gustafson, J.; Martin, N. M.; Fernandes, V. R.; Borg, A.; Liu, Z.; Chang, R.; Matera, S.; Reuter, K.; Lundgren, E. *Phys. Rev. Lett.* **2013**, *110*, 117601.
- [76] Blume, R.; Hävecker, M.; Zafeiratos, S.; Teschner, D.; Kleimenov, E.; Knop-Gericke, A.; Schlögl, R.; Barinov, A.; Dudin, P.; Kiskinova, M. *J. Catal.* **2006**, *239*, 354.
- [77] Porsgaard, S.; Ono, L. K.; Zeuthen, H.; Knudsen, J.; Schnadt, J.; Merte, L. R.; Chevallier, J.; Helveg, S.; Salmeron, M.; Wendt, S.; Besenbacher, F. *ChemPhysChem* **2013**, *14*, 1553.
- [78] Teschner, D.; Borsodi, J.; Wootsch, A.; Révay, Z.; Hävecker, M.; Knop-Gericke, A.; Jackson, S. D.; Schlögl, R. *Science* **2008**, *320*, 86.
- [79] Teschner, D.; Révay, Z.; Borsodi, J.; Hävecker, M.; Knop-Gericke, A.; Schlögl, R.; Milroy, R.; Jackson, S. D.; Torres, D.; Sautet, P. *Angew. Chem. Int. Ed.* **2008**, *47*, 9274.
- [80] Lee, A. F.; Naughton, J. N.; Liu, Z.; Wilson, K. *ACS Catal.* **2012**, *2*, 2235.
- [81] Lee, A. F.; Prabhakaran, V.; Wilson, K. *Chem. Commun.* **2010**, *46*, 3827.
- [82] Zetterberg, J.; Blomberg, S.; Gustafson, J.; Sun, Z. W.; Li, Z. S.; Lundgren, E.; Aldén, M. *Rev. Sci. Instrum.* **2012**, *83*, 053104.
- [83] Zetterberg, J.; Blomberg, S.; Gustafson, J.; Evertsson, J.; Zhou, J.; Adams, E. C.; Carlsson, P.-A.; Aldén, M.; Lundgren, E. *Nat. Commun.* **2015**, *6*, 7076.
- [84] Blomberg, S.; Brackmann, C.; Gustafson, J.; Aldén, M.; Lundgren, E.; Zetterberg, J. *ACS Catal.* **2015**, *5*, 2028.
- [85] Matera, S.; Blomberg, S.; Hoffman, M. J.; Zetterberg, J.; Gustafson, J.; Lundgren, E.; Reuter, K. *ACS Catal.* **2015**, *5*, 4515.



## Chapter 2

### Research Methods

---

#### 2.1 X-ray Photoelectron Spectroscopy<sup>1,2</sup>

When material surfaces are exposed to a photo irradiation, photoelectrons are emitted into the vacuum (photoionization). With X-ray photoelectron spectroscopy (XPS) photoelectron kinetic energies are measured, and then binding energies of core-electrons are deduced. Synchrotron radiations and lab-scale X-ray sources, e.g. Al K $\alpha$  (1486.6 eV) and Mg K $\alpha$  (1253.6 eV), are used for core-electron excitation. XPS can be clearly used to characterize elemental composition of the material, because the core-binding energy is unique for each core level of each element. Photoionization process satisfies the energy conservation law described as follows;

$$h\nu = E_b + E_k + \phi, \quad (2.1.1)$$

where the terms  $h\nu$ ,  $E_b$ ,  $E_k$  and  $\phi$  are the incident photon energy, electron binding energy, photoelectron kinetic energy and work function, respectively. The schematic description is shown in Figure 2.1.1. The binding energy is determined by the energy difference of the initial ground state ( $n_i$ ) and final core-excited state ( $n_i - 1$ ).

$$E_b = [E(n_i - 1) - E(n_i)]. \quad (2.1.2)$$

If the core-potential is unchanged before and after core-excitation, the binding energy is estimated from the initial state (Koopmans' theorem).<sup>3</sup>

The photoelectron emission conforms Fermi's golden rule, described as follows;

$$T_{i \rightarrow f} = \frac{4\pi^2}{h} |\langle \varphi_f | H' | \varphi_i \rangle|^2 \delta(E_f - E_i - h\nu), \quad (2.1.3)$$

where  $\varphi_i$  and  $\varphi_f$  are the wave functions of the initial (interested core-level) and final (photoelectron) states.  $E_f$  and  $E_i$  are the energy of those states, and  $h\nu$  is the incident photon energy.  $H'$  is time dependent part of Hamiltonian. It suggests that the electron excitation (emission) is permitted when the transition moment is not zero and the energy conservation law is satisfied at a time. Derivation of the equation is described in Appendix A. Change in intensity of the same core-level refers the number of included atoms in the system. It is noted that the equation is a universal concept for excitation between two eigenstates, thus the vibrational excitation is also explained in this scheme.

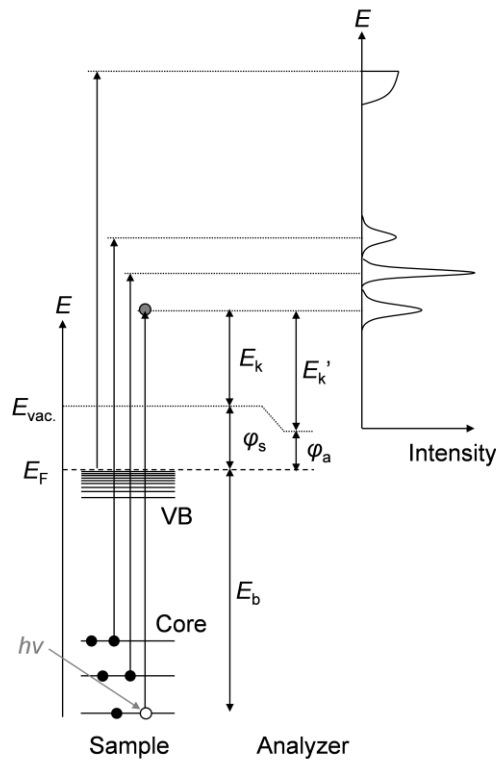


**Figure 2.1.1.** Schematic description of X-ray induced photoionization process.

The photoelectron kinetic energy is decided by the incident photon energy, therefore the cross-section is a function of incident photon energy. Figure 2.1.2 shows the energy dependence of photoionization cross-section, which is simulated for fcc-Pd. It demonstrates the transition possibility reaches to the maximum when the kinetic energy is around 100 eV. It is noted that the photoionization occurs regardless of the azimuthal quantum number of interested core-orbital (Appendix B).

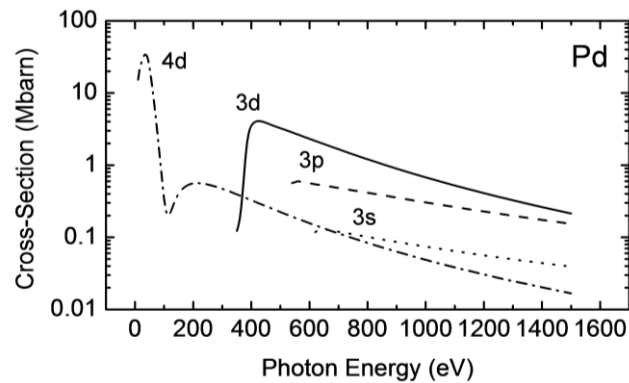


**Figure 2.1.2.** Simulated energy dependence of photoionization cross-sections for Pd.

Photoelectrons moving in bulk crystal are scattered with a certain probability: the plasmon excitation, electron–hole pair excitation and phonon excitation. The inelastic mean free paths (IMFPs) depend on the valence band structures of materials, but the resultant line profiles are roughly the same (universal curve). Figure 2.1.3 shows the example of simulated IMFPs for some precious metals (TPP-2M).<sup>4</sup> The intrinsic surface sensitivity of this technique stems from the short IMFP of photoelectron.

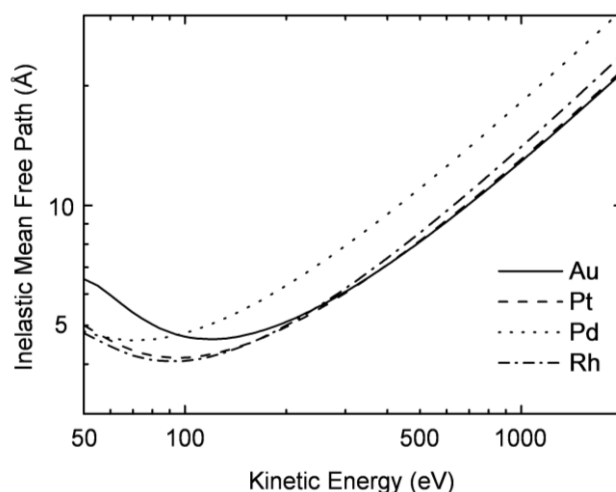


**Figure 2.1.3.** Simulated inelastic mean free paths for several precious metals.

The lift time of core-excited state is finite in the order of femtosecond ( $10^{-15}$  s), thus the obtained spectrum has (basically) a Lorentzian shape of a natural width. In the case of metal systems, the emitted photoelectrons cause the secondary excitation of the valence band electrons. It results in the continuous energy loss of the photoelectron kinetic energy, it is experimentally observed an asymmetric tailing of the spectrum to the higher binding energy side. The spectral line shape is described by Doniach–Šunjić function<sup>5</sup>, which is the convolution of Lorentzian and a step function with asymmetric factor. It is noted that the experimental spectra include a contribution from Gaussian function which comes from experimental error.

The core-level shift (CLS) is determined as an internal difference of interested and referenced binding energies, which is the sign of difference of electric structure between interested and referenced atoms.

$$E_{\text{CLS}} = E_{\text{b}} - E_{\text{b}}^{\text{ref}}. \quad (2.1.4)$$

For instance, the topmost surface atoms exhibit lower-shift of binding energy relative to the internal bulk ones on PGMs, which comes from the d-band narrowing on surface region. Chemical interactions with molecules (atoms) also modulate the electric structure of the surface atoms, therefore the CLS is applied to the chemical characterization of the system, e.g. metal or oxide.

Basically, the core-binding energy is determined by the Coulomb interaction, therefore CLS is also explained by the difference of electric charge as follows;

$$E_i^{\text{CLS}} = kq_i + \sum_{i \neq j} \frac{q_j}{R_{i,j}}. \quad (2.1.5)$$

The first term is the internal effect of interested atom, the  $q_i$  is the net charge on the atom  $i$ , and  $k$  is Coulomb repulsion integral. The second term is the background effect (Madelung potential),  $R_{i,j}$  is the distance between the atoms  $i$  and  $j$ . The positive (negative) net charge on the interested atom  $i$  causes a positive (negative) shift.<sup>6</sup>

For chemisorbed systems, a simple explanation has been proposed.<sup>7</sup> The molecule (atom) on surfaces adsorb on highly symmetry sites, e.g. hollow, bridge and top. The CLSs of adsorbed metal atoms exhibit the linear relationship as follows;

$$E_{i,j}^{\text{CLS}} \approx iE_{1,j}^{\text{CLS}}, \quad (2.1.6)$$

$$E_{1,j}^{\text{CLS}} \approx \frac{1}{j}E_{1,1}^{\text{CLS}}, \quad (2.1.7)$$

where  $i$  and  $j$  are the number of adsorbate and adsorbed metal atom in the system, e.g.  $j=1$ , top; 2, bridge; 3, three-fold-hollow; 4, four-fold-hollow. Here, it suggests that the initial and final state effects constantly increase as a function of the number of adsorbate. These ideas suppose that the CLS is defined by the energy difference before photoexcitation, which is called the initial state approximation. The chemical interaction mainly alters the valence band structure. Therefore, it is assumed that the CLS can be represented by the shift of valence band, especially the d-band center. However, the relaxation process of core-hole also alters the obtained CLS; the final state effect is enhanced in the case of strongly-correlated systems.

## 2.2 Infrared Reflection Absorption Spectroscopy<sup>8</sup>

The  $N$ -atomic molecules have  $3N$  internal degree of freedom. In the case of diatomic molecule, it is decomposed to 3-translational motion, 2-rotational mode and 1-vibrational mode. As discussed in Chapter 1, molecules strongly interact with surfaces, resulting in the adsorption. On the surfaces, all  $3N$  degree of freedom is converted to vibrational mode. To investigate the vibrational structure of the molecule leads to understanding of the behavior of molecules on the surface.

It is assumed that a diatomic molecule AB consists of atom A and B connected with a spring constant  $k$ . The equation of motion for the vibration and the corresponding potential are written as follows (harmonic oscillator approximation);

$$F(x) = m \frac{d^2x}{dt^2} = -kx, \quad (2.2.1)$$

$$V(x) = - \int F(x) dx = \frac{1}{2} kx^2. \quad (2.2.2)$$

here,  $m$  is the reduced mass of the molecule and  $x$  is the distance from equilibrium internuclear position. To describe the quantum mechanical vibration, the Schrödinger equation is written as follows;

$$H\psi = \left[ -\frac{\hbar^2}{2m} \nabla^2 + \frac{1}{2} kx^2 \right] \psi = E\psi. \quad (2.2.3)$$

As a result, the energy of the harmonic oscillator is quantized at equal intervals  $h\nu$ , and the lowest energy level ( $n = 0$ ) has a value of some finite (zero point energy).

$$E_n = \left( n + \frac{1}{2} \right) \hbar \sqrt{\frac{k}{m}} = \left( n + \frac{1}{2} \right) h\nu \quad (n = 0, 1, 2, \dots), \quad (2.2.4)$$

$$\nu = \frac{1}{2\pi} \sqrt{\frac{k}{m}}.$$

Additionally, the absorption of photon is governed by Fermi's golden rule, see eq. (2.1.3). Besides, the rovibrational mode, formed by the coupling of the rotation and vibrational mode, is experimentally observed in the case of gaseous molecules. The life-time of the nuclear vibration is in order of (sub-) pico-second ( $10^{-12}$  s), thus the energy resolution of the spectrum is intrinsically better than that of XPS. It enables us to investigate the local adsorption site of the molecule on the surface as discussed later. Infrared absorption spectroscopy (IRAS) is a surface sensitive setup for investigating molecular adsorbed systems. The schematic view is shown in Figure 2.2.1. The surface is irradiated with infrared light with a grazing angle  $\theta$  (total reflection). The electric field vector normal to the surface (p-polarization) is enhanced on the surface, here  $E_p^\perp \simeq 2E_p$ . Whereas the electric field parallel to the surface (s-polarization) is weakened on the surface. The vibration mode is excited, when the inner product of electric field vector and electric dipole moment is not equal zero. Therefore the incident IR light excites only the vibrational mode normal to the surface. The transition probability  $T$  is proportional to these factors as follows;

$$T \propto \left| \frac{E_p^\perp}{E_p} \right|^2 \frac{1}{\cos \theta}. \quad (2.2.5)$$

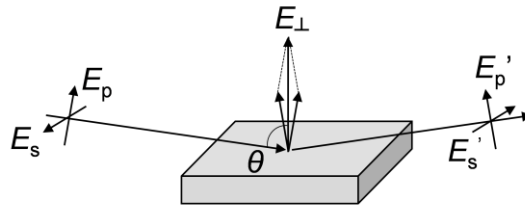


**Figure 2.2.1.** Schematic description of measurement principle of IRAS.

### 2.3 Low Energy Electron Diffraction<sup>9</sup>

Low energy electron diffraction (LEED) is a conventional surface science tool to investigate surface morphology and adsorbate lattice. The incident electron (wave) is scattered on the surface. The back-scattered electron pattern is recorded by the fluorescent screen. Since the surface has quasi-two-dimensional periodicity, the scattered electron is observed as a reciprocal lattice rod, which is perpendicular to the surface normal. The diffraction intensity  $F$  is defined by the following equation;

$$F = \sum_{\mathbf{G}} \int n_{\mathbf{G}} \exp[i(\mathbf{G} - \Delta\mathbf{k}) \cdot \mathbf{r}] dV, \quad (2.3.1)$$

where,  $\mathbf{G}$ ,  $\Delta\mathbf{k}$  and  $n_{\mathbf{G}}$  are the reciprocal lattice vector, scattering vector and Fourier coefficient. The reciprocal lattice vector is defined by using lattice vector  $\mathbf{R}$  and an integer  $m$ , as  $\mathbf{G} \cdot \mathbf{R} = 2\pi m$ . When the  $\mathbf{G} = \Delta\mathbf{k}$ , the diffraction intensity reaches to the maximum.

The de Broglie wave length  $\lambda$  is a function of electron energy  $E$  described as follows;

$$\lambda = \frac{h}{\sqrt{2m_e E}}, \quad (2.3.2)$$

where, the terms  $h$  and  $m_e$  indicate the Planck constant and electron's mass. Typically, the electron energy is tuned  $\sim 100$  eV, where penetration depth is limited in a few Ångström, suggesting the technique is surface sensitive. The surface imperfections give the diffuse diffraction spot size and background noise, which is secondary information on surface states. Besides, a high electron flux sometimes excites the adsorbates on surfaces, resulting a destruction of ordered layers, so called electron stimulated desorption. Figure 2.3.1 (a) and (b) show an example of LEED optics, and obtained diffraction pattern, respectively.

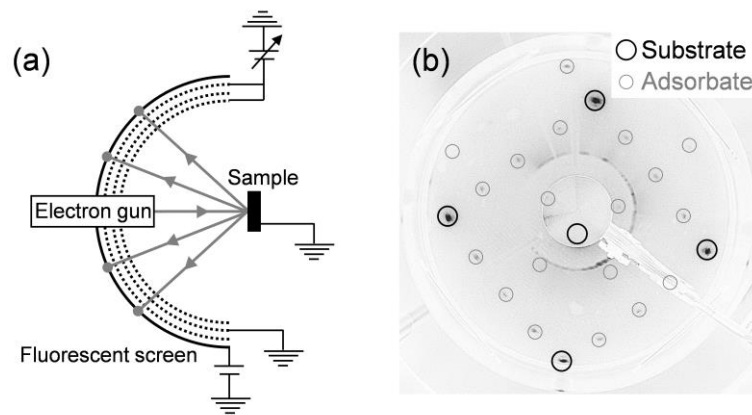


**Figure 2.3.1.** The schematic description of LEED optics (a) and an example of experimentally obtained LEED pattern (CO/Pd(100) surface).

## 2.4 Experimental Apparatus

### 2.4.1 Near-Ambient-Pressure X-ray Photoelectron Spectroscopy

All XPS measurements were performed at a synchrotron radiation facility to utilize the focused high-flux X-ray with the high-energy selectivity, which is crucial to collect the photoelectron under high pressure conditions. The experimental apparatus was connected to an undulator soft X-ray beamline BL13A/B at KEK-PF, Japan.<sup>10</sup> Photographic and schematic images of the NAP-XPS system are shown in Figure 2.4.1. The system consists of three vacuum chambers, namely the load-lock, preparation and analysis. The base pressures of preparation and analysis chambers are on the order of  $10^{-10}$  Torr. The sample is cleaned in the preparation chamber by the standard process: Ar<sup>+</sup> sputtering, surface oxidation and annealing. A LEED optics (Omicron, Spectra LEED) is available in the preparation chamber. The analysis chamber consists of four differential-pumping stages, which are pumped with turbo molecular pumps, to detect photoelectrons from the sample under high-pressure environments. The emitted photoelectrons are detected using an electron energy analyzer modified for high pressure experiments (Omicron, EA125HP). The sample temperature is controlled by liquid N<sub>2</sub> and resistive heater from the backside. The temperature is measured using an alumel-chromel (K-type) thermocouple attached to the sample holder. The sample is irradiated by X-ray introduced through a thin Si<sub>3</sub>N<sub>4</sub> film (100 nm thickness), which separates the beamline and analysis chamber. O<sub>2</sub>, CO and NO gases are introduced to the chamber using variable leak valves. A quadrupole MS (HIDEN, HAL201) is mounted on the way of differential-pumping stage to monitor the reactant and product gases.

Figure 2.4.2 shows a XP spectrum taken from Pd–Au alloy surface under 10 mTorr CO ambient. Here CO adsorbed on surface and in gas-phase are separately observed. The contribution from adsorbed species is attenuated with increasing the background pressure (Figure 2.4.3).

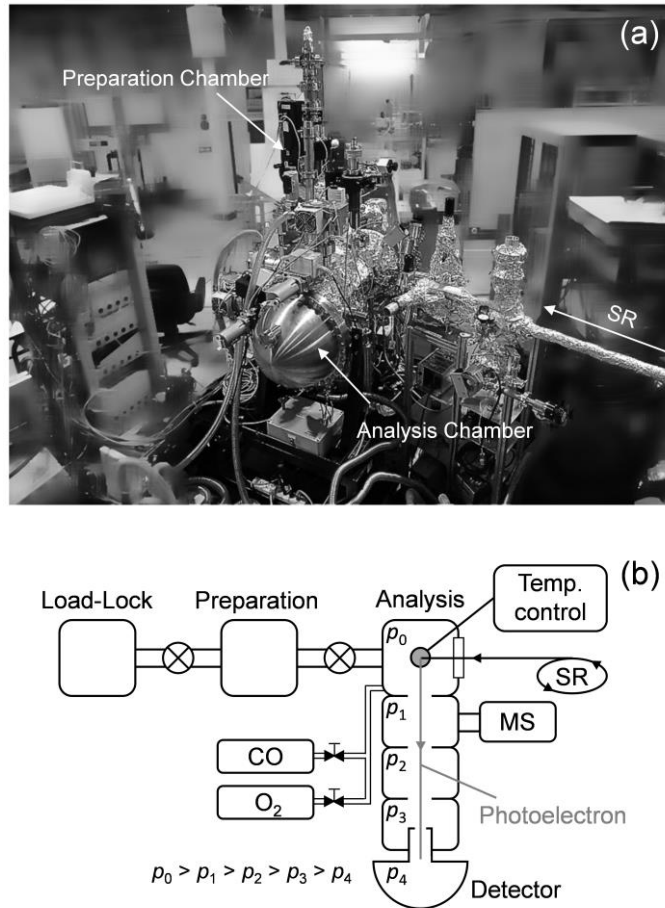


**Figure 2.4.1.** Photographic (a) and schematic (b) images of NAP-XPS system connected to the BL-13A/B at KEK-PF, Japan.

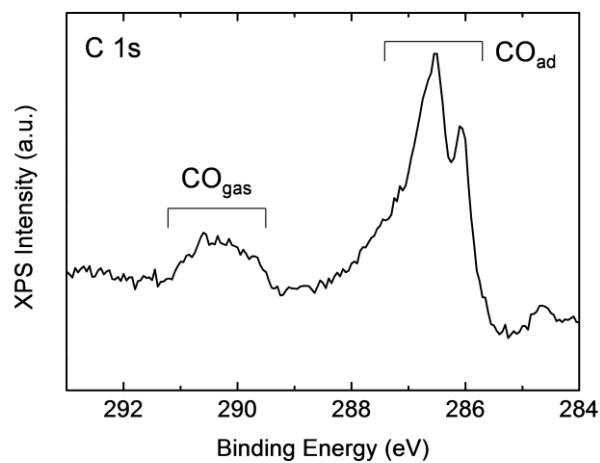


**Figure 2.4.2.** An example of XP spectrum taken from CO adsorbed surface. The data was taken under 10 mTorr CO ambient.

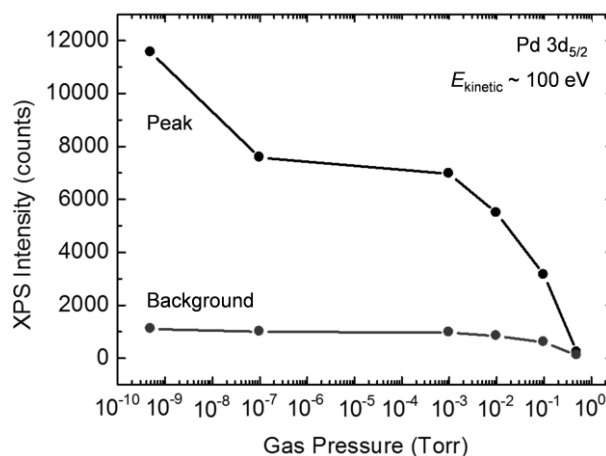


**Figure 2.4.3.** The pressure dependence of peak and background intensity.

### 2.4.2 Polarization Modulation Infrared Reflection Absorption Spectroscopy

The IRAS measurements were performed by a homemade vacuum chamber connecting with a mid-infrared generator (Nicolet iS50). The experimental apparatus was built up at Yagami campus, Keio University, Japan. Photographic and schematic images are shown in Figure 2.4.4. The system consists of three vacuum chambers, namely the load-lock, preparation and analysis. The base pressures of preparation and analysis chambers are on the order of  $10^{-10}$  Torr. The sample is cleaned in the preparation chamber by the standard process: ion sputtering, surface oxidation and annealing. Notably, this apparatus is modified for the PM- IRAS measurement. With this technique we can selectively observe the surface species under various pressure conditions. The sample is irradiated by infrared light with the grazing angle of  $80^\circ$ , where the sp-polarization is switched by 50 kHz using a photo-elastic modulator (PEM) unit. The reflected light is analyzed by a HgCdTe (MCT) detector. The optical path is purged by dried  $N_2$  gas.

Figure 2.4.5 shows examples of IRA spectra with and without PM. The p-polarized data contains both of gaseous and adsorbed species, whereas the s-polarized data contains only gaseous species as discussed section 2.2. Thus the gaseous species is dominant on s+p data (conventional IRAS), the gaseous species gives a complicated spectrum due to the rovibrational excitation. While the surface species is enhanced on p-s data (PM-IRAS).

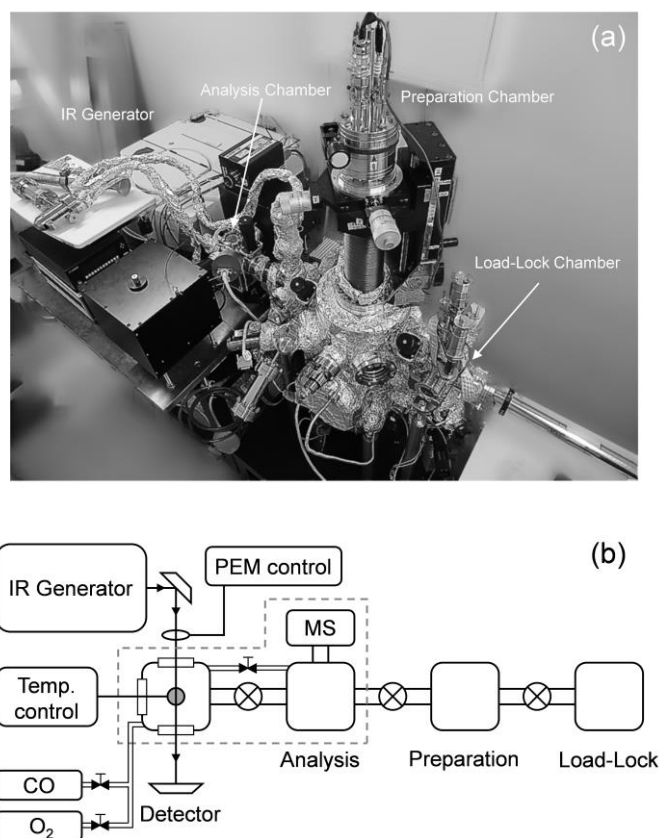


**Figure 2.4.4.** Photographic (a) and schematic (b) images of PM-IRAS system at Yagami campus, Keio University, Japan.

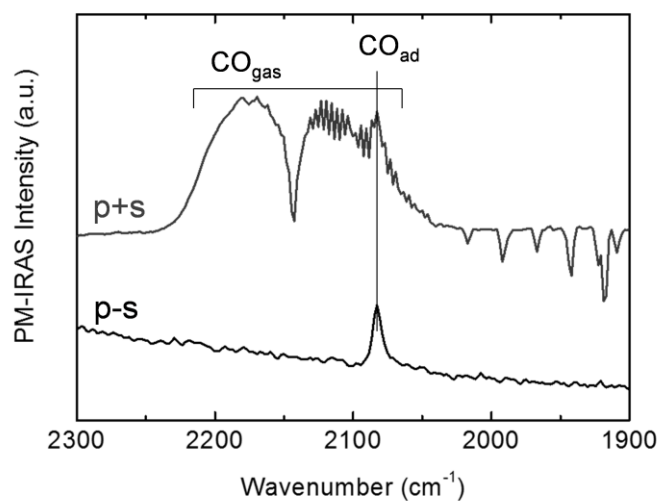


**Figure 2.4.5.** An example of (PM-)IRA spectrum taken from a CO adsorbed system. The data was taken under 100 mTorr CO ambient.

## 2.5 Density Functional Theory

### 2.5.1 Basic Theory

The basis of density functional theory (DFT) is established by Hohenberg and Kohn.<sup>11</sup> In this theory, the total electron energy of the system is a functional of electron density. When the total electron energy reaches the minimum value by changing wave function, the electron density becomes the one of the exact ground state. The total electron energy is described by the sum of kinetic energy  $T$ , Coulomb energy  $U$  and exchange–correlation energy  $E_{xc}$ .

$$E = T + U + E_{xc}. \quad (2.5.1)$$

Kohn and Sham suppose the electron density is expressed by the (quasi) electron orbitals.

$$\rho(\mathbf{r}) = \sum_{i=1}^N n_i \psi_i^*(\mathbf{r}) \psi_i(\mathbf{r}), \quad (2.5.2)$$

where,  $\rho$  is the electron density,  $\psi_i$  and  $n_i$  are a single particle wave function and partial occupation in an electron state  $i$ , respectively. Then, the kinetic energy  $T$  is given by

$$T = \sum_i n_i \int \psi_i^*(\mathbf{r}) \left[ -\frac{\hbar^2}{2m_e} \nabla^2 \right] \psi_i(\mathbf{r}) d\mathbf{r}. \quad (2.5.3)$$

Here, the electron–electron interaction is ignored: electrons moves in the averaged electrostatic potential. The complicated quantum contributions are considered in the  $E_{xc}$  term.

The Coulomb energy  $U$  is the classical electrostatic energy, which comes from nuclei–electron (ne) and electron–electron (ee) interactions.

$$U = U_{ne} + U_{ee} = - \sum_I \frac{Z_I e^2}{4\pi\epsilon_0} \int \frac{\rho(\mathbf{r}')}{|\mathbf{R}_I - \mathbf{r}'|} d\mathbf{r}' + \frac{e^2}{8\pi\epsilon_0} \iint \frac{\rho(\mathbf{r})\rho(\mathbf{r}')}{|\mathbf{r} - \mathbf{r}'|} d\mathbf{r}d\mathbf{r}'. \quad (2.5.4)$$

The exchange–correlation energy  $E_{xc}$  includes the complicated quantum contributions to the total energy, which is generally approximated by using, for example, pre-calculated values estimated from the free electron gas model.

To gain the minimum total electron energy  $E$ , the set of wave functions  $\psi_i$  is determined by solving Kohn–Sham equation<sup>12</sup>,

$$\left[ -\frac{\hbar^2}{2m_e} \nabla^2 + V_{ne} + V_{ee} + V_{xc} \right] \psi_i(\mathbf{r}) = \epsilon_i \psi_i(\mathbf{r}), \quad (2.5.6)$$

where,  $\epsilon_i$  is a Kohn–Sham eigenvalue, while  $V_{ne}$ ,  $V_{ee}$  and  $V_{xc}$  are the Coulomb and exchange–correlation potentials described as follows;

$$V_{ne} + V_{ee} = - \sum_I \frac{Z_I e^2}{4\pi\epsilon_0} \frac{1}{|\mathbf{R}_I - \mathbf{r}|} + \frac{e^2}{8\pi\epsilon_0} \int \frac{\rho(\mathbf{r}')}{|\mathbf{r} - \mathbf{r}'|} d\mathbf{r}', \quad (2.6.7)$$

$$V_{xc} = \frac{\delta E_{xc}[\rho(\mathbf{r})]}{\delta \rho(\mathbf{r})}.$$

The unit cell approach is suitable to represent crystal (and surface) systems, because they have

the translational symmetry. The plane wave basis set is employed to reproduce Kohn–Sham wave functions.

$$\psi_i(\mathbf{r}) = u_i(\mathbf{r})\exp(i\mathbf{k} \cdot \mathbf{r}). \quad (2.5.8)$$

The term  $\mathbf{k}$  is a wave vector, the periodic part  $u_i(\mathbf{r})$  is expanded by the reciprocal lattice vector  $\mathbf{G}$  depending on crystal structure (Bloch’s theorem). Then it is rewritten as follows;

$$\psi_i(\mathbf{r}) = \sum_{\mathbf{G}} C_{i,\mathbf{G}}\exp(i\mathbf{G} \cdot \mathbf{r})\exp(i\mathbf{k} \cdot \mathbf{r}) = \sum_{\mathbf{G}} C_{i,\mathbf{G}}\exp[i(\mathbf{k} + \mathbf{G}) \cdot \mathbf{r}]. \quad (2.5.9)$$

### 2.5.2 Adsorption Energy

The bond formation between molecule and metal surface induces the modulation of valence band structure and results in the stabilization of total electron energy in the system. The adsorption energy ( $E_{\text{ad}}$ ) extracts the energy difference due to the molecule adsorption to the surface. The averaged adsorption energy is estimated via the following equation,

$$E_{\text{ad}} = \frac{E_{j/i}^{\text{total}} - E_i^{\text{total}} - N_j E_j^{\text{total}}}{N_j}, \quad (2.5.10)$$

where  $E_i^{\text{total}}$ ,  $E_j^{\text{total}}$  and  $E_{j/i}^{\text{total}}$  are the total electron energies of molecule-free surface, isolated molecule in vacuum and molecule-adsorbed surface, respectively.  $N_j$  is the number of molecule included in the system.

This is a simple way to understand the molecule–surface interaction. However, the temperature is assumed to be 0 K in this method. Therefore, the adsorption energy simulation does not guarantee the most stable structure is formed under the interested temperature and pressure environments.

### 2.5.3 Surface Free Energy

The surface free energy ( $\gamma$ ) is defined as the energy requested to form the interested surface at given temperature ( $T$ ) and pressure ( $p$ ).<sup>13,14</sup> A surface structure with the lowest surface free energy is preferentially formed under a certain condition. The surface free energy is formulated as follows;

$$\gamma(T, \{p_j\}, \{N_i\}, \{N_j\}) = \frac{1}{A} \left[ G(T, \{p_j\}, \{N_i\}, \{N_j\}) - \sum_i N_i \mu_i - \sum_j N_j \mu_j \right], \quad (2.5.11)$$

where,  $G$  is the Gibbs free energy of the interested surface, and  $\mu_i$  and  $\mu_j$  are the chemical potentials of metal atom  $i$  and gaseous molecule  $j$ , respectively.  $N$  is the number of the species included in the system.  $A$  is a normalization factor, which is usually surface area of unit cell.

The Gibbs free energy consists of total electron energy, vibrational free energy and configurational entropy, which are functional of pressure and temperature of the system. However it

is usually approximated to the total electron energy. The validity is carefully discussed in Ref. 13.

$$G = E^{\text{total}} + F^{\text{vib.}} + TS^{\text{conf.}} + pV \approx E^{\text{total}}. \quad (2.5.12)$$

Then eq(2.5.11) is rewritten as follows;

$$\gamma(T, \{p_j\}, \{N_i\}, \{N_j\}) = \frac{1}{A} \left[ E_{j/i}^{\text{total}} - E_i^{\text{total}} - \sum_j N_j \mu_j \right], \quad (2.5.13)$$

where,  $E_{j/i}^{\text{total}}$  and  $E_i^{\text{total}}$  is a total electron energies of surface and bulk crystal, where  $E_i^{\text{total}} \approx G_i = N_i \mu_i$ , respectively. The chemical potential of molecule on the surface is in equilibrium with the background gaseous molecule via the partial pressure of  $p_j$ , thus it can be expressed by the chemical potential of gas-phase as follows;

$$\mu_j(T, p_j) = E_j^{\text{total}} + \Delta\mu_j(T, p_j) = E_j^{\text{total}} + \Delta\mu_j(T, p^0) + k_B T \ln \left( \frac{p_j}{p^0} \right), \quad (2.5.14)$$

where  $k_B$  is the Boltzmann constant, and  $E_j^{\text{total}}$  is the total electron energy of isolated molecule.  $\Delta\mu_j(T, p^0)$  is the standard chemical potential at the standard pressure  $p^0$  ( $= 1$  atm), which is obtained from tabulated enthalpy and entropy values. This equation means that the surface free energy of the system changes as a function of molecular chemical potential. In the case of bimetallic alloy system, further consideration is required (see Appendix C).

### 2.5.4 Core-Level Shift

Theoretical simulation of core-level shift (CLS) deduced from XPS is performed by Slater–Janak transition state approximation.<sup>15</sup> The CLS is defined by the difference of binding energy between the interested and referenced atoms, as described above. The binding energy of particular core level  $i$  is defined by the difference of total energies of the ground ( $E(n_i)$ ) and photo-excited ( $E(n_i - 1)$ ) systems, where  $n_i$  is the number of electrons occupying the core level  $i$ . In the DFT, the eigenvalue is obtained by the derivative of total electron energy (Janak's theorem)<sup>16</sup>. The simulated binding energy is approximated by the Kohn–Sham eigenvalue ( $\varepsilon_i$ ) with a half occupation.

$$[E(n_i - 1) - E(n_i)] = \int_{n_{i-1}}^{n_i} \frac{\partial E}{\partial n'} dn' \approx -\varepsilon_i \left( n_i - \frac{1}{2} \right), \quad (2.5.15)$$

$$E_{\text{CLS}} = [E(n_i - 1) - E(n_i)] - [E_{\text{ref.}}(n_i - 1) - E_{\text{ref.}}(n_i)]. \quad (2.5.16)$$

Further details of this method is discussed in Appendix D.

## References

- [1] Fadley, C. S. *Surf. Interface Anal.* **2008**, *40*, 1579.
- [2] Bagus, P.; Iltou, E. S.; Nelin, C. J. *Surf. Sci. Rep.* **2013**, *68*, 273.
- [3] Koopmans, von T. *Physica* **1933**, *1*, 104.
- [4] Tanuma, S.; Powell, C. J.; Penn, D. R. *Surf. Interface Anal.* **1993**, *21*, 165.
- [5] Doniach, S.; Šunjić, M. *J. Phys C: Solid State Phys.* **1970**, *3*, 285.
- [6] Grönbeck, H.; Klacar, S.; Martin, N. M.; Hellman, A.; Lundgren, E.; Andersen, J. N. *Phys. Rev. B* **2012**, *85*, 115445.
- [7] Baraldi, A.; S. Lizzit, S.; Comelli, G.; Kiskinova, M.; Rosei, R.; Honkala, K.; Nørskov, J. K. *Phys. Rev. Lett.* **2004**, *93*, 046101.
- [8] Chabal, Y. J. *Surf. Sci. Rep.* **1988**, *8*, 211.
- [9] Van Hove, M. A.; Moritz, W.; Over, H.; Rous, P. J.; Wander, A.; Barbieri, A.; Materer, N.; Starke, U.; Somorjai, G. A. *Surf. Sci. Rep.* **1993**, *19*, 191.
- [10] Toyoshima, A.; Tanaka, H.; Kikuchi, T.; Amemiya, K.; Mase, K. *J. Vac. Soc. Jpn.* **2011**, *54*, 580.
- [11] Hohenberg, P.; Kohn, W. *Phys. Rev.* **136**, *1964*, B864.
- [12] Kohn, W.; Sham, L. J. *Phys. Rev.* **140**, *1965*, A1133.
- [13] Reuter, K.; Scheffler, M. *Phys. Rev. B* **65**, *2001*, 035406.
- [14] Kitchen, J. R.; Reuter, K.; Scheffler, M. *Phys. Rev. B* **2008**, *77*, 075437.
- [15] Zeng, Z.-H.; Ma, X.-F.; Ding, W.-C.; Li, W.-Z. *Sci. China Chem.* **2010**, *53*, 402.
- [16] Janak, J. F. *Phys. Rev. B* **1978**, *18*, 7165.

## Chapter 3

# Adsorption of Simple Molecules on Platinum-Group Metal Surfaces

---

### 3.1 The Reversible Dense CO Overlayer Formation on Pt(111) Surface

#### Abstract

The high-density CO adsorption phase formed on a Pt(111) surface with exposing to CO gas of sub-Torr ambient was investigated using near-ambient-pressure X-ray photoelectron spectroscopy. The surface coverage was proportional to the background pressure, suggesting a reversible phase transition of CO adsorbed on the surface. Combined results of the experimental data and theoretical calculations reveal the local adsorption configuration of CO molecules in the dense CO overlayer formed under realistic conditions.

#### 3.1.1 Introduction

Platinum (Pt) is regarded as one of the important catalytic material, which has been widely applied to the modern society such as TWC, hydrogenation/oxidation catalysts, fuel-cell catalysts and so on.<sup>1</sup> Adsorption of molecules to surface is the first step relevant for the heterogeneous catalysis. Therefore many researches have performed experiments using surface science techniques to reveal the interactions of Pt surfaces with molecules. In particular the CO/Pt(111) system has been extensively studied since it can be regarded as the simple model system for the fundamental understanding of molecule–metal surface interactions. Even though the practical Pt catalysts work under ambient pressure conditions, most of such studies have been so far conducted under UHV conditions.<sup>2–4</sup>

Thanks to technical developments of high-pressure-compatible surface science, recently a new insight for CO/Pt(111) system has been proposed. A high-pressure scanning tunneling microscopy (HP-STM) study found a dense CO overlayer, denoted by  $(4 \times 4)\text{-}9\text{CO}$ , under a CO oxidation reaction condition at near ambient pressures.<sup>5</sup> However, later this phase was re-interpreted by alternative model as  $(\sqrt{19} \times \sqrt{19})\text{R}23.4^\circ\text{-}13\text{CO}$  (hereafter “ $\sqrt{19}\text{-}13\text{CO}$ ”).<sup>6</sup> A remarkable difference of these models are

existence of hollow site occupation or not. The  $\sqrt{19}$ - $^{13}\text{C}$ O structure has been also reported in CO-bubbled water solutions. It is reported that a significant enhancement of the CO stretching on top site as function of CO pressure from UHV to NAP conditions, with sum frequency generation vibrational spectroscopy (SFG-VS).<sup>7-10</sup> Periodicity and arrangement of the molecular overlayer are documented by STM observations, whereas the adsorption site of the molecule is usually discussed by using VSs. Although the CO adsorption on Pt(111) surface is one of the most fundamental adsorption systems, however, the local adsorption geometry of CO on surface lattice of Pt(111) is still unclear and the detailed structure has not been completely described yet.

Here, in-situ measurements with a synchrotron based x-ray photoelectron spectroscopy (XPS) was performed for the CO/Pt(111) system in the range from UHV to near ambient pressure. Obtained data was analyzed in detail with the aid of theoretical core-level shift (CLS) simulations. It is revealed that CO molecules locate on high-symmetry adsorption sites on Pt(111) surface. The lateral CO-CO repulsion in the dense overlayer induced by the adsorption on high-symmetry-sites can be accommodated via specific tilting of the molecular axis of CO.

### 3.1.2 Experiment and Computational Methodology

Spectroscopic measurements were performed at an undulator soft X-ray BL-13A/B at the Photon Factory of the High Energy Accelerator Research Organization (KEK-PF) in Tsukuba, Japan.<sup>11</sup> A Pt(111) surface was cleaned by the standard procedure; repeated cycles of Ar<sup>+</sup> sputtering and sufficient surface annealing (1200 K). The surface orientation was checked by LEED. A hexagonal (1 × 1) pattern was obtained from the cleaned surface. XP spectra were recorded with photon energies of 150, 370 and 630 eV, for Pt 4f, C 1s and O 1s levels, respectively. Pure CO gas was dosed to the surface at 298 K. XP spectra were deconvoluted into several components via a numerical analysis, where the convoluted function of Doniach-Šunjić and Gaussian and Shirley-type background subtraction were used. Periodic surface structures and corresponding CLSs were simulated by Vienna ab initio simulation package (VASP). The calculated equilibrium lattice constant of fcc-Pt was  $a_0 = 3.97 \text{ \AA}$ , which is slightly longer than the experimental result. Pt metal slab was constructed by a four-layer thickness, where upper two Pt layers are fully relaxed. CO molecules are located on high symmetry adsorption sites. The residual forces on atoms were reduced below  $0.05 \text{ eV \AA}^{-1}$ . The CLSs simulation was performed via the Janak's theorem. Further details are described in section 2.5.4.

### 3.1.3 Results and Discussion

CO adsorption on Pt(111) surface changes the spectral shape of Pt 4f<sub>7/2</sub> level as shown in Figure 3.1.1. The XP spectra taken from clean and CO-saturated surfaces show three types of surface Pt atoms. On

the clean surface, the Pt  $4f_{7/2}$  level consists of two components, which are assigned as the topmost surface layer ( $Pt_0$ ) and the bulk Pt atoms, respectively. The surface was exposed to the 20 Langmuir (L,  $1 \text{ L} = 1 \times 10^{-6} \text{ Torr sec}$ ) of CO under UHV at 298 K, after that the surface is saturated by CO (grey). Two distinct peaks are observed and assigned to bridge site occupation ( $Pt_{1/2}$ ) and top site occupation ( $Pt_1$ ). The gradual evolution of XP spectra is shown in (b), the top site occupation (t) is initially preferred, and then the bridge site occupation (br) increases. The evolution of CO coverage is shown in inset.

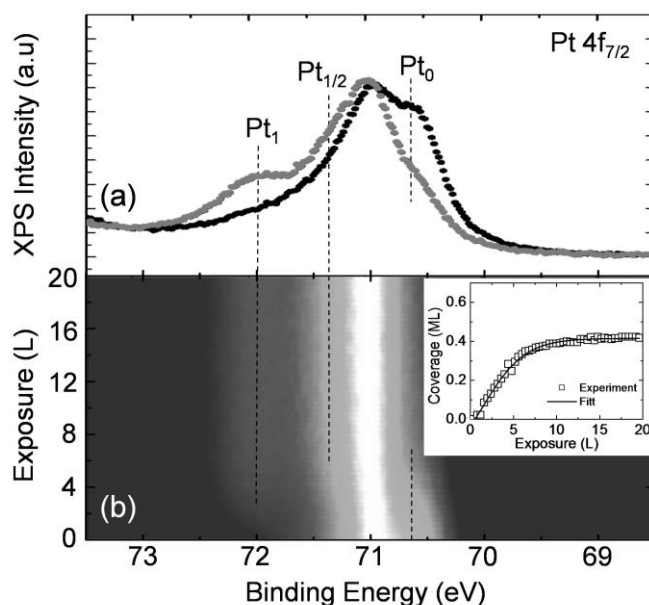


**Figure 3.1.1.** (a) Pt  $4f_{7/2}$  XP spectra taken from CO-free and CO-saturated Pt(111) surfaces. (b) Evolution of Pt  $4f_{7/2}$  level as a function of CO exposure. CO coverage deduced from integrated peak areas (inset).

Figure 3.1.2 shows the curve-fitted XP spectra taken from Pt 4f (a, c and e) and C 1s (b and d) levels for CO adsorption on Pt(111). After 20 L exposure, CO adsorption gives rise to the two CO-induced components in Pt 4f spectra denoted by  $Pt_{1/2}$  and  $Pt_1$ . C 1s XP spectra also exhibit two distinct peaks, which are assigned to CO molecules adsorbed on bridge (286.1 eV) and top (286.8 eV) sites. O 1s level shows two distinct peaks at 531.2 and 532.9 eV attributed to CO on bridge and top sites, which is consistent with the C 1s results. At this moment, Pt 4f level drastically changes; the intensity of component  $Pt_0$  decreases, while two extra components appear at higher binding energy side (c). The CO coverage is estimated from the fractions; CO-bonding surface Pt/all surface Pt, which results in 0.43 monolayer (ML) with respect to the number of surface Pt atoms. The  $c(4 \times 2)$ -2CO structure was formed on the CO-saturated Pt(111) obtained by 20 L CO exposure.<sup>4,7,8</sup> A part of surface Pt atom is

free from CO adsorption even at the saturation coverage.

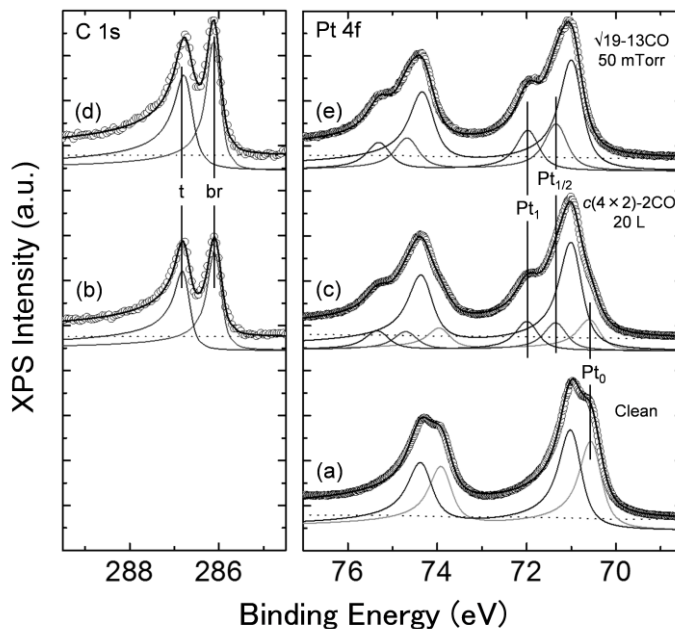
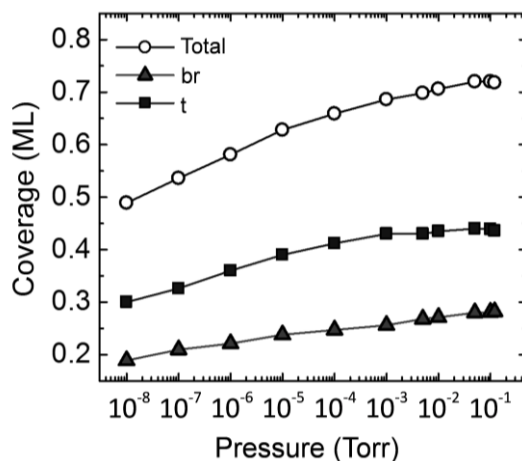


**Figure 3.1.2.** XP spectra Pt 4f and C 1s levels for Pt(111) surface taken under different conditions (clean, 20 L and 50 mTorr) at room temperature. All XP spectra are shown with curve fitting results by  $Pt_0$ ,  $Pt_{1/2}$  and  $Pt_1$  and the bulk component for Pt 4f level and br and t for C 1s level. Assignment of these components is discussed in the main text. Adapted from Ref. P-5 with permission of the PCCP Owner Societies.

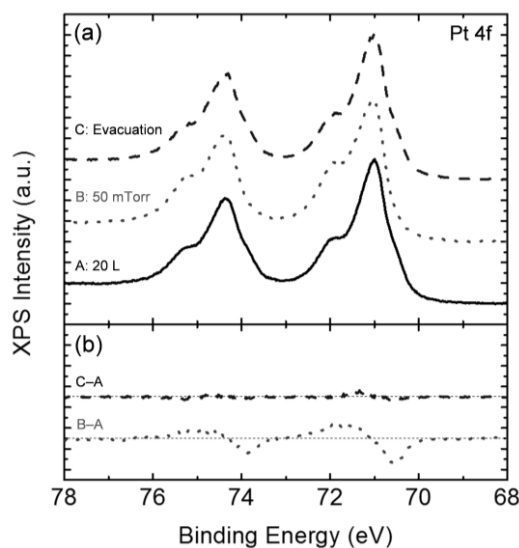
The CO exposure up to 50 mTorr hardly change in the C 1s level (d), however it exhibits two intensities of two components (br and t) increase, and the full width half maximum (FWHM) of top (t) component is broadened, which can be explained by tilting of a part of the top CO as mentioned later. Spectral shape of Pt 4f level significantly changes as shown in (e); CO-free surface Pt ( $Pt_0$ ) disappears, which indicates that all the surface Pt atoms are bound to CO molecules under the higher pressure condition. Consequently, the intensity of CO-binding surface Pt ( $Pt_{1/2}$  and  $Pt_1$ ) are enhanced. It is noted that intensity of  $Pt_{1/2}$  component is slightly larger than that of  $Pt_1$ , which is consistent with the C 1s level.

Figure 3.1.3 shows the evolution of surface CO coverages estimated from peak areas of  $Pt\ 4f_{7/2}$  level as a function of CO pressure from  $10^{-8}$  to  $10^{-1}$  Torr. It is clear that the surface CO coverage continuously increases depending on the CO pressure. the intensity of CO-free surface Pt ( $Pt_0$ ) goes down below the detection limit, when the pressure is raised above 50 mTorr. At the moment the CO coverage reaches the experimental saturation (0.72 ML). The enhancement of top site occupation (~35%) with respect to at  $10^{-7}$  Torr is well consistent with a previous study measured by SFG-VS.<sup>8</sup>

When the CO supply to the surface was turned off, component  $Pt_0$  almost comes back to the original intensity (Figure 3.1.4). The results clearly indicate that the reversibility of the surface coverage and overlayer depending on the CO pressure.



**Figure 3.1.3.** Pressure dependence of the surface CO coverages deduced from Pt  $4f_{7/2}$  level. The fractional coverages of CO on bridge (br) and top (t) are shown by triangle and square plots, respectively, and the total coverage (circle) is a sum of them. Adapted from Ref. P-5 with permission of the PCCP Owner Societies.



**Figure 3.1.4.** Reversibility for the background pressure of CO overlayer. (a) XP spectra for Pt 4f level taken from a Pt(111) surface under an ultrahigh vacuum (UHV) condition after 20 L CO exposure (A), under 50 mTorr CO (B) and after CO evacuation (C). (b) difference spectra of B and C from A. Adapted from Ref. P-5 with permission of the PCCP Owner Societies.

The present experimental data is well explained by the dense  $\sqrt{19-13}\text{CO}$  formation proposed in the previous STM/DFT study.<sup>6</sup> The unit cell of the structure consists of 6 bridge-COs and 7 top-COs

adsorbed on 19 Pt atoms, thus the coverage is 0.68 ML. Here all the surface Pt atoms are connected to CO molecules. The slight discrepancy from the ideal coverage, i.e. the relative enhancement of top-CO, may be explained by the presence of dense top CO molecules at domain boundaries of the  $\sqrt{19}$ -13CO structure. It is emphasized from the core-level spectroscopic point of view that the CO molecules in the  $\sqrt{19}$ -13CO phase are located at only the two high-symmetry sites (top and bridge sites).

Next DFT calculations reveal the lateral interaction results in the displacement from the regular high-symmetry site and tilting of the molecular axis. The adsorption structures of the  $c(4 \times 2)$ -2CO and the  $\sqrt{19}$ -13CO phases are optimized considering the above results with the DFT calculations as illustrated in Figure 3.1.5. CO molecules locate on top and bridge sites with the upright configuration in the  $c(4 \times 2)$ -2CO structure (a). While, there are two types of CO molecules on top sites in  $\sqrt{19}$ -13CO structure (b); one perpendicular CO and six tilting top-COs ( $\sim 11^\circ$ ) in the cell. The tilting angle of bridge-CO is smaller than that of top-CO ( $< 3^\circ$ ). Here the six slightly tilted CO molecules on top sites rotate anti-clockwise around the centered top-CO, though both the clockwise and anti-clockwise rotations are possible.

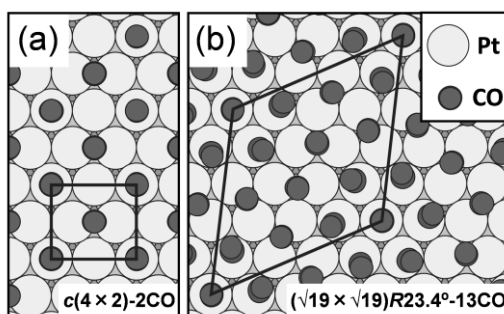


**Figure 3.1.5.** The top views of simulated overlayers of  $c(4 \times 2)$ -2CO (a) and  $\sqrt{19}$ -13CO (b). The black enclosures indicate the unit cells of the structures. Here the surface and molecule are modelled by large and small balls, respectively. Adapted from Ref. P-5 with permission of the PCCP Owner Societies.

The phase transition from  $c(4 \times 2)$ -2CO to  $\sqrt{19}$ -13CO is also concluded in the energetic point of view (Figure 3.1.6). Under the low-pressure conditions, the  $c(4 \times 2)$ -2CO is preferred due to the relative high adsorption energy per molecule. When the chemical potential increases beyond  $-1.0$  eV, the surface switches to taking of the steeper line, resulting in the dense CO overlayer ( $\sqrt{19}$ -13CO) formation. Table 3.1.1 shows the calculated CLSs of Pt 4f and C 1s levels for the two CO structures, with respect to the binding energies of bulk Pt and CO adsorbed on the bridge site. The simulated CLSs are consistent with the experimental results, which further supports the formation of the  $\sqrt{19}$ -13CO phase on the surface.

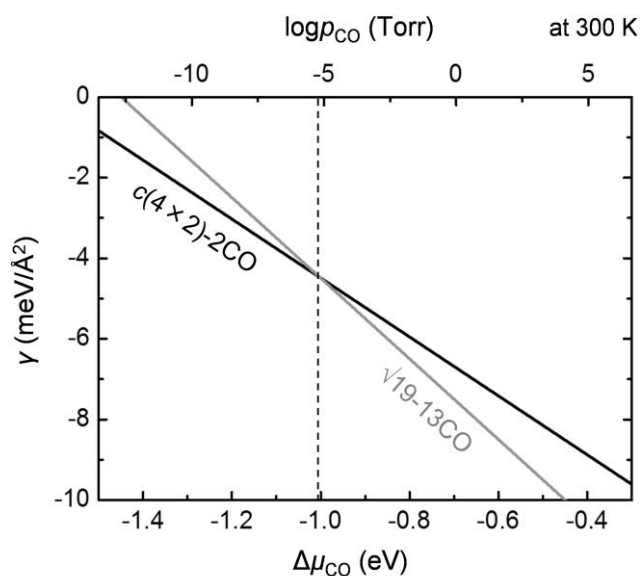


**Figure 3.1.6.** Surface free energies for different CO-induced surface structures formed on Pt(111) as a function of CO chemical potential.

**Table 3.1.1.** Experimental and theoretical CLSs for CO/Pt(111) system. Two model structures of  $c(4 \times 2)$ -2CO and  $\sqrt{19}$ -13CO are simulated here. The CLS values are calibrated with respect to the binding energies of bulk Pt and CO on the bridge site, for Pt 4f and C 1s levels, respectively. Adapted from Ref. P-5 with permission of the PCCP Owner Societies.

system	level	calcd CLS (eV)	exp. CLS (eV)
$c(4 \times 2)$ -2CO	Pt 4f	-0.32	-0.35
		+0.35	+0.34
		+1.17	+0.98
$\sqrt{19}$ -13CO	C 1s	+0.56	+0.7
	Pt 4f	+0.42	+0.34
		+1.15	+0.98
	C 1s	+0.52 (tilted)	+0.7
		+0.45 (uplight)	

The experimental broadening of FWHM of the peak corresponding to the CO on top site in C 1s level is explained by the small lateral displacement of the CO on top site, and resultant change of chemical condition in the  $\sqrt{19}$ -13CO phase. The previous STM study reported by Jensen et al. suggested the

formation of  $(4 \times 4)$ - $\sqrt{3}$ CO incommensurate structure (0.56 ML), which includes two hollow COs per unit cell.<sup>5</sup> However, the CLS simulation does not support the hollow site occupation, which exhibits almost zero shift in Pt 4f level.

### **3.1.4 Conclusion**

In summary, using the NAP-XPS techniques paralleled with DFT calculations, the behaviour of CO/Pt(111) system is studied under CO pressures up to 100 mTorr at room temperature. The chemical analysis revealed that the CO molecules in dense CO overlayer are located at the top and bridge sites on the Pt(111) surface. The formation of the incommensurate CO adsorption was ruled out in the present in-situ XPS observation. The DFT simulations reveal the slight shift of CO molecules from the regular top site (< 27% of Pt atomic radius) and tilted by approximately  $11^\circ$  from the surface normal along clockwise or anti-clockwise rotated directions in the  $\sqrt{19}$ - $\sqrt{13}$ CO overlayer.

## References

- [1] J. W. Döbreiner, *Schweigg J.* **1823**, *39*, 1.
- [2] Björneholm, O.; Nilsson, A.; Tillborg, H.; Bennich, P.; Sandell, A.; Herdnäs, B.; Puglia, C.; Mårtensson, N. *Surf. Sci. Lett.* **1994**, *315*, L983.
- [3] Kinne, M.; Fuhrmann, T.; Whelan, C. M.; Zhu, J. F.; Pantförder, J.; Probst, M.; Held, G.; Denecke, R. Steinrück, H.-P. *J. Chem. Phys.* **2002**, *117*, 10852.
- [4] Yang, H. J.; Minato, T.; Kawai, M.; Kim, Y. *J. Phys. Chem. C* **2013**, *117*, 16429.
- [5] Jensen, J. A.; Rider, K. B.; Salmeron, M.; Somorjai, G. A. *Phys. Rev. Lett.* **1998**, *80*, 1228.
- [6] Vestergaard, E. K.; Thostrup, P.; An, T.; Lægsgaard, E.; Stensgaard, I.; Hammer, B.; Besenbacher, F. *Phys. Rev. Lett.* **2002**, *88*, 259601.
- [7] Somorjai, G. A.; York, R. L.; Butcher, D.; Park, J. Y. *Phys. Chem. Chem. Phys.* **2007**, *9*, 3500.
- [8] Su, X.; Cremer, P. S.; Shen, Y. R.; Somorjai, G. A. *Phys. Rev. Lett.* **1996**, *77*, 3858.
- [9] Rupprechter, G.; Dellwig, T.; Unterhalt, H.; Freund, H.-J. *J. Phys. Chem. B* **2001**, *105*, 3797.
- [10] Villegas, I.; Weaver, M. J. *J. Chem. Phys.* **1994**, *101*, 1648.
- [11] Toyoshima, A.; Tanaka, H.; Kikuchi, T.; Amemiya, K.; Mase, K. *J. Vac. Soc. Jpn.* **2011**, *54*, 580.



## 3.2 The Irreversible Phase Transition of Adsorbed NO on Rh(111) Surface

### Abstract

The adsorption of nitric oxide (NO) on Rh(111) surface has been investigated under the pressure ranging from UHV up to 100 mTorr. The surface chemical and structural properties were revealed by the combination of NAP-XPS, LEED and DFT simulation. The experimental and computational results indicate that several ordered NO overlayers are formed on Rh(111) at low-temperature and under UHV conditions, which are consistent with the previous reports. While at room temperature and under 100 mTorr NO pressure, a part of NO molecules dissociate to atomic species, i.e. N and O. Furthermore, the N atoms are continuously removed from the surface by the chemical reaction with NO. Consequently, the surface is covered by NO + O phase(s). Interestingly, the phase(s) has well-ordered ( $2 \times 2$ ) periodicity, with including NO and O in a unit cell.

### 3.2.1 Introduction

The adsorption of nitric oxide (NO) on Rh surfaces has been studied extensively because Rh is a good catalyst for the reduction of nitroxides.<sup>1-25</sup> Recently, various high-density overlayers of simple molecules have been found under high pressure exposure, and its catalytic activity have been debated using high pressure surface science techniques.<sup>18-28</sup> Rider et al. found that a dense adsorption structure of ( $3 \times 3$ ) periodicity formed under high background using high-pressure scanning tunneling microscopy (HP-STM).<sup>18</sup> The formation of dense overlayer, which consists of 7 NO molecules (hollow : top = 6 : 1) per unit cell, is supplemented by a DFT study.<sup>19</sup> On the other hand, Wallace et al. reported only one vibration signal assigned to top-NO was observed due to the site blocking by dissociated species under 1 Torr NO presence.<sup>21</sup> Since the dissociation of NO molecules on the surface has not been well characterized, the whole picture of the system is less understood. Thus the chemical identification of the adsorbates including dissociated species is requested to improve the understanding of high-pressure-NO-induced phases.

NAP-XPS provides chemical information on both substrate and adsorbate over the wide pressure and temperature ranges. A combination with DFT based calculations makes it possible to characterize the electronic and geometric structures for the observed adsorption system with a good accuracy.

Here it is reported that NO adsorption behavior on a Rh(111) surface as a function of pressure from UHV to 100 mTorr NO ambient. Experimental results (NAP-XPS and LEED) are paralleled by computational simulations. It was found an irreversible formation of a mixed overlayer of NO and

atomic O by a high-pressure NO exposure. This mixed overlayer is formed via dissociation of NO and selective removal of atomic N. This finding provides an understanding of the puzzled NO-induced structure reported previously and may contribute to further development of the industrially important Rh catalyst for NO reduction.

### 3.2.2 Experimental and Computational Methodology

A clean Rh(111) surface (SPL, 8 mm $\phi$   $\times$  1 mm, 99.995% quality) was prepared by a standard procedure; repeated cycles of the Ar<sup>+</sup> sputtering at 1 kV at room temperature for 20 min, a brief annealing with an electron beam heating to  $\sim$ 1300 K, following an O<sub>2</sub> treatment at 1000 K for 5 min. XPS measurements were performed at beamline 13A/B at KEK-PF.<sup>34</sup> The base pressures of the analysis chamber and the separated sample preparation chamber were in the order of 10<sup>-10</sup> Torr. Pure NO gas (Takachiho chemical industrial, 99.9%) was introduced to the analysis chamber up to 1 Torr via a variable metal leak valve. Contaminations, which sometimes affect the surface chemical condition, in the NO gas was checked by using a MS monitoring at a NO pressure of 10 mTorr. The MS signals of O<sub>2</sub> (m/e = 32), N<sub>2</sub>O (44), NO<sub>2</sub> (46) were under the detection limit.

The incident photon energies were tuned to detect information from similar physical origin beneath the surface (i.e. O 1s, 650 eV; N 1s, 500 eV; Rh 3d<sub>5/2</sub>, 400 eV). The binding energy scale was calibrated with respect to the Fermi-edge. Since the photoemission intensity is attenuated by ambient-pressure gas, the O 1s and N 1s intensities were normalized by the integrated intensity of Rh 3d<sub>5/2</sub> photoelectrons from the Rh substrate. X-ray irradiation effects on adsorbed layers were checked and the absence of such effects was confirmed. The XP spectra were deconvoluted using a convolution function of Doniach-Šunjić and Gaussian line shapes, and Shirley-type background subtraction.

For DFT based calculations, VASP was employed. A projector augmented wave (PAW) method was used with a plane wave cutoff energy of 400 eV for electron-ion interactions. The generalized gradient approximation (GGA)-Perdew-Burke-Ernzerhof (PBE) was used for the exchange-correlation functional. The Rh metal slab was modeled by seven layer thickness. Brillouin zone integration of (9  $\times$  9  $\times$  1) Monkhorst-Pack k-point mesh was applied for the (2  $\times$  2) super-cell. We used coequal k-point meshes for the other super-cells to be the same density. For the bare Rh metal, the calculated equilibrium lattice constant was  $a_0 = 3.82$  Å, that was slightly larger than an experimental value of 3.80 Å. Adsorbates were placed on both sides of surfaces to reduce a long-range dipole-dipole interaction. Then the first to third Rh layers of both side surfaces and adsorbed molecules are fully relaxed, whereas the middle Rh layer is fixed to the bulk lattice constant. Although there is a small margin for each adsorption structure, the adsorbed NO molecules basically have the perpendicular configuration to the surface even after relaxation process. Binding energies of core electrons and the resultant CLSs were estimated using the Slater-Janak transition approach.<sup>24</sup>

### 3.2.3 Results and Discussions

#### NO adsorption under UHV condition

First, LEED patterns were obtained from clean and NO-covered Rh(111) surfaces with different coverage at 155 K as shown in Figure 3.2.1. Just after surface cleaning, a sharp  $(1 \times 1)$  pattern was observed as shown in (a). The model structure is illustrated in the right panel (b). While NO dose under UHV condition induces two types of ordered structures depending on exposure. Since NO dissociation to atomic nitrogen (N) and oxygen (O) is ruled out at 155 K, the ordered structures consist of only NO molecules. Figure 3.2.1(c) shows a LEED pattern taken after 3 Langmuir (L,  $1 \text{ L} = 1 \times 10^{-6} \text{ Torr sec}$ ) exposure at 155 K.<sup>3</sup> The formation of the  $c(4 \times 2)$  orientation is identified (c).

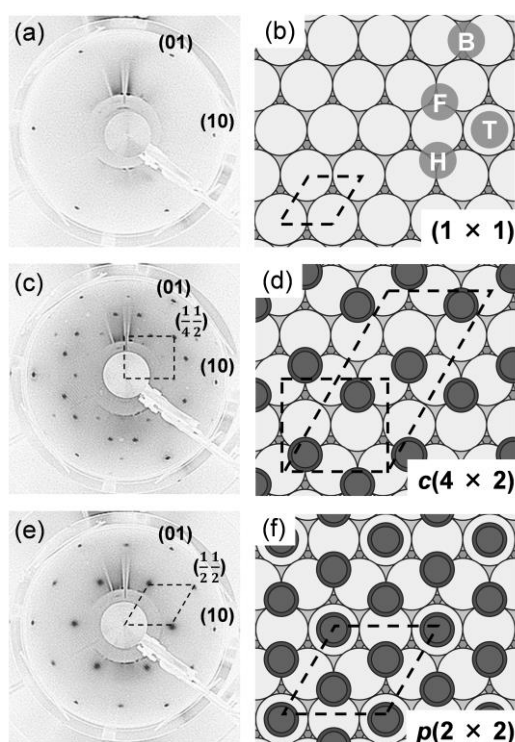


**Figure 3.2.1** Observed LEED patterns from clean and NO-exposed Rh(111) surfaces and corresponding model structures; clean surface (a and b), NO exposure of 3 L (c and d) and 60 L (e and f). The substrate was cooled down to 155 K. Here the electron energy  $E$  of 73 eV was applied. Dashed tetragons show unit cells of the NO-induced superstructure. High-symmetry sites for adsorption are indicated in (b) as fcc-hollow (F), hcp-hollow (H), bridge (B) and top (T). Adapted with permission from Ref. P-6. Copyright (2015) American Chemical Society.

In right panel (d), the corresponding model is shown; two NO molecules are adsorbed at the hcp- and fcc-hollow sites in a unit cell, resulting in a coverage of 0.50 monolayers (ML).<sup>3,4,7,8,17</sup> Further NO

exposure up to 60 L leads to a phase transformation to  $p(2 \times 2)$  (e) and the pattern no longer change even under continuous dosing at  $10^{-7}$  Torr. The atomistic model of the surface is shown in (f), although the present result cannot exclude coexistence of a  $p(2 \times 2)$ -2NO and a  $p(2 \times 2)$ -3NO structures. Further details of this phase is discussed by XPS as described later. The adsorption energies for NO, N and O on each site were estimated using DFT calculation (Table 3.2.1). At 0.25 ML, NO molecule prefers the hcp-hollow (H) site. The order of adsorption energy for each site is as follows; H > fcc-hollow (F) > bridge (B) > top (T). The average adsorption energies of the possible NO overlayers at 0.5 and 0.75 ML are also shown in the table.

**Table 3.2.1.** Calculated adsorption energies of NO, N and O on Rh(111). The adsorption energies are estimated with respect to gas-phase free molecule. Several adsorption phases of NO, N and O with different structures are considered. Adapted with permission from Ref. P-6. Copyright (2015) American Chemical Society.

Coverage (ML)	System	NO (eV)	N (eV)	O (eV)
0.25	$p(2 \times 2)$ (H)	-2.41	-0.202	-1.94
	$p(2 \times 2)$ (F)	-2.31	-0.0379	-2.00
	$p(2 \times 2)$ (B)	-2.27	-	-
	$p(2 \times 2)$ (T)	-1.93 <sup>a</sup>	-	-0.575
0.50	$c(4 \times 2)$ (HF)	-2.41		
	$p(2 \times 2)$ (HF)	-2.33		
0.75	$p(2 \times 2)$ (HFT)	-2.07 <sup>b</sup>		

<sup>a</sup> NO molecule at on-top site has the upright configuration.

The average adsorption energy per molecule results in -2.41, -2.33 and -2.07 eV for the  $c(4 \times 2)$ -2NO,  $p(2 \times 2)$ -2NO and  $p(2 \times 2)$ -3NO, respectively. These adsorption energies are consistent with previous DFT calculation results.<sup>4,17,19</sup>

Figure 3.2.2 shows XP spectra for O 1s, N 1s and Rh 3d<sub>5/2</sub> levels taken after exposures of 0, 5 and 60 L. The bottom three spectra shown in Fig. 2 (a, b and c) correspond to a clean Rh(111) surface. The O 1s and N 1s spectra in Figure 3.2.2 (a and b) show no peak, while in the Rh 3d<sub>5/2</sub> spectrum of Fig. 3.2.2(c) a fitting analysis reveals two distinct components at 306.8 eV and 307.3 eV. The signal at lower binding energy side is attributed to the first-layer Rh atoms (denoted by Rh<sub>0</sub>), whereas the higher one is assigned as the bulk Rh atoms including a contribution from the second layer.<sup>31-33</sup>

The middle three spectra of Figure 3.2.2(d, e and f) were measured after 5 L exposure at 155 K. At this moment, a single peak is visible in the O 1s level (d) which is assigned to NO molecules at the

hcp- and fcc-hollow sites.<sup>14</sup> The N 1s level (e) also indicates that the adsorption of NO molecule at binding energy of 400.3 eV.<sup>14,20,24</sup> The Rh 3d<sub>5/2</sub> level (f) exhibits a spectral change; the surface component shifts to the higher binding energy side, and it splits into two components at 307.1 and 307.5 eV indicating that two Rh atoms with different chemical states are induced by the NO adsorption on the surface. We attribute the lower and higher binding energy components to the Rh atoms bonded by one and two NO molecule(s), respectively, at the hollow site(s). Since one NO molecule is shared by three Rh atoms, the effective coordination number of the Rh atom is 1/3 (Rh<sub>1/3</sub>) or 2/3 (Rh<sub>2/3</sub>). If the complete c(4 × 2)-2NO phase covers the surface, the peak ratio of Rh<sub>2/3</sub>/Rh<sub>1/3</sub> should be 1, however the actual value is estimated to 1.4, which suggests that the a more dense adsorption of NO on the surface and/or a photoelectron diffraction modulates the intensities.

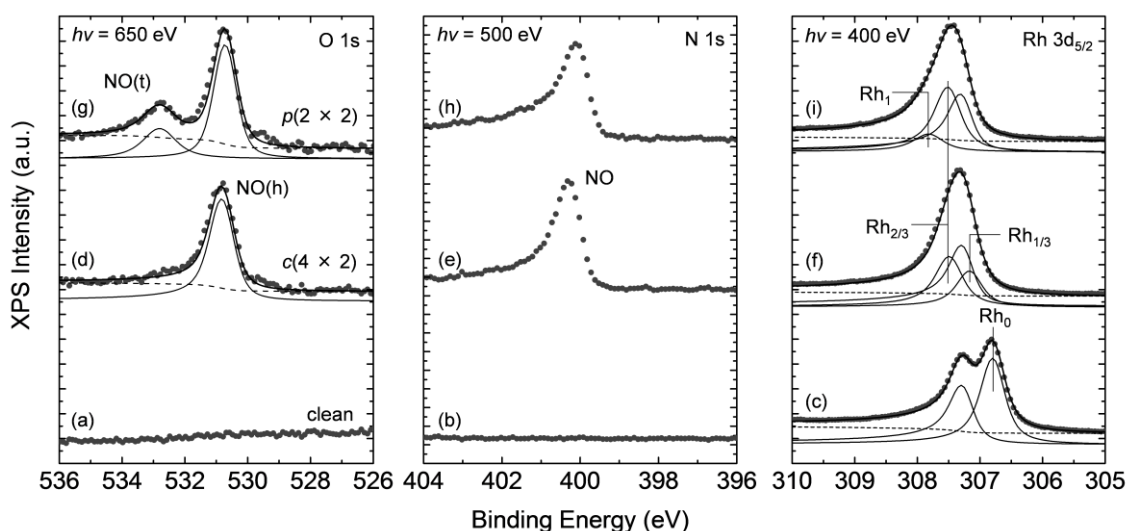


**Figure 3.2.2.** XP spectra from O 1s, N 1s and Rh 3d<sub>5/2</sub> levels from a Rh(111) surface taken under different surface conditions (i.e. before and after NO gas exposures). The photon energies are indicated in each figure. The bottom spectra were taken from a clean Rh(111) surface (a, b and c). NO adsorption phases with a c(4 × 2) structure (d, e and f) and a p(2 × 2) structure (g, h and i) were prepared by NO exposures of 5 and 60 L, respectively. The substrate temperature was kept at 155 K. O 1s and Rh 3d<sub>5/2</sub> spectra were deconvoluted into distinct components (solid black lines). The dark gray plots show the experimental result, and the bold black line is a sum of the fitting curves, while, the black dashed line indicates a background. Adapted with permission from Ref. P-6. Copyright (2015) American Chemical Society.

The upper three spectra of Figure 3.2.2(g, h and i) were recorded after 60 L NO exposure at 155 K, which guarantees the surface coverage reaches the saturation. The O 1s XP level (g) shows the appearance of a new peak at 532.8 eV which is assigned to NO molecules located at top sites.<sup>14</sup> The surface coverage of NO on hollow sites keeps unchanged in intensity (0.50 ML). Based on this value,

the surface coverage of NO on top site is estimated to be 0.20 ML. Therefore the total surface coverage is 0.70 ML. If the  $p(2 \times 2)$ -3NO phase completely covers the surface, the surface coverage reaches 0.75 ML (see Figure 3.2.1(f)). The discrepancy may be explained by coexistence of the  $p(2 \times 2)$ -2NO (0.50 ML) and  $p(2 \times 2)$ -3NO structures.<sup>7,8</sup> Another explanation for this is the presence of domain boundaries of the  $p(2 \times 2)$ -3NO structure,<sup>4</sup> The spectral shape of N 1s level (h) is less sensitive to the difference of adsorption site, but a slightly shifts to lower binding energy side ( $\sim -0.2$  eV) is seen. As discussed above, the NO/Pd(100) system shows a negative shift in N 1s level. The Rh 3d<sub>5/2</sub> level (i) shifts to the higher binding energy side. The Rh<sub>1/3</sub> component completely disappears, whereas the Rh<sub>2/3</sub> one increases in intensity, and a new component appears at 307.8 eV, which is attributed to Rh atoms bonding with NO on top site (Rh<sub>1</sub>). The experimental intensity ratio of Rh<sub>1</sub>/Rh<sub>2/3</sub> is 0.27, which is a little smaller than the ideal value of 0.33 and associated with incomplete transformation to the  $p(2 \times 2)$ -3NO phase due to the domain boundaries.

In order to confirm peak assignments, CLSs of Rh 3d<sub>5/2</sub> level were simulated for the  $c(4 \times 2)$ -2NO and  $p(2 \times 2)$ -3NO structures. Table 3.2.2 shows comparison of calculated and experimental CLSs based on the Rh bulk.. The simulated CLS values are in good agreement with experimental ones. Thus the present XPS results for the  $c(4 \times 2)$ -2NO and  $p(2 \times 2)$ -3NO phases support the previously proposed structure models formed under UHV conditions.<sup>3-10</sup>

**Table 3.2.2.** Calculated and experimental CLSs of Rh 3d<sub>5/2</sub> level for clean and NO-adsorbed Rh(111) surfaces. For the NO/Rh(111) surfaces, the  $c(4 \times 2)$ -2NO (0.50 ML) and  $p(2 \times 2)$ -3NO (0.75 ML) structures were assumed for the calculations. All the CLSs are indicated with respect to the bulk Rh atom. Adapted with permission from Ref. P-6. Copyright (2015) American Chemical Society.

Coverage (ML)	label	calcd CLS (eV)	exp. CLS (eV)
0	Rh <sub>bulk</sub>	0.0	0.0
	Rh <sub>0</sub>	-0.46	-0.5
0.50	Rh <sub>1/3</sub>	-0.27	-0.2
	Rh <sub>2/3</sub>	+0.10	+0.2
0.75	Rh <sub>2/3</sub>	+0.07	+0.2
	Rh <sub>1</sub>	+0.57	+0.5

### NO adsorption in gas equilibrium under a NAP condition

Next, in-situ XPS measurements were performed under a NAP condition at room temperature. It is noted that the temperature of UHV and NAP experiments were different (room temperature and 155 K). Thus the sticking coefficient and adsorption process may be changed. Figure 3.2.3 shows XP

spectra taken under in-situ (100 mTorr NO ambient) and ex-situ (after gas evacuation) conditions. An additional component appears at 529.5 eV in O 1s level, which is originating from NO dissociation to the atomic O (a).<sup>11,33</sup> This assignment is supported by the XP spectra taken from the O-covered Rh(111) surface (see Figure 3.2.4). At room temperature, a part of NO dissociates to the atomic species even under  $10^{-7}$  Torr NO ambient, so the dissociation is not high-pressure induced effect. Therefore the atomic O could be generated by NO dissociation at the initial stage of high pressure NO dose at room temperature.

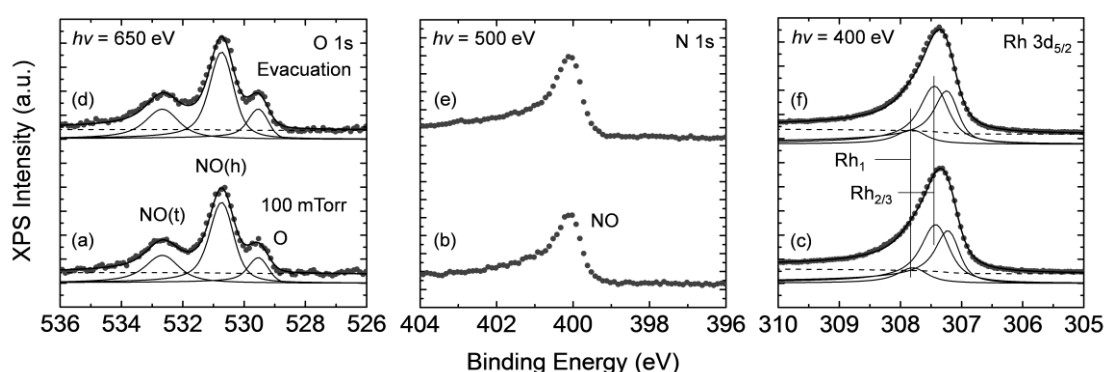


**Figure 3.2.3.** XP spectra from O 1s, N 1s and Rh 3d<sub>5/2</sub> core levels from a Rh(111) surface taken under 100 mTorr of NO at RT (a, b and c) and after NO gas evacuation and cooled down to 155 K (d, e and f). The photon energies are indicated in each figure. O 1s and Rh 3d<sub>5/2</sub> spectra were deconvoluted into several components. Adapted with permission from Ref. P-6. Copyright (2015) American Chemical Society.

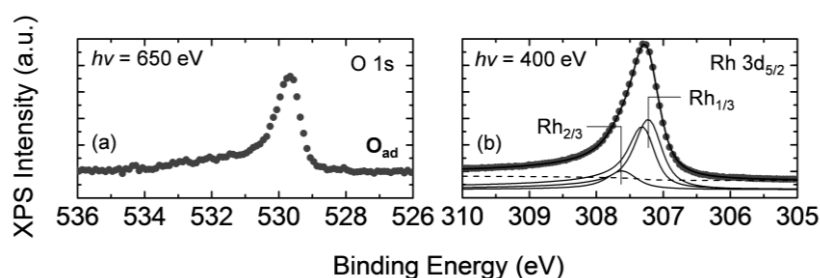


**Figure 3.2.4.** XP spectra from O 1s (a) and Rh 3d<sub>5/2</sub> (b) levels from an O-adsorbed Rh(111) surface at RT. Irradiated photon energies are indicated in each figure. Adapted with permission from Ref. P-6. Copyright (2015) American Chemical Society.

Besides, it can be recognized that NO molecules adsorb on both of the hollow and top sites. As a result, the atomic O and molecular NO coexist on the surface under 100 mTorr NO ambient. Here the experimental surface coverage is estimated to be 0.71 ML. While, the atomic N is under the detection

limit in N 1s level (Figure 3.2.3(b)), suggesting that the atomic N is removed from the surface after dissociation. Since the N<sub>2</sub> recombination reaction occurs above 500 K on Rh(111),<sup>1,2</sup> the channel should not be dominant in this regime. It is noted that the atomic N was detected under (after) the 10<sup>-7</sup> Torr exposure. It indicates that the presence of high-pressure NO is a key factor to the removal of atomic N. Another channel for the atomic N removal is the formation of N<sub>2</sub>O by the reaction with gaseous NO.<sup>9</sup> Such atomic N removal has been also reported in previous experiments performed on Pd(100)<sup>24</sup> and Pt(111)<sup>25</sup>. The Rh 3d<sub>5/2</sub> level is curve fitted into three components (denoted by bulk, Rh<sub>2/3</sub> and Rh<sub>1</sub>). The line shape and fitting result of Rh 3d<sub>5/2</sub> level is very similar to that for the p(2 × 2)-3NO phase shown in Figure 3.2.2(i). Another important point is that the XP spectra hardly changed between in-situ and ex-situ (*P*<sub>background</sub> ~ 10<sup>-8</sup> Torr) conditions. It suggests that the chemical conditions between 100 mTorr ambient and UHV remain unchanged.

Figure 3.2.5(a) shows a difference XP spectrum estimated from O 1s level between the 100 mTorr ambient and the 60 L exposure of NO. From the spectrum it is clear that the NO on hollow site is replaced by the atomic O, since the amounts of decrease of NO and increase of O are compatible.

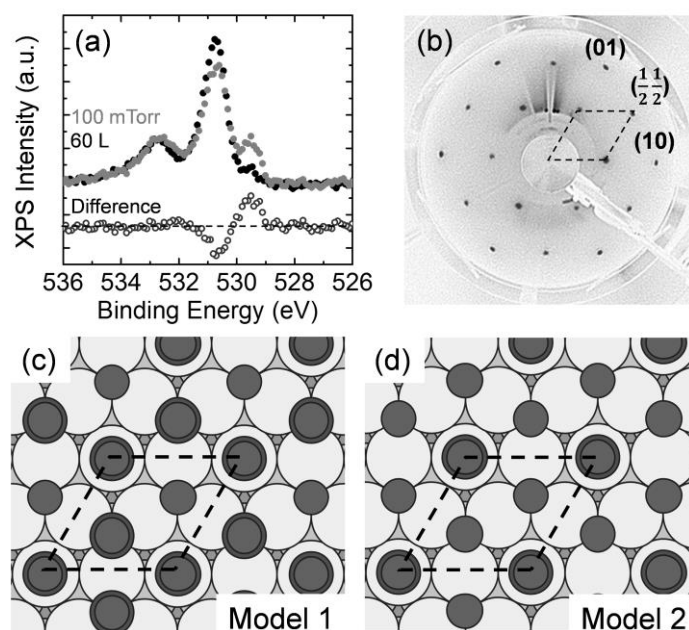


**Figure 3.2.5.** (a) The difference spectrum (open circle) of O 1s level is obtained by subtraction of the spectrum taken after 60 L exposure (black filled circle; Fig. 2(g)) from the spectrum taken under 100 mTorr dosing condition (gray filled circle; Fig. 3(a)). An ex-situ LEED pattern from a Rh(111) surface at 155 K taken after NO gas evacuation (b). The electron energy *E* of 80 eV was applied. (c), (d): Structure models for adsorption phases on Rh(111) formed by the high-pressure NO treatment (see text). Adapted with permission from Ref. P-6. Copyright (2015) American Chemical Society.

Whereas the NO on top site shows no difference, indicating that it keeps the same adsorption states independent of background chemical condition. If the NO domains are separated from the O domains, the intensity of NO on top site is also changed in the same manner as that for the NO on hollows site. Furthermore, if the chemisorbed O forms two-dimensional islands, the Rh 3d<sub>5/2</sub> level should give a lower binding energy component than the bulk one (see Figure 3.2.4).<sup>33</sup> however the obtained spectrum does not show such a lower binding energy component. Figure 3.2.5(b) shows an ex-situ LEED pattern obtained from the NO/O mixed phase after NO evacuation. The surface exhibits a clear p(2 × 2) pattern, which indicates that the NO/O mixed phase has a well-ordered structure. Since all the ex-situ XP spectra (O 1s, N 1s and Rh 3d<sub>5/2</sub> levels) taken after NO evacuation essentially unchanged compared with corresponding in-situ spectra (Figure 3.2.3), it is most likely that the NO/O mixed phase has the same ordered structure under the presence of 100 mTorr ambient. A previous high-pressure STM measurements also observed a p(2 × 2) structure formed under a similar NO ambient conditions.<sup>18</sup> The fractional surface coverages of NO and O on hollow sites are estimated to be 0.38 and 0.12 ML, respectively. Therefore the fractional ratio of p(2 × 2)-3NO and the NO/O phases is almost one to one, if they coexist on the surface. The molecular dissociation to the atomic species needs unoccupied hollow sites, whereas the pre-adsorbed NO suppresses the dissociation due to a lack of vacant sites for the dissociated species. Thus the molecular adsorption and dissociation of NO are competitive processes on the Rh(111) surface. In fact, the coverage of dissociated species (atomic O on hollow site) does not reach the saturation (0.25 ML) and the hollow sites are occupied by both NO and atomic O. The fractional coverages of NO and O on hollow sites may be kinetically influenced by the NO pressure and the substrate temperature. There is a possibility of the formation of p(3 × 3)-7NO (0.78 ML) phase, which was identified under high-pressure NO conditions by HP-STM.<sup>18</sup> In this phase, the hollow/top intensity ratio should be 6 in O 1s level. However, the enhancement of NO on hollow site was not recognized in the present experimental setup.

A previous PM-IRAS study observed the replacement of NO on hollow site with dissociated species,<sup>21</sup> which is well consistent with present results that the replacement by O atom takes place under the high pressure conditions. However, the PM-IRAS study reported disappearance of the signal of NO on hollow site. The lack of the NO on hollows site may be explained in terms of dipole weakening of the NO on hollow site due to electronic effects arising from coadsorption with NO on top site as was seen for NO/Pt(111).<sup>16</sup>

From all the experimental results and simulated adsorption energies, adsorption models for the NO/O mixed phase with the p(2 × 2) periodicity are proposed as shown in Figure 3.2.5(c and d). In Model 1, two NO molecules occupy the hcp-hollow and top sites whereas an O atom occupies the fcc-hollow site per unit cell. In model 2, an NO molecule locates on the top site and two O atoms are both on the hcp- and fcc- hollow sites. Table 3.2.3 shows the simulated CLSs for the two NO/O mixed phases. The surface Rh atoms bonding to both the hollow-NO and hollow-O and bonding to two

hollow-Os are denoted by Rh<sub>2/3-NO/O</sub> and Rh<sub>2/3-2O</sub>, respectively. The CLS values of model 1 is in better agreement with the experimental ones. It is noted that in this phase a part of the fcc-hollow sites is specifically replaced by atomic O with respect to the p(2 × 2)-3NO phase. This replacement is attained by NO dissociation and subsequent removal of atomic N, latter of which proceeds via reaction with NO. In this sense this replacement is not a physical replacement induced by collision and displacement but a chemically-driven replacement.

**Table 3.2.3.** The calculated and experimental CLSs of Rh 3d<sub>5/2</sub> level of NO/O/Rh(111) systems. All the CLSs are indicated with respect to the bulk Rh atom. Adapted with permission from Ref. P-6. Copyright (2015) American Chemical Society.

Model	label	calcd CLS (eV)	exp. CLS (eV)
1: p(2 × 2)-2NO/O	Rh <sub>2/3-NO/O</sub>	+0.17	+0.2
	Rh <sub>1</sub>	+0.60	+0.5
2: p(2 × 2)-NO/2O	Rh <sub>2/3-2O</sub>	+0.35	+0.2
	Rh <sub>1</sub>	+0.62	+0.5

### 3.2.4 Conclusions

The pressure dependence of NO overlayer formed on the Rh(111) surface at different background pressures and temperatures was investigated with both in-situ and ex-situ XPS observations. It is revealed that a part of NO dissociates to atomic species and a high-pressure NO dose lead to a formation of a stable NO/O mixed phase, whereas the N atom is chemically removed from the surface. From LEED observation and computational simulation, the NO/O mixed phase has a p(2 × 2) structure where two NO molecules sit on the hcp-hollow site and the top site and one O atom on the fcc-hollow site.

## References

- [1] Root, T. W.; Schmidt, L. D.; Fisher, G. B. *Surf. Sci.* **1983**, *134*, 30.
- [2] Root, T. W.; Fisher, G. B.; Schmidt, L. D. *J. Chem. Phys.* **1986**, *85*, 4679.
- [3] Castner, D. G.; Sexton, B. A.; Somorjai, G. A. *Surf. Sci.* **1978**, *71*, 519.
- [4] Hermse, C. G. M.; Frechard, F.; van Bavel, A. P.; Lukkien, J. J.; Niemantsverdriet, J. W.; van Santen, R. A.; Jansen, A. P. *J. Chem. Phys.* **2003**, *118*, 7081.
- [5] Kim, Y. J.; Thevuthasan, S.; Herman, G. S.; Peden, C. H. F.; Chambers, S. A.; Belton, D. N.; Permana, H. *Surf. Sci.* **1996**, *359*, 269.
- [6] Zasada, I.; Van Hove, M. A.; Somorjai, G. A. *Surf. Sci.* **1998**, *418*, L89.
- [7] Hagelaar, J. H. A.; Flipse, C. F. J.; Jansen, A. P. *J. Phys.: Conf. Ser.* **2007**, *61*, 379.
- [8] Hagelaar, J. H. A.; Jansen, A. P. J.; Flipse, C. F. J. *Phys. Rev. B* **2009**, *79*, 115414.
- [9] Nakai, I.; Kondoh, H.; Shimada, T.; Nagasaka, M.; Yokota, R.; Katayama, T.; Amemiya, K.; Orita, H.; Ohta, T. *J. Phys. Chem. C* **2009**, *113*, 13257.
- [10] Beniya, A.; Koitaya, T.; Kondoh, H.; Mukai, K.; Yoshimoto, S.; Yoshinobu, J. *J. Chem. Phys.* **2009**, *131*, 084704.
- [11] Esch, F.; Baraldi, A.; Comelli, C.; Lizzit, S.; Kiskinova, M.; Cobden, P. D.; Nieuwenhuys, B. E. *J. Chem. Phys.* **1999**, *110*, 4013.
- [12] Lizzit, S.; Baraldi, A.; Cocco, D.; Comelli, G.; Paolucci, G.; Rosei, R.; Kiskinova, M. *Surf. Sci.* **1998**, *410*, 228.
- [13] Kostelník, P.; Šikola, T.; Varga, P.; Schmid, M. *J. Phys.: Condens. Matter* **2009**, *21*, 134005.
- [14] Zhu, J. F.; Kinne, M.; Fuhrmann, T.; Denecke, R.; Steinrück, H.-P. *Surf. Sci.* **2003**, *529*, 384.
- [15] Matsumoto, M.; Fukutani, K.; Okano, T. *Surf. Sci.* **2012**, *606*, 1489.
- [16] Aizawa, H.; Morikawa, Y.; Tsuneyuki, S.; Fukutani, K.; Ohno, T. *e-J. Surf. Sci. Nanotech.* **2007**, *5*, 122.
- [17] Zeng, Z.-H.; Da Silva, J. L. F.; Li, W.-X. *Phys. Chem. Chem. Phys.* **2010**, *12*, 2459.
- [18] Rider, K. B.; Hwang, K. S.; Salmeron, M.; Somorjai, G. A. *Phys. Rev. Lett.* **2001**, *86*, 4330.
- [19] Popa, C.; Flipse, C. F. J.; Jansen, A. P. J.; van Santen, R. A.; Sautet, P. *Phys. Rev. B* **2006**, *73*, 245408.
- [20] Requejo, F. G.; Hebenstreit, E. L. D.; Ogletree, D. F.; Salmeron, M. *J. Catal.* **2004**, *226*, 83.
- [21] Wallace, W. T.; Cai, Y.; Chen, M. S.; Goodman, D. W. *J. Phys. Chem. B* **2006**, *110*, 6245.
- [22] Ozensoy, E.; Hess, C.; Loffreda, D.; Sautet, P.; Goodman, D. W. *J. Phys. Chem. B* **2005**, *109*, 5414.
- [23] Vang, R. T.; Wang, J.-G.; Knudsen, J.; Schnadt, J.; Lægsgaard, E.; Stensgaard, I.; Besenbacher, F. *J. Phys. Chem. B* **2005**, *109*, 14262.
- [24] Toyoshima, R.; Yoshida, M.; Monya, Y.; Suzuki, K.; Amemiya, K.; Mase, K.; Mun, B. S.; Kondoh, H. *Surf. Sci.* **2013**, *615*, 33.
- [25] Shimada, T.; Simon, B. S.; Nakai, I. F.; Banno, A.; Abe, H.; Iwasawa, Y.; Ohta, T.; Kondoh, H. *J. Phys. Chem. C* **2010**, *114*, 17030.
- [26] Jensen, J. A.; Rider, K. B.; Salmeron, M.; Somorjai, G. A. *Phys. Rev. Lett.* **1998**, *80*, 1228.
- [27] Longwitz, S. R.; Schnadt, J.; Vestergaard, E. K.; Vang, R. T.; Lægsgaard, E.; Stensgaard, I.; Brune, H.; Besenbacher, F. *J. Phys. Chem. B* **2004**, *108*, 14497.
- [28] Tao, F.; Dag, S.; Wang, L.-W.; Liu, Z.; Butcher, D. R.; Salmeron, M.; Somorjai, G. A. *Nano Lett.* **2009**, *9*, 2167.
- [29] Gustafson, J.; Westerström, R.; Balmes, O.; Resta, A.; van Rijn, R.; Torrelles, X.; Herbschleb, C. T.; Frenken, J. W. M.; Lundgren, E. *J. Phys. Chem. C* **2010**, *114*, 4580.
- [30] Gao, F.; Cai, Y.; Gath, K. K.; Wang, Y.; Chen, M. S.; Guo, Q. L.; Goodman, G. W. *J. Phys. Chem. C* **2009**, *113*, 182.
- [31] Baraldi, A.; Lizzit, S.; Novello, A.; Comelli, G.; Rosei, R. *Phys. Rev. B* **2003**, *67*, 205404.
- [32] Koitaya, T.; Mukai, K.; Yoshimoto, S.; Yoshinobu, J. *J. Chem. Phys.* **2013**, *138*, 044702.
- [33] Ganduglia-Pirovano, M. V.; Scheffler, M.; Baraldi, A.; Lizzit, S.; Comelli, G.; Paolucci, G.; Rosei, R. *Phys. Rev. B* **2001**, *63*, 205415.
- [34] Toyoshima, A.; Kikuchi, T.; Tanaka, H.; Mase, K.; Amemiya, K.; Ozawa, K. *J. Phys. Conf. Ser.* **2013**, *425*, 152019.



### 3.3 CO and NO Adsorption on Low-Index Pd Surfaces

#### Abstract

CO and NO adsorption on low-index Pd single crystal surfaces under sub-Torr pressure conditions at room temperature was investigated by a combination of NAP-XPS and DFT based calculations. It is revealed that the surface coverage and adsorption structure was (reversibly) controlled by background pressure. Furthermore a pressure-induced additional site occupation of CO (NO) was found under higher pressure conditions. On Pd(100) surface, NO molecules partially dissociate into atomic species (N and O), but the N is chemically removed from the surface under the NAP conditions.

#### 3.3.1 Introduction

A carbon monoxide (CO) and nitric oxide (NO) can strongly interact with surface metal atoms with C and N end-down configurations. To understand the elemental step(s) of heterogeneous catalytic reaction, e.g. CO and NO conversion on TWC, the adsorption of CO or NO on single-crystal surfaces has been extensively investigated.<sup>1-44</sup> The adsorption structure may play significant roles to the catalytic reactivity. This information will help the development of commercial catalyst systems, for example exhaust gas convertors.

Pd is a one of the PGMs, and shows several excellent catalytic activities, for examples, conversion of organic molecules, and CO oxidation. Therefore adsorption structures on low-index Pd surfaces under ultra-high vacuum (UHV) conditions have been extensively investigated using surface sensitive structural<sup>1-3,5</sup> and spectroscopic<sup>1-4,6,7,13-15</sup> techniques.

On (100) and (110) orientated Pd surfaces, it is acknowledged that CO molecules stably adsorb on 2-fold bridge sites, while, the 3-fold hollow, 2-fold bridge and 1-fold top sites are occupied on (111) surface depending on surface temperature.

The NO/PGMs interaction also has been studied at various temperatures.<sup>13-28</sup> For example, NO molecules adsorb on the 4-fold hollow and the 2-fold bridge sites, at the coverage  $\theta$  of 0.25 and 0.50, respectively on Pd(100),<sup>13-15</sup> A part of NO molecule dissociates to atomic N and O even on the low index ordered PGM surfaces.<sup>15,19,24,25</sup>

However, because of technical constraints, the interactions between molecules and substrates, and morphology of surface adsorption structures under (near) atmospheric conditions are still less understood, even though actual heterogeneous catalysts usually work under atmospheric conditions.

In the present study, CO and NO adsorption on low-index Pd surfaces were investigated under the pressure range of up to 0.5 Torr, using a synchrotron-based NAP-XPS technique at room

temperature. DFT calculations were also employed to obtain information on adsorption states of CO and NO from the XP spectra. Background gas phase molecules stabilize the adsorbates under high pressure conditions. In some cases this effect results in formation of a new ordered surface structure, not observed at low temperature experiments under UHV. Numbers of high-pressure-induced surface species, which can accelerate the catalytic reaction, have been reported using various experimental techniques.<sup>46-52</sup>

### 3.3.2 Experimental and Computational Methodology

Single crystal surfaces were cleaned by a standard procedure: repeated cycles of the Ar<sup>+</sup> sputtering at room temperature, surface oxidation, followed by a brief annealing with an electron beam heating. Surface orientation and cleanness were checked by LEED and XPS. XPS measurements were performed at beamline 13A/B at KEK-PF. The base pressures of the analysis chamber and the separated preparation chamber were in the order of 10<sup>-10</sup> Torr. CO and NO gases (research grade) were introduced to the analysis chamber up to 0.5 Torr via variable metal leak valves. The purity of inlet gases were checked, because there is a possibility that the unwanted contaminants might affect the surface chemistry. For the CO gas, the Ni- (Fe-) carbonyl species are reported as the major contaminants in high pressure gas exposure. The Ni 2p (Fe 2p) XP spectrum taken under 500 mTorr ambient showed no carbonyl-associated feature. For the NO gas, the mass signals of O<sub>2</sub> (*m/e* = 32), N<sub>2</sub>O (44), and NO<sub>2</sub> (46) were under the detection limit. These results guaranteed the surface was free from contaminations. The sample temperature was controlled using the liquid N<sub>2</sub> cooling and resistive heating in the analysis chamber. The incident photon energies were tuned for each core-level to measure with almost the same surface sensitivity, for instance, the inelastic mean free path (IMFP) of Pd surface is estimated to be  $\approx 4.8$  Å by the TPP-2M method. The binding energy calibration was done based on the Fermi level. Because the photoemission intensity is attenuated by ambient-pressure gas, the C 1s, N 1s and O 1s intensities were normalized by the integrated intensity of metal substrate (i.e. Pd 3d<sub>5/2</sub>). The XP spectra were curve fitted using a convoluted function of Doniach–Šunjić and Gaussian, and Shirley-type background subtraction.

DFT calculations were performed using the VASP. The PAW method was used with a plane wave cutoff energy of 400 eV for electron–ion interactions. GGA-PBE was used for the exchange–correlation functional. The isolated molecules were calculated in the orthorhombic box. For bulk calculations, the estimated equilibrium lattice constant were  $a_0 = 3.90$  Å for Pd (fcc), which were slightly larger than the experimental value. The metal surfaces were constructed using the slab model with vacuum layer. Two-dimensional Brillouin zone integrations were performed by the Monkhorst–Pack method for each supercell to be uniformed *k*-point density. Adsorbed molecules were configured via C or N end-down structure. Adsorbates and metal layers are fully relaxed within the

residual force on atoms below  $0.05 \text{ eV \AA}^{-1}$ . BEs of core electrons and the resultant CLSs were estimated using the Slater–Janak transition approach.

### 3.4.3 Results and Discussions

#### CO and NO/Pd(100) system

First, results for the CO/Pd(100) system are discussed. Ball models of CO overlayer formed on Pd(100) are shown in Figure 3.3.1. Gray and dark gray balls show Pd atoms in the topmost surface and the subsurface layer, respectively. While the small ball shows the adsorbed CO molecule. The  $(2\sqrt{2} \times \sqrt{2})R45^\circ$  ( $\theta = 0.50$ ) structure is stably observed at room temperature, further dense structures are formed at lower temperatures. A DFT simulation predicts formation of the dense  $(1 \times 1)$  adsorption structure under high pressure conditions, although it has not been experimentally reported yet.<sup>11</sup>

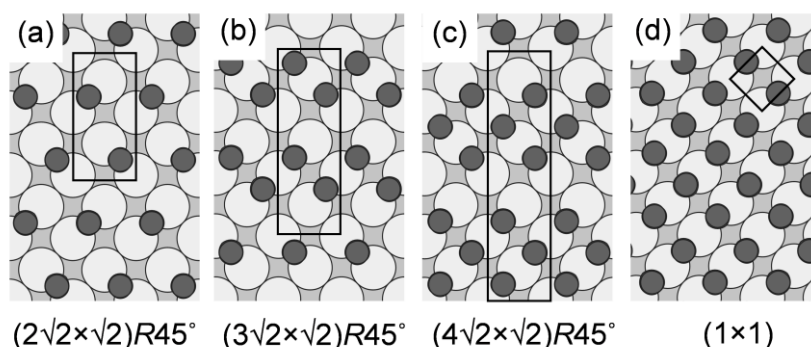


**Figure 3.3.1.** Top views of CO overlayer formed on Pd(100) surface are illustrated (a)  $(2\sqrt{2} \times \sqrt{2})R45^\circ$  ( $\theta = 0.50$ ), (b)  $(3\sqrt{2} \times \sqrt{2})R45^\circ$  ( $\theta = 0.67$ ), (c)  $(4\sqrt{2} \times \sqrt{2})R45^\circ$  ( $\theta = 0.75$ ), and (d)  $(1 \times 1)$ -CO ( $\theta = 1$ ). Large and small balls show the Pd atoms and CO molecules, respectively. The black squares show the unit cells of overlayers.

Figure 3.3.2 shows the pressure dependence of XP spectra of Pd  $3d_{5/2}$  (a), C 1s (b), here the surface temperature was at room temperature. The introduced CO gas pressure is labelled in the right side of each Pd  $3d_{5/2}$  spectrum (a). Labels in left side in the figures ( $\alpha$ ,  $\beta$ ,  $\gamma$  and  $\delta$ ) show the series obtained at same gas pressure. At lower pressure condition;  $10^{-7}$  Torr ( $\alpha$ ), Pd  $3d_{5/2}$  level is deconvoluted into two peak components at 334.9 eV denoted by bulk “B” and at 335.5 eV CO-bonding surface Pd “Pd<sub>1/2</sub>”. The CO gas exposure leads to appearance of the higher binding-energy component. The proportion of Pd<sub>1/2</sub> line is less asymmetric than that of B, suggesting that it is a CO-bonding surface component. A single peak is measured at C 1s level, because the CO molecules strongly adsorb on the bridge site. Further CO exposure up to  $10^{-3}$  Torr ( $\beta$ ) caused a new component at 335.9 eV “Pd<sub>1</sub>”. Whereas the Pd<sub>1/2</sub> intensity was decreased. Here the proportion and binding energy of the CO-bonding

surface components were fixed for all pressure conditions. While C 1s level taken at  $10^{-3}$  Torr hardly changed, the difference spectrum eliminates a small energy shift of  $\approx +0.1$  eV, suggesting the small change in chemical environment of CO on bridge site..

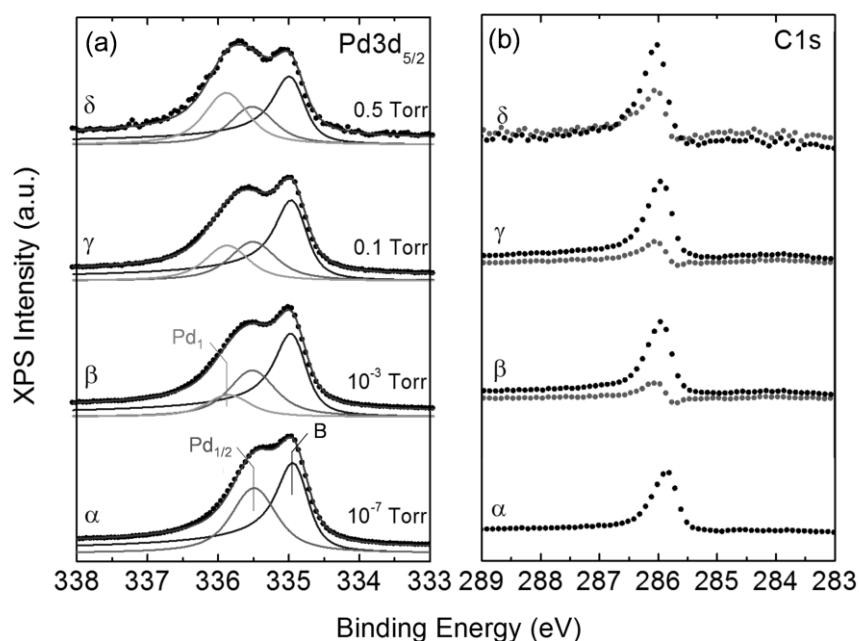


**Figure 3.3.2.** XP spectra of Pd(100) taken under different CO pressures up to 0.5 Torr for Pd3d<sub>5/2</sub> (a) and C1s (b) levels at room temperature. Labels  $\alpha$ ,  $\beta$ ,  $\gamma$  and  $\delta$  indicate the series of CO pressure. (a) Pd3d<sub>5/2</sub> levels are deconvoluted into three components “B” at 334.9 eV, “Pd<sub>1/2</sub>” at 335.5 eV and “Pd<sub>1</sub>” at 335.9 eV. (b) C1s exhibited a single peak at 285.9 eV, and difference spectra are overlapped at higher pressure conditions. Adapted from Ref. P-3. Copyright (2013), with permission from Elsevier.

Andersen et al. have reported that the exposure of CO to Pd(100) surface resulted in forming two distinct peaks, named type 1 (335.39–335.57 eV) and type 2 (335.89–336.01 eV) in addition to the bulk component in Pd 3d<sub>5/2</sub> XPS by using high resolution XPS under UHV.<sup>6</sup> These components are assigned to surface Pd bond(s) with one and two CO molecule(s), respectively. the peak intensity ratio of these peaks (Pd<sub>1</sub>/Pd<sub>1/2</sub>) are dependent on adsorption structures, the  $(2\sqrt{2} \times \sqrt{2})R45^\circ$  ( $\theta = 0.50$ ),  $(3\sqrt{2} \times \sqrt{2})R45^\circ$  ( $\theta = 0.67$ ) and  $(4\sqrt{2} \times \sqrt{2})R45^\circ$  ( $\theta = 0.75$ ). Surface structures at 10<sup>-7</sup> Torr and 10<sup>-3</sup> Torr are assumed as the  $(2\sqrt{2} \times \sqrt{2})R45^\circ$  and  $(3\sqrt{2} \times \sqrt{2})R45^\circ$ , respectively, based on the number of surface Pd atoms attributed to Pd<sub>1/2</sub> and Pd<sub>1</sub> per unit cell. Here it is assumed that the spectra which obtained at 10<sup>-7</sup> Torr as the coverage of 0.5 monolayer (ML), where it is defined as a number of CO molecule per surface Pd atom. The coverage at 10<sup>-3</sup> Torr is estimated to be  $0.61 \pm 0.01$  ML from C 1s and  $0.66 \pm 0.06$  ML from the ratio in Pd3d<sub>5/2</sub> (Pd<sub>1</sub>/Pd<sub>1/2</sub> = 0.47). These are close to the ideal coverage

of 0.67 ML for the  $(3\sqrt{2} \times \sqrt{2})R45^\circ$  structure.

With using IRAS technique, Bradshaw and Hoffmann proposed occupation of top sites on the Pd(100) surface under  $1 \times 10^{-7}$  Torr CO at 300 K<sup>1</sup>. Their experimental condition was close to that for Figure 3.3.2 in the present experiment. It was reported that the CO on top site gives an obviously higher binding-energy (+0.7 eV) with respect to the CO on bridge site on Pd(111) under 0.1 mbar CO.<sup>42</sup> Since such a higher binding-energy component was not observed in  $\alpha$ , it is assumed that the amount of top CO was below the detection limit at  $10^{-7}$  Torr if it is coexist on the surface. Goodman et al. reported that the CO molecules adsorb on only bridge site on Pd(100) surface at 1 Torr CO presence by using the PM-IRAS techniques.<sup>37</sup> It is assumed that the CO on Pd(100) surface adsorbs on bridge site regardless the background CO pressure. A DFT study predicted that the bridge site is favored in the energetic point of view.<sup>10</sup>

DFT calculations were employed to support peak assignments in XPS. To consider the binding-energy shift of the surface Pd layer, the 2nd and 3rd layer Pd are fixed in crystal lattice. CO molecules are located on bridge site with the perpendicular configuration to the surface via the C atom. Here we modelled the  $(2\sqrt{2} \times \sqrt{2})R45^\circ$  and the  $(4\sqrt{2} \times \sqrt{2})R45^\circ$  adsorption structures. The CO molecules in the  $(2\sqrt{2} \times \sqrt{2})R45^\circ$  structure has kept the upright configuration from surface normal, whereas a part of CO molecules in the  $(4\sqrt{2} \times \sqrt{2})R45^\circ$  structure was slightly tilted ( $< 10^\circ$ ), because of the local uplift of surface Pd atoms.

The Pd<sub>1</sub> intensity was grown further during CO gas introduction. At 0.1 Torr ( $\gamma$ ), the intensity ratio Pd<sub>1</sub>/Pd<sub>1/2</sub> was almost unity (0.9), suggesting that the  $(4\sqrt{2} \times \sqrt{2})R45^\circ$  overlayer was formed. This overlayer has already been identified at low temperatures under UHV. The surface coverages at 0.1 Torr estimated from C 1s and Pd 3d<sub>5/2</sub> are  $0.63 \pm 0.01$  and  $0.74 \pm 0.07$  ML, respectively. Although the surface forms a higher-density phase, the C 1s peak exhibited the CO bonding on bridge site with a slight growth compared with that for  $10^{-3}$  Torr ( $\beta$ ). The less responsibility to the pressure might be explained by a photoelectron diffraction effect due to the change of local adsorption configuration of CO molecules in the  $(4\sqrt{2} \times \sqrt{2})R45^\circ$  structure.

The ratio Pd<sub>1</sub>/Pd<sub>1/2</sub> increased over the unity ( $>1$ ) at 0.5 Torr ( $\delta$ ). The presence of such a high-density phase is not previously supported in experiments. At this moment, a distinct growth of CO intensity appeared, whereas contaminants, e.g. atomic C and carbonyl species, which comes from chamber wall and/or residual gas was not observed in C 1s level. No change of the binding energy was observed in the difference spectrum with respect to other difference spectra. The surface coverage at 0.5 Torr estimated from C 1s and Pd 3d levels are  $0.83 \pm 0.06$  and  $0.78 \pm 0.07$  ML, respectively. The experimental error of Pd<sub>1</sub>/Pd<sub>1/2</sub> is estimated to  $\pm 10\%$ . As discussed above, the C 1s spectra was normalized by the corresponding peak area of from the Pd substrate. As a result, it is confirmed that the CO intensity increased obviously in C 1s level. Therefore it is concluded that the increase of Pd<sub>1</sub>/Pd<sub>1/2</sub> at 0.5 Torr stems from an additional adsorption of CO on the surface.

Figure 3.3.3 shows reversibility of Pd<sub>1</sub>/Pd<sub>1/2</sub> intensity as a function of dosing CO pressure. The intensity ratio depends on CO pressure and changes almost reversibly: the ratio estimates to be 0 at 10<sup>-7</sup> Torr, indicating the (2√2 × √2)R45° structure (1). The ratio becomes 0.9 at 10<sup>-1</sup> Torr (2), and the continuous dosing up to 0.5 Torr causes an increase of the ratio to 1.3 (3). The ratio went back to 0.9, when the CO pressure is set to 10<sup>-1</sup> Torr (4). Further cycles exhibited the same trend: second (4-6) and third (6-8) cycles. These results well indicate that the (4√2 × √2)R45°-like phase and the further dense (1 × 1)-like phase reversibly formed under the equilibrium with background pressure. Figure 3.3.3 (b and c) show Pd 3d<sub>5/2</sub> and C 1s spectra taken at 10<sup>-7</sup> Torr (bottom) and after pumping out of 0.5 Torr CO (top).

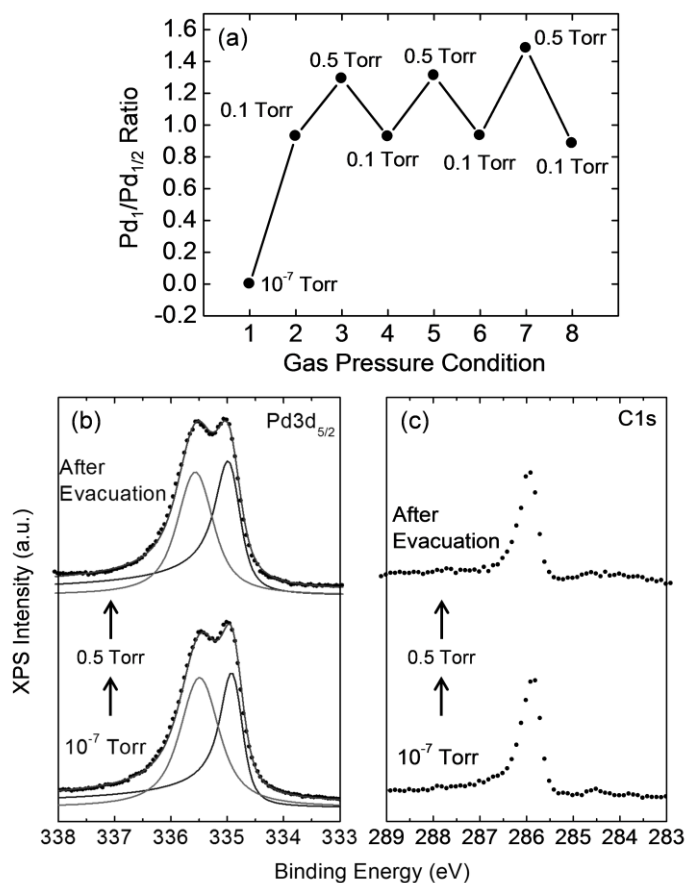


**Figure 3.3.3.** (a) Pd<sub>1</sub>/Pd<sub>1/2</sub> ratio at each CO gas pressure. The Pd 3d<sub>5/2</sub> (b) and C 1s (c) spectra taken under 10<sup>-7</sup> Torr CO ambient (bottom) is intrinsically unchanged from the spectrum taken after gas evacuation (top). Adapted from Ref. P-3. Copyright (2013), with permission from Elsevier.

Both XP spectra shows two peak components (b), denoted by B and Pd<sub>1/2</sub>, the spectral shape is intrinsically unchanged, suggesting the reversible formation of (2√2 × √2)R45°. The complete

disappearance of Pd<sub>1</sub> after gas exposure suggests that the CO molecules on the surface are stabilized by the background CO. The CO dissociation is ruled out by the XP spectrum of C 1s level (c), because of the absence attributed to the atomic C at 284 eV. Recently Somorjai and co-workers revealed that the CO dissociates even on ordered Pt surfaces under high-pressure CO treatment.<sup>40,41</sup> However, it is confirmed that the CO dissociation does not occur on Pd(100) surface in the present case.

Rogal et al. have predicted that the dense (1 × 1)-CO overlayer ( $\theta = 1$ ) (Figure 3.3.1 right panel), is stabilized under presence of CO by using DFT calculations.<sup>11</sup> If the adsorbed CO molecules dominate 50% of accessible bridge sites, the (1 × 1)-CO overlayer should be formed, here the surface reconstruction is excluded. If the (1 × 1)-CO overlayer is perfectly formed on the surface the Pd<sub>1/2</sub> component should disappear. Therefore the overlayer at 0.5 Torr is under the transition from (4√2 × √2)R45° to the (1 × 1)-CO.

Next, NO adsorption on Pd(100) surface is discussed. Jaworowski et al. found that the NO molecules exposed to the Pd(100) surface adsorbs on 2-fold bridge to 4-fold hollow sites depending on substrate temperature and surface coverage with using low temperature LEED and XPS experiments.<sup>15</sup> Below 250 K, NO molecules dominate the bridge sites with forming a (2√2 × √2)R45° overlayer ( $\theta = 0.50$ ). A site change from bridge to hollow site is observed at above 420 K, where the p(2 × 2) and c(4 × 2) overlayers ( $\theta = 0.25$ ) coexist on the surface. Schematic adsorption structure models for the p(2 × 2), c(4 × 2) and (2√2 × √2)R45° structures are shown in Figure 3.3.4.

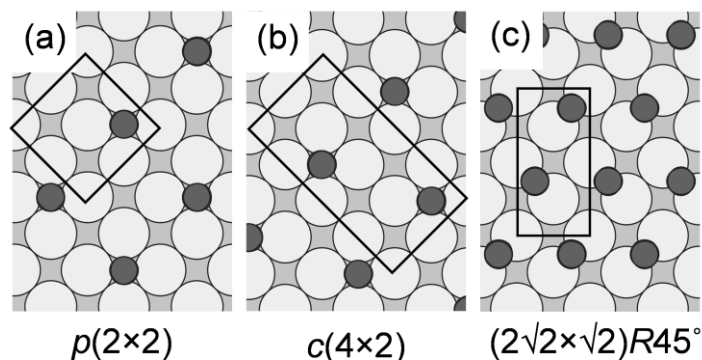


**Figure 3.3.4.** Top views of NO overlayer formed on Pd(100) surface, (a and b) p(2 × 2) and c(4 × 2) ( $\theta = 0.25$ ), and (c) (2√2 × √2)R45° ( $\theta = 0.50$ ). Large and small balls show the Pd atoms and CO molecules, respectively. The black squares show the unit cells of the overlayers. Adapted from Ref. P-3. Copyright (2013), with permission from Elsevier.

Figure 3.3.5 shows the pressure dependence of NAP-XP spectra of Pd 3d<sub>5/2</sub> (a), N 1s and its difference spectra (b) recorded at room temperature. Labels ( $\alpha$ ,  $\beta$ ,  $\gamma$  and  $\delta$ ) are marked in the left side in the figures. Under 10<sup>-7</sup> Torr NO pressure ( $\alpha$ ), two distinct components are seen in Pd 3d<sub>5/2</sub> level (a).

The lower one is attributed to bulk “B” (334.9 eV), and the other one labeled by “Pd<sub>1/2</sub>” (335.7 eV) is an NO-bonding surface component. In N 1s level (b), a broad and asymmetric peak centered at 400.6 eV is detected; that is sign of NO adsorption on the surface. The tailing to the higher binding-energy side is a general trend of other NO/metal systems.<sup>15, 21</sup> The experimental CLS of the surface Pd atoms binding to the hollow-NO was estimated to +0.3 eV from the bulk ones.<sup>15</sup> Any component was not observed at +0.3 eV, in the present case at 10<sup>-7</sup> Torr, which indicated that the p(2 × 2) and c(4 × 2) overlayers are not formed in the present experimental conditions. In the present measurement under 10<sup>-7</sup> Torr, the CLS of Pd<sub>1/2</sub> is +0.8 eV with respect to B, that is in good agreement with that of the bridge-occupied Pd and much higher than that of the hollow-occupied Pd.

Thus the Pd<sub>1/2</sub> component is ascribed to the bridge-site Pd. The bridge-site Pd is dominantly detected in α, the NO induced overlayer is assigned as the (2√2 × √2)R45°. The present spectral shape is somewhat different from the previous results,<sup>15</sup> that may be explained by differences in incident photon energy selected in the present study.

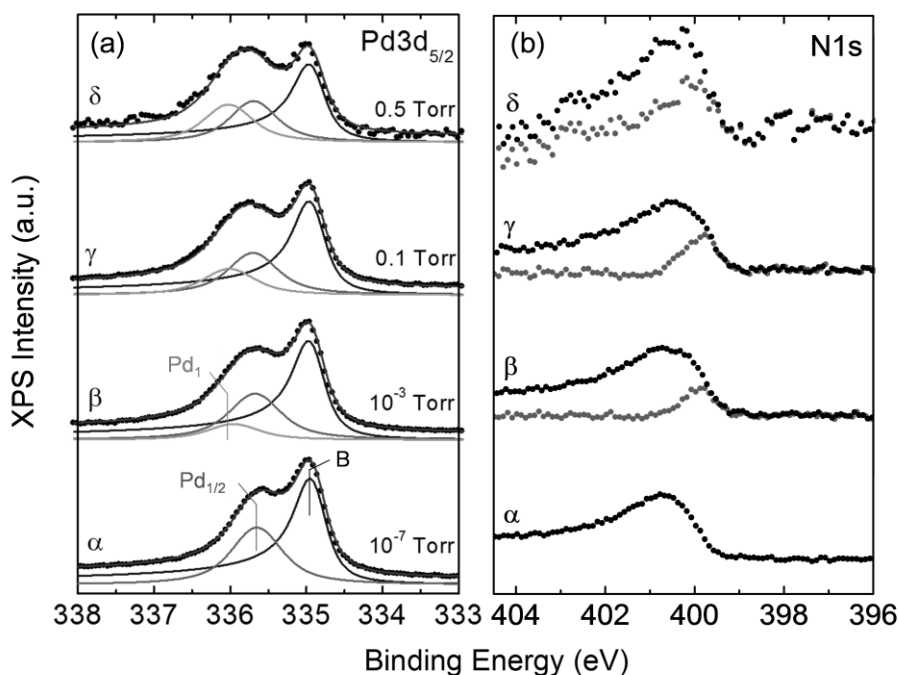


**Figure 3.3.5.** XP spectra of Pd(100) taken under different NO pressures up to 0.5 Torr for Pd3d<sub>5/2</sub> (a) and C1s (b) levels at room temperature. Labels α, β, γ and δ indicate the series of NO pressure. (a) Pd3d<sub>5/2</sub> levels are deconvoluted into three components “B” at 334.9 eV, “Pd<sub>1/2</sub>” at 335.7 eV and “Pd<sub>1</sub>” at 336.0 eV. (b) N1s exhibited a broad peak centered at 400.6 eV, and difference spectra are overlapped at higher pressure conditions. Adapted from Ref. P-3. Copyright (2013), with permission from Elsevier.

Increasing the pressure up to  $10^{-3}$  Torr ( $\beta$ ) leads to appearance of a new component denoted by “Pd<sub>1</sub>” (336.0 eV). The N 1s level does not significantly change, however the difference spectrum highlights the presence of additional component at 400.0 eV. A previous DFT simulation suggested that NO adsorption on top site results in the shift toward to the lower binding energy side on NO/Pt(111) system.<sup>27</sup> This result implies that the adsorption on top site is stabilized on Pd(100) surface. Further NO exposure lead the increase of intensity of Pd<sub>1</sub> component. At 0.5 Torr NO pressure ( $\delta$ ), the intensity is almost the same with Pd<sub>1/2</sub> in Pd 3d<sub>5/2</sub>. If it is assumed that the coverage of the NO structure formed at  $10^{-7}$  Torr as 0.5 ML ( $(2\sqrt{2} \times \sqrt{2})R45^\circ$ ), the coverage at 0.5 Torr estimated from N 1s level is to be  $0.70 \pm 0.03$  ML. The Pd<sub>1</sub> component is substantially weakened after NO gas evacuation. It indicates that the NO on top site is a metastable species and is stabilized by the background NO.

To confirm peak assignments, the CLSs were simulated for the NO adsorption on Pd(100) surface with considering possible NO overlayers. Because the configuration of NO on top site on Pd(100) was not clear, so the stable adsorption geometry of NO on top site is determined. There is a possibility that the NO molecule located on top site has a tilting configuration from the surface normal. It is reported that the NO on top site on Pd(111)<sup>17,18</sup> and Pt(111)<sup>27,28</sup> has a tilting configuration. While perpendicular configuration is stable on Ir(111)<sup>25</sup> and Rh(111)<sup>31</sup> surfaces. Adsorption geometry of NO on Pd(100) was considered by optimizing both of the upright and the tilting configurations and it was found that the tilting configuration was more reasonable from the energetic point of view.

The atomic species, e.g., N and O, are created via the NO dissociation without thermal excitation (room temperature) even on low-index single crystal surfaces.<sup>16,19,24,25</sup> Thus the possibility of the NO dissociation under high pressure conditions should be taken into account. Under the equilibrium conditions, the spectral evidence for dissociation was not clearly observed.<sup>15,52</sup> Nevertheless after the gas evacuation, the atomic species was detected at 397.5 eV which was assigned to the adsorbed N. The corresponding Pd 3d<sub>5/2</sub> level exhibits a new component at 335.4 eV, assigned to N-binding surface Pd atom. In a previous report<sup>15</sup>, the dissociation of adsorbed NO on Pd(100) surface occurred at above 550 K, although the active center was surface defect. It is not concluded whether the dissociation proceeds on regular or irregular sites like a defect. The atomic species was not observed under the gas equilibrium conditions, but detected after pumping out NO gas. It may be explained by the chemical removal of atomic species, (i.e. associative desorption  $2O_{ad} \rightarrow O_2\uparrow$  and  $2N_{ad} \rightarrow N_2\uparrow$  and/or  $NO + O$  and  $NO + N$  reactions) continuously proceeds on the surface.

Next, it is considered the formation of NO<sub>x</sub> compound on the surface resulted from the oxidation of NO. It is reported that the nitrite (NO<sub>2</sub>) and/or nitrate (NO<sub>3</sub>) formation on NO/Pd particles. They exhibit a higher binding-energy components in Pd 3d<sub>5/2</sub> (338.2-338.9 eV) and N 1s (nitrite; 403.8-404.7 eV and nitrate; 406.8-407.7 eV) levels. Such higher binding-energy shifts in both of Pd 3d<sub>5/2</sub> and N 1s levels are not observed during/after gas introduction. Therefore the formation of these oxidized species is excluded on the Pd(100) surface.

Finally, Table 3.3.1 shows the comparison of theoretical and experimental CLSs and corresponding assignments, where the values are estimated with respect to the bulk in Pd 3d<sub>5/2</sub> level. The theoretical CLSs of Pd bonding with one bridge-CO (+0.67 eV) and Pd with two bridge-COs (+1.23 eV) are consistent with experimental observations; Pd<sub>1/2</sub> (+0.6 eV) and Pd<sub>1</sub> (+1.0 eV). It was also estimated that the C 1s CLSs of bridge-CO exhibited the no large shift (< 0.02 eV) for different adsorption overlayers. This is also in good agreement with the experimental observations. As a summary, it is confirmed that CO molecules are adsorbed on the bridge sites of the Pd(100) surface irrespective of the long-range structure. In the case of NO/Pd(100) system, the top site occupation under high-pressure NO is also supported by the present simulations.

**Table 3.3.1.** Comparison between calculated and experimental CLSs. For CO (NO) adsorbed Pd(100) surfaces, molecules are assumed to locate at bridge and top sites. The CO- (NO-) binding Pd atoms are labelled as Pd<sub>x</sub>, where *x* is the coordination number of CO (NO) to the Pd atom. Adapted from Ref. P-3. Copyright (2013), with permission from Elsevier.

system	level	label	calcd CLS (eV)	exp. CLS (eV)
CO/Pd(111)	Pd 3d	Pd <sub>1/2</sub>	+0.67	+0.6
		Pd <sub>1</sub>	+1.23	+1.0
NO/Pd(111)	Pd 3d	Pd <sub>1/2</sub>	+0.90	+0.8
		Pd <sub>1</sub>	+1.30	+1.1

### CO/Pd(111) system

The CO adsorption on Pd(111) surfaces is one of typical adsorption model systems to understand adsorbate-substrate interactions. Therefore it has been extensively investigated over a wide ranges of pressure and temperature using various surface science techniques. Figure 3.4.6 shows the CO adsorption behavior under different pressure conditions at 298 K. The clean (CO-free) surface exhibits two components in Pd 3d<sub>5/2</sub> level (a), which reflect surface (S) and bulk (B) Pd atoms. CO exposure causes a shift of the surface component to the higher-energy side (c). Curve fitting analyses lead us to conclude that CO molecules are adsorbed at bridge (Pd<sub>1/2</sub>) and hollow (Pd<sub>1/3</sub>) sites, which is consistent with C 1s level (d). Here the CO coverage is estimated to be 0.50 ML.<sup>53</sup>

Under 10 mTorr CO, another component appears at the higher-energy side, which is associated with on top CO (e and f) and labeled as Pd<sub>1</sub> and t. This is in good agreement with a previous result performed under a similar pressure condition.<sup>54</sup> These peak assignments are supported by core-level-shift calculations (Table 3.3.2).

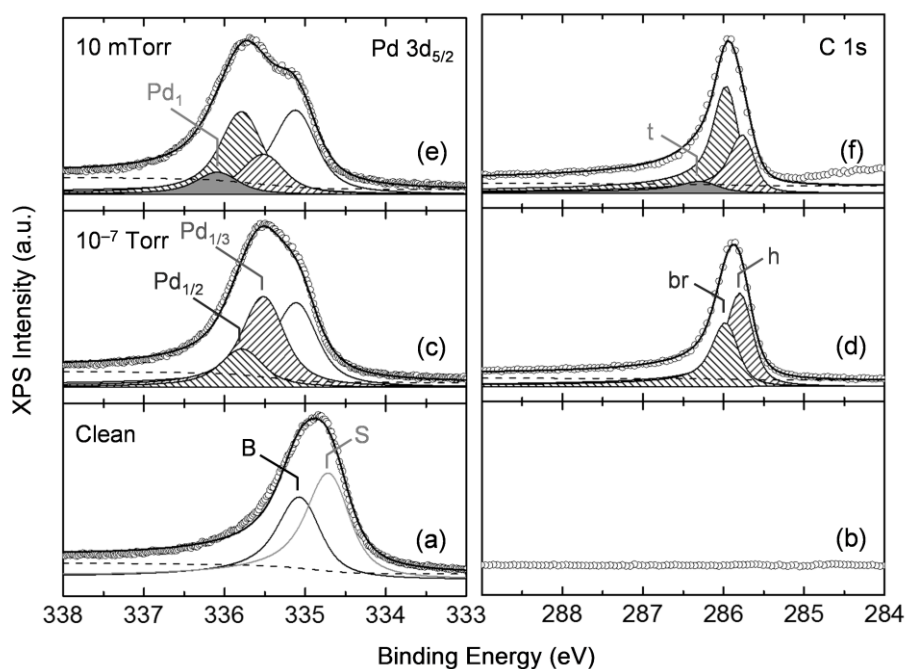


**Figure 3.4.6.** XP spectra for Pd  $3d_{5/2}$  and C 1s levels taken from Pd(111) surface under different pressure condition at 298 K. All XP spectra are shown with curve fitting results, where each component is labelled by B, S and  $Pd_x$  in Pd  $3d_{5/2}$  and h, br and t in C 1s. Adapted with permission from Ref. P-7. Copyright (2015) American Chemical Society.

**Table 3.3.2.** Comparison between calculated and experimental CLSs for Pd(111) and CO/Pd(111). For the clean surfaces, the CLSs of the 1st layer (S) atom is calculated. For CO adsorbed surfaces, CO molecules are assumed to locate at hollow (h), bridge (br) and top (t) sites. The CO-binding Pd atoms are labelled as  $Pd_x$ , where  $x$  is the coordination number of CO to the Pd atom. The reference species of Pd 3d and C 1s XPS are the bulk Pd and CO adsorbed at the hollow site, respectively. Adapted with permission from Ref. P-7. Copyright (2015) American Chemical Society.

system	level	label	calcd CLS (eV)	exp. CLS (eV)
Pd(111)	Pd 3d	S	-0.26	-0.28
CO/Pd(111)	Pd 3d	$Pd_{1/3}$	+0.47	+0.40
		$Pd_{1/2}$	+0.75	+0.66
		$Pd_1$	+1.35	+0.98
	C 1s	br	+0.22	+0.20
		t	+0.79	+0.50

A hump structure at around 284 eV is due to a carbon contamination. The intensity of Pd<sub>1/3</sub> observed at 10 mTorr decreases from that at 10<sup>-7</sup> Torr, whereas the intensity of Pd<sub>1/2</sub> shows reverse trend. And the Pd<sub>1</sub> is observed at 10 mTorr only. The fraction of occupation of the adsorption sites depends on the pressure. It suggests that the Pd(111) surface forms the densely-packed phase by occupation of lower-coordination sites with increasing CO pressure.

### CO/Pd(110) system

Finally, the result of CO/Pd(110) system is presented under the pressure range from UHV to near-ambient-pressure. Figure 3.3.7 shows the Pd 3d<sub>5/2</sub> and C 1s XP spectra taken for different CO pressures up to 0.1 Torr. First, at lower pressure 10<sup>-7</sup> Torr, the spectrum was deconvoluted into three components in Pd 3d<sub>5/2</sub>, denoted as B, 335.0 eV; Pd<sub>1/2</sub>, 335.6 eV and Pd<sub>1</sub>, 336.0 eV. The CO on surface exhibits a single peak at 286.0 eV in C 1s level, besides a peak appears at 531.8 eV in O 1s level. The experimental value of obtained CLS for Pd<sub>1/2</sub> (+ 0.6 eV) based on the binding energy of B is near to the previously reported value for the (4 × 2)-6CO overlayer ( $\theta = 0.75$ ) as illustrated in (c), where CO molecules locate on bridge sites of the reconstructed (1 × 2) missing-row surface.<sup>40</sup> Whereas, the value for Pd<sub>1</sub> (+ 1.0 eV) implies the formation of the dense (2 × 1)p2mg-2CO overlayer ( $\theta = 1$ ) as illustrated in (d). The CO molecules locate on the bridge site on atomic rows of the non-reconstructed (1 × 1) surface in the (2 × 1)p2mg-2CO overlayer.<sup>55,56</sup>

The Pd 3d<sub>5/2</sub> and C 1s spectra do not exhibit the drastic change over the pressure range from 10<sup>-7</sup> to 0.1 Torr (a and b). The slight increase of Pd<sub>1</sub> component is observed at higher pressures. A small hump at 284 eV, which is attributed to atomic C, appears above 10<sup>-3</sup> Torr in C 1s level. It originates from the hydrocarbons from gas-phase residual and/or chamber wall. It also give a contribution in the Pd 3d<sub>5/2</sub> level via Pd-C bonds. Since the value of CLS for the C-binding Pd atom is about +0.5~+0.6 eV in Pd 3d<sub>5/2</sub> level, thus the Pd<sub>1/2</sub> component includes a contribution from the C-bonding Pd at above 10<sup>-3</sup> Torr.<sup>18</sup> The intensity ratio is estimated as follows; CO : C = 1 : 0.17. These results indicate that the CO molecules dominate the Pd(110) surface. Since the (2 × 1)p2mg-2CO overlayer has the highest density ( $\theta = 1$ ) and is formed even at 10<sup>-7</sup> Torr, further dense overlayer is not formed at higher pressures.

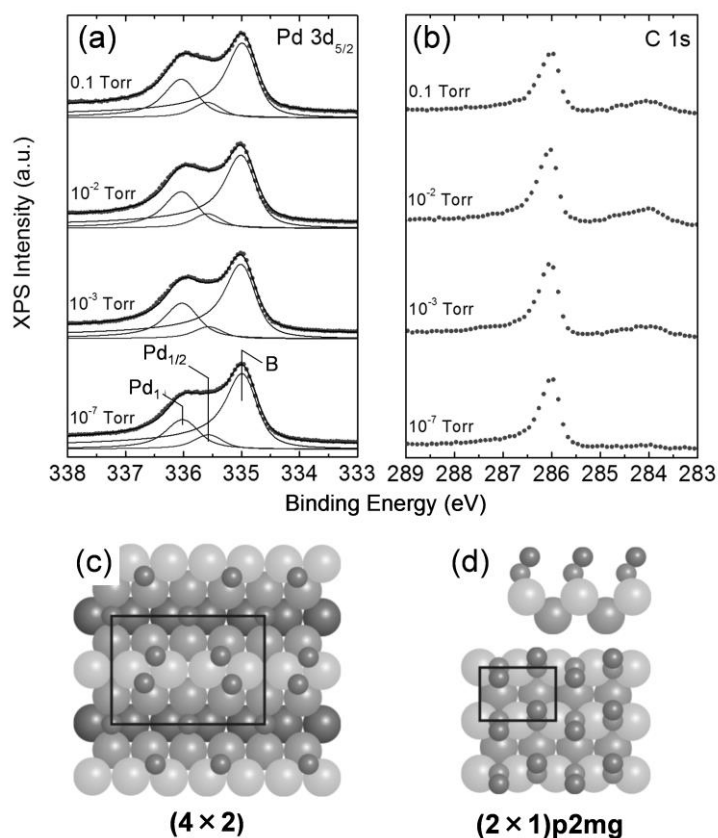


**Figure 3.3.7** XP spectra of Pd  $3d_{5/2}$  (a) and C  $1s$  (b) levels taken from a Pd(110) surface at different CO pressures at room temperature. At  $10^{-7}$  Torr, the Pd  $3d_{5/2}$  XP spectra are curve fitted into three components; B (335.0 eV) and two CO-bonding surface Pds; Pd $_{1/2}$  (335.6 eV) and Pd $_1$  (336.0 eV). Adsorbed CO gives a peak around 286 eV in C  $1s$ . A small hump at around 284 eV is atomic C species. Schematic model structures are illustrated; the  $(4 \times 2)$ -6CO (d) and the  $(2 \times 1)p2mg$ -2CO (e). Adapted with permission from Ref. P-4. Copyright (2013) American Chemical Society.

### 3.3.4 Conclusions

CO and NO adsorption on low-index Pd surfaces under sub-Torr gas pressure conditions were investigated using experimental and theoretical approaches. It is concluded that the dense molecular overlayer is reversibly formed on the surface without a surface reconstruction nor site switching from the 2-fold bridge at up to 0.5 Torr CO for the CO/Pd(100) and Pd(110) systems. Whereas the top site occupation was observed on Pd(111) surface, which was stabilized by background CO. A site switching from bridge to top site takes place at higher pressures for the NO/Pd(100) system. These data were well supported by theoretical simulations. These fundamental findings will improve the further understanding of heterogeneous catalytic reactions proceeding on Pd surfaces.



## References

- [1] Bradshaw, A. M.; Hoffmann, F. M. *Surf. Sci.* **1978**, *72*, 513.
- [2] Behm, R. J.; Christmann, K.; Ertl, G.; Van Hove, M. A.; Thiel, P. A.; Weinberg, W. H. *Surf. Sci.* **1979**, *88*, L59.
- [3] Behm, R. J.; Christmann, K.; Ertl, G.; Van Hove, M. A. *J. Chem. Phys.* **1980**, *73*, 2984.
- [4] Ortega, A.; Hoffman, F. M.; Bradshaw, A. M. *Surf. Sci.* **1982**, *119*, 79.
- [5] Berndt, W.; Bradshaw, A. M. *Surf. Sci. Lett.* **1992**, *279*, L165.
- [6] Andersen, J. N.; Qvarford, M.; Nyholm, R.; Sorensen, S. L.; Wigren, C. *Phys. Rev. Lett.* **1991**, *67*, 2822.
- [7] Surnev, S.; Sock, M.; Ramsey, M. G.; Netzer, F. P.; Wiklund, M.; Borg, M.; Andersen, J. N. *Surf. Sci.* **2000**, *470*, 171.
- [8] Gierer, M.; Barbieri, A.; Van Hove, M. A.; Somorjai, G. A. *Surf. Sci.* **1997**, *391*, 176.
- [9] Smeth, M.; Beutler, A.; Ramsvik, T.; Nyholm, R.; Borg, M.; Andersen, J. N.; Duschek, R.; Sock, M.; Netzer, F. P.; Ramsey, M. G. *Surf. Sci.* **2001**, *491*, 99.
- [10] Eichler, A.; Hafner, J. *Phys. Rev. B* **1998**, *57*, 10110.
- [11] Rogal, J.; Reuter, K.; Scheffler, M. *Phys. Rev. Lett.* **2007**, *98*, 046101.
- [12] Wang, J. G.; Li, W.-X.; Borg, M.; Gustafson, J.; Mikkelsen, A.; Pedersen, T. M.; Lundgren, E.; Weissenrieder, J.; Klikovits, J.; Schmid, M.; Hammer, B.; Andersen, J. N. *Phys. Rev. Lett.* **2005**, *95*, 25612.
- [13] Nyberg, C.; Uvdal, P. *Surf. Sci.* **1988**, *204*, 517.
- [14] Sugai, S.; Watanabe, H.; Kioka, T.; Miki, H.; Kawasaki, K. *Surf. Sci.* **1991**, *259*, 109.
- [15] Jaworowski, A. J.; Ásmundsson, R.; Uvdal, P.; Sandell, A. *Surf. Sci.* **2002**, *501*, 74.
- [16] Sharpe, R. G.; Bowker, M. *Surf. Sci.* **1996**, *360*, 21.
- [17] Hansen, K. H.; Šljivančanin, Ž.; Hammer, B.; Lægsgaard, E.; Besenbacher, F.; Stensgaard, I. *Surf. Sci.* **2002**, *496*, 1.
- [18] Kostelník, P.; Šikola, T.; Varga, P.; Schmid, M.; *J. Phys. Condens. Matter.* **2009**, *21*, 134005.
- [19] Rienks, E. D. L.; Bakker, J. W.; Baraldi, A.; Carabineiro, S. A. C.; Lizzit, S.; Weststrate, C. J.; Nieuwenhuys, B. E. *Surf. Sci.* **2002**, *516*, 109.
- [20] Shimada, T.; Kondoh, H.; Iwasaki, M.; Nakai, I.; Nagasaka, M.; Amemiya, K.; Orita, H.; Ohta, T. *J. Phys. Chem. B* **2006**, *110*, 20507.
- [21] Zhu, J. F.; Kinne, M.; Fuhrmann, T.; Denecke, R.; Steinrück, H.-P. *Surf. Sci.* **2003**, *529*, 384.
- [22] Matsumoto, M.; Fukutani, K.; Okano, T.; Miyake, K.; Shigekawa, H.; Kato, H.; Okuyama, H.; Kawai, M. *Surf. Sci.* **2000**, *454*, 101.
- [23] Zhu, J. F.; Kinne, M.; Fuhrmann, T.; Denecke, R.; Steinrück, H.-P. *Surf. Sci.* **2003**, *529*, 384.
- [24] So, S. K.; Franchy, R.; Ho, W. *J. Chem. Phys.* **1989**, *91*, 5701.
- [25] Matsumoto, M.; Fukutani, K.; Okano, T. *Surf. Sci.* **2012**, *606*, 1489.
- [26] Fujitani, T.; Nakamura, I.; Takahashi, A.; Haneda, M.; Hamada, H. *J. Catal.* **2008**, *253*, 139.
- [27] Zeng, Z.-H.; Da Silva, J. L. F.; Deng, H.-Q.; Li, W.-X. *Phys. Rev. B* **2009**, *79*, 205413.
- [28] Aizawa, H.; Morikawa, Y.; Tsuneyuki, S.; Fukutani, K.; Ohno, T. *Surf. Sci.* **2002**, *514*, 394.
- [29] Certona, P.; Rider, K.; Yoon, H. A.; Salmeron, M.; Somorjai, G. A. *Surf. Sci.* **2000**, *445*, 249.
- [30] Rider, K. B.; Hwang, K. S.; Salmeron, M.; Somorjai, G. A. *Phys. Rev. Lett.* **2001**, *86*, 4330.
- [31] Popa, C.; Flipse, C. F. J.; Jansen, A. P. J.; van Santen, R. A.; Sautet, P. *Phys. Rev. B* **2006**, *73*, 245408.
- [32] Jensen, J. A.; Rider, K. B.; Salmeron, M.; Somorjai, G. A. *Phys. Rev. Lett.* **1998**, *80*, 1228.
- [33] Vang, R. T.; Wang, J.-G.; Knudsen, J.; Schnadt, J.; Lægsgaard, E.; Stensgaard, I.; Besenbacher, F. *J. Phys. Chem. B* **2005**, *109*, 14262.
- [34] Ozensoy, E.; Min, B. K.; Santra, A. K.; Goodman, D. W. *J. Phys. Chem. B* **2004**, *108*, 4351.
- [35] Ozensoy, E.; Hess, C.; Loffreda, D.; Sautet, P.; Goodman, D. W. *J. Phys. Chem. B* **2005**, *109*, 5414.
- [36] Hess, C.; Ozensoy, E.; Yi, C.-W.; Goodman, D. W. *J. Am. Chem. Soc.* **2006**, *128*, 2988.
- [37] Szanyi, J.; Kuhn, W. K.; Goodman, D. W. *J. Vac. Sci. Technol. A* **1993**, *11*, 1969.
- [38] Yoshioka, K.; Kitamura, F.; Takeda, M.; Takahashi, M.; Ito, M. *Surf. Sci.* **1990**, *227*, 90.
- [39] Dellwig, T.; Rupprechter, G.; Unterhalt, H.; Freund, H.-J. *Phys. Rev. Lett.* **2000**, *85*, 776.

- [40] Kung, K. Y.; Chen, P.; Wei, F.; Shen, Y. R.; Somorjai, G. A. *Surf. Sci.* **2000**, *463*, L627.
- [41] McCrea, K.; Parker, J. S.; Chen, P.; Somorjai, G. A. *Surf. Sci.* **2001**, *494*, 238.
- [42] Kaichev, V. V.; Prosvirin, I. P.; Bukhtiyarov, V. I.; Rupprechter, H. U. G.; Freund, H.-J. *J. Phys. Chem. B* **2003**, *107*, 3522.
- [43] Balmes, O.; Resta, A.; Wermeille, D.; Felici, R.; Messing, M. E.; Deppert, K.; Liu, Z.; Grass, M. E.; Bluhm, H.; van Rijn, R.; Frenken, J. W. M.; Westerström, R.; Blomberg, S.; Gustafson, J.; Andersen, J. N.; Lundgren, E. *Phys. Chem. Chem. Phys.* **2012**, *14*, 4796.
- [44] Shimada, T.; Mun, B. S.; Nakai, I. F.; Banno, A.; Abe, H.; Iwasawa, Y.; Ohta, T.; Kondoh, H. *J. Phys. Chem. C* **2010**, *114*, 17030.
- [45] Bukhtiyarov, A. V.; Kvon, R. I.; Nartova, A. V.; Prosvirin, I. P.; Bukhtiyarov, V. I. *Surf. Sci.* **2012**, *606*, 559.
- [46] Ackerman, M. D.; Pedersen, T. M.; Hendriksen, B. L. M.; Robach, O.; Bobaru, S. C.; Popa, I.; Quiros, C.; Kim, H.; Hammer, B.; Ferrer, S.; Frenken, J. W. M. *Phys. Rev. Lett.* **2005**, *95*, 255505.
- [47] Gustafson, J.; Westerström, R.; Mikkelsen, A.; Torrelles, X.; Balmes, O.; Bovet, N.; Andersen, J. N.; Baddeley, C. J.; Lundgren, E. *Phys. Rev. B* **2008**, *78*, 045423.
- [48] van Rijn, R.; Balmes, O.; Resta, A.; Wermeille, D.; Westerström, R.; Gustafson, J.; Felici, R.; Lundgren, E.; Frenken, J. W. M. *Phys. Chem. Chem. Phys.* **2011**, *13*, 13167.
- [49] Hendriksen, B. L. M.; Frenken, J. W. M. *Phys. Rev. Lett.* **2002**, *89*, 046101.
- [50] Grass, M. E.; Zhang, Y.; Butcher, D. R.; Park, J. T.; Li, Y.; Bluhm, H.; Bratlie, K. M.; Zhang, T.; Somorjai, G. A. *Angew. Chem. Int. Ed.* **2008**, *47*, 8893.
- [51] Butcher, D. R.; Grass, M. E.; Zeng, Z.; Aksoy, F.; Bluhm, H.; Li, W.-X.; Mun, B. S.; Somorjai, G. A.; Liu, Z. *J. Am. Chem. Soc.* **2011**, *133*, 20319.
- [52] Toyoshima, R.; Yoshida, M.; Monya, Y.; Kousa, Y.; Suzuki, Y.; Abe, H.; Mun, B. S.; Mase, K.; Amemiya, K.; Kondoh, H. *J. Phys. Chem. C* **2012**, *116*, 18691.
- [53] Surnev, S.; Sock, M.; Ramsey, M. G.; Netzer, F. P.; Wiklund, M.; Borg, M.; Andersen, J. N. *Surf. Sci.* **2000**, *470*, 171.
- [54] Kaichev, V. V.; Prosvirin, I. P.; Bukhtiyarov, V. I.; Unterhalt, H.; Rupprechter, G.; Freund, H.-J. *J. Phys. Chem. B* **2003**, *107*, 3522.
- [55] Raval, R.; Haq, S.; Harrison, M. A.; Blyholder, G.; King, D. A. *Chem. Phys. Lett.* **1990**, *167*, 391.
- [56] Lpcatelli, A.; Brena, B.; Lizzit, S.; Comelli, G.; Cautero, G.; Paolucci, G.; Rosei, R. *Phys. Rev. Lett.* **1994**, *73*, 90.

### 3.4 CO Adsorption on Pd<sub>70</sub>Au<sub>30</sub>(111) Alloy Surface: A Remarkable Enhancement of Top Site Occupation

#### Abstract

The adsorption of carbon monoxide (CO) on a Pd<sub>70</sub>Au<sub>30</sub>(111) alloy surface as a function of background CO pressure (ultrahigh vacuum-10 mTorr) was investigated using a combination of NAP-XPS and DFT simulation. The CO molecule preferentially adsorbs on top (bridge and hollow) site on isolated (contiguous) Pd site in accordance with density of the segregated Pd site, up to 10<sup>-6</sup> Torr CO background. With increasing the CO pressure (10 mTorr), the adsorption on top site becomes dominant on the surface. Such behavior is not observed on a pure-Pd(111) surface, suggesting that it is caused by inter-mixing with Au. Thermodynamic simulations, including the pressure-induced entropic term, indicate that the adsorption on top site is efficiently stabilized under the CO gas equilibrium conditions.

#### 3.4.1 Introduction

Oxidation of CO on PGM surfaces is a prototypical model system for understanding the heterogeneous catalysis. The atomic-scale reaction mechanism has been paid much attention in the field of surface science. Under the UHV environment, the reaction generally proceeds via the LH mechanism, where the reactants adsorb, diffuse, and react on the metallic surfaces. The experimental evidence of the mechanism is reported by Ertl and co-workers.

Recent technical developments enables us the in-situ observations under the (near) realistic environments with overcoming pressure and material gaps.<sup>1-5</sup> Here, the catalytically active surface is clearly different from that used in UHV-based experiments. In the case of Pd(111), the CO oxidation reaction proceeds on the oxidized surface under the sub-Torr environments (see Chapter 4)

Alloying sometimes alters the catalytic performance of a monometallic material, which is explained by several factors such as lattice distortion, charge transfer and so called ensemble effect.<sup>6-8</sup> The Pd-Au bimetallic alloy has the capability of chemical conversion of organic molecules and low-temperature CO oxidation. It is known that the Au rich layer is formed at the surface due to its low surface free energy.<sup>9-13</sup> On the other hand, high-pressure CO exposures to (100) and (110) open-surfaces lead to the surface segregation of internal Pd atoms, suggesting that the surface elemental composition strongly depends on the background environment.<sup>7,13</sup> However, as for close-packed (111) surface the number of studies is quite limited so far, even though nanometer-sized industrial catalysts are mainly composed of (111) surfaces, due to its thermodynamic stability. The strong bond formation between CO and metal surface at lower temperatures inhibit dissociative adsorption of O<sub>2</sub> and hence

catalytic reaction (CO-poisoning). The understanding of CO adsorption behavior improves the performance of the low-temperature CO oxidation catalysts.

Here, the in-situ observation of pressure dependence of Pd<sub>70</sub>Au<sub>30</sub>(111) alloy surface was performed using NAP-XPS. DFT simulation gives information on atomic-scale insight of the local structure and energetics with considering pressure induced effect.<sup>14,15</sup> With a combination of experimental and computational methods, the evolution of surface coverage and occupation of the adsorption sites are traced as a function of background pressure.

### 3.4.2 Experiment and Computational Methodology

In-situ XPS observations were performed at beamline 13A/B at KEK-PF. The base pressures of the analysis and sample preparation chambers were of the order of 10<sup>-10</sup> Torr. The monometallic and alloyed single-crystal surfaces were cleaned by repeated cycles of Ar<sup>+</sup> sputtering, surface oxidation and brief annealing (Pd, 1100 K; Au, 900 K; Pd<sub>70</sub>Au<sub>30</sub>, 1000 K). Incident photon energies were tuned such that the photoelectron kinetic energies are approximately 95 eV (Pd 3d, 430 eV; C 1s, 380 eV and Au 4f, 180 eV). CO gas (purity 99.95%) was dosed to the surfaces at 298 K. Obtained XP spectra were deconvoluted into several components via the curve fitting analysis using convoluted functions of Doniach–Šunjić and Gaussian functions and Shirley-type subtraction.

Computational simulations were carried out using VASP. The Kohn-Sham equations were resolved by the PAW method ( $E_{\text{cutoff}} = 400$  eV) with the PBE XC functional. The calculated bulk lattice constants were  $a_0 = 3.95, 4.17$  and  $4.01$  Å for Pd (A1), Au (A1) and Pd<sub>75</sub>Au<sub>25</sub> (L1<sub>2</sub> crystal), respectively, with 16<sup>3</sup>  $k$ -point sampling. Surfaces were constructed by the slab model (single surface/4-layer), where the 6<sup>2</sup>  $k$ -point sampling was carried out for the (2 × 2) supercell. The isolated CO molecule was put in orthorhombic box with single  $k$ -point. Adsorbed CO molecules and 1st and 2nd surface layers were fully relaxed until the residual forces on atoms are reduced to less than 0.05 eV Å<sup>-1</sup>. CLS simulations were carried out based on the Slater-Janak transition state approximation. Atomistic thermodynamic simulations were employed to reveal the pressure effect on the surface. Details of theoretical methods are described in Chapter 3.

### 3.4.3 Results and Discussion

The surface structure of Pd<sub>70</sub>Au<sub>30</sub>(111) is characterized by LEED and XPS. There is a possibility that the topmost surface reconstructs due to the surface strain, for instance the Au(111) surface shows so-called herringbone structure. While a (1×1) surface structure was observed for the Pd-Au(111) surface. Figure 3.4.1 shows the XP spectra for Pd 3d and Au 4f levels taken from Pd(111) (a and b), Au(111) (c and d) and Pd<sub>70</sub>Au<sub>30</sub>(111) (e and f) surfaces under UHV conditions. The peak overlapping

is a serious problem when multi-elemental system is measured by XPS. In the case of Pd-Au alloy, the Pd 3d<sub>5/2</sub> (typically 335 eV) and Au 4d<sub>5/2</sub> (335 eV), and the Au 4f<sub>7/2</sub> (84 eV) and Pd 4s (87 eV) overlap each other, though the Pd 3d<sub>5/2</sub> and Au 4f<sub>7/2</sub> give the sharpest/strongest peaks in each element. But the photoexcitation cross-section is different from each other, suggesting that the relative intensity is controllable by tuning the irradiation photon energy. Here the photon energies were tuned as 430 eV for Pd 3d and 180 eV for Au 4f levels. XP spectra from monometallic surfaces (a and d) were fitted into surface (S) and bulk (B) components.<sup>16,17</sup> While the alloy surface has three components in Pd 3d, which is clearly different from monometallic surfaces. The peaks are assigned to Pd in the 1st layer (S), in the 2nd layer (S') and in bulk (B), based on a previous study on Pd-Ag alloy. The atomic fraction of Pd atoms in the 1st layer is estimated to be approximately 30% from angle-dependent measurements. It suggests that the surface is covered by Au-rich layer. On the other hand, the Au 4f level is fitted into a single component, which may be explained by a small CLS between surface and bulk.

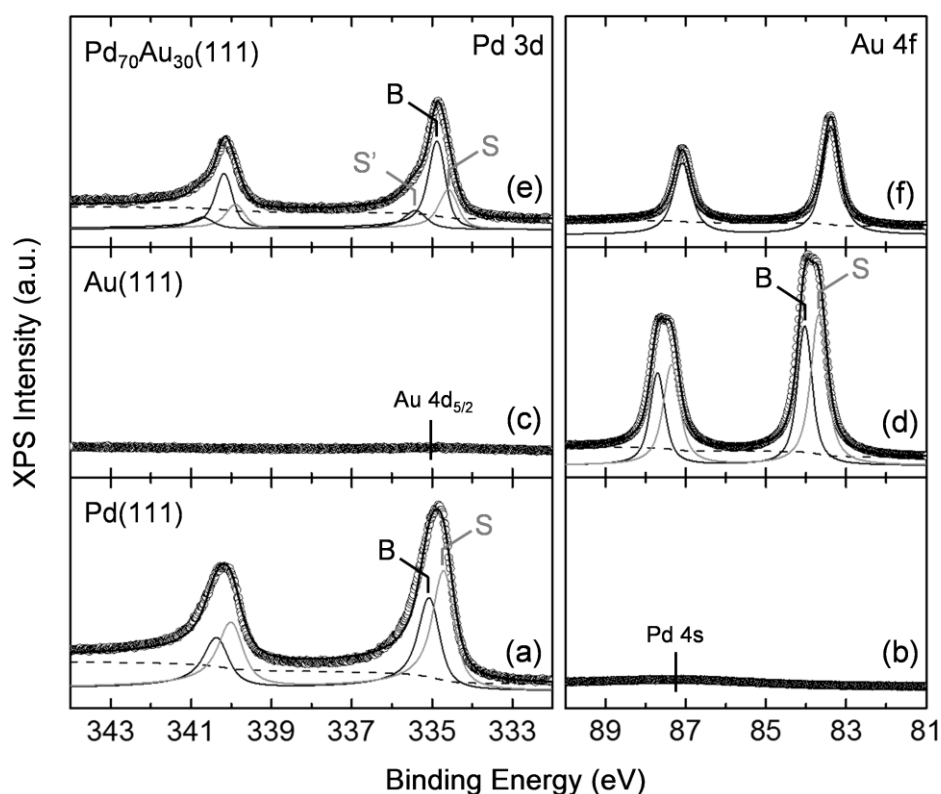


**Figure 3.4.1.** XP spectra for Pd 3d and Au 4f levels taken from CO-free Pd(111), Au(111) and Pd<sub>70</sub>Au<sub>30</sub>(111) surfaces at 298 K. All XP spectra are shown with curve fitting results, where each component indicates the bulk (B) and (near) surface (S and S') metal atoms. Adapted with permission from Ref. P-7. Copyright (2015) American Chemical Society.

The formation of Au-rich layer is also concluded by the theoretical simulation. Figure 3.4.2 shows the surface free energy diagram depending on the bulk stoichiometry. It reveals that the Au-rich surface is energetically favored (marked by black arrow). The segregation of Au atom is explained by the low surface free energy of pure-Au with respect to the pure-Pd.

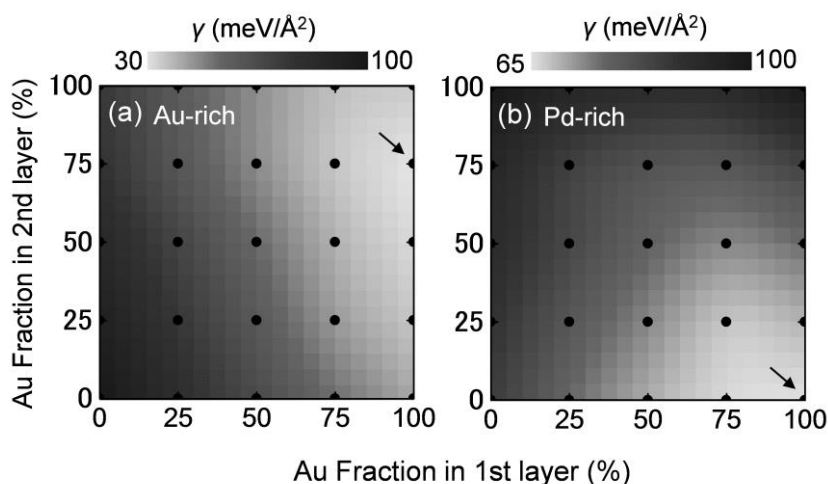


**Figure 3.4.2.** The simulated surface free energies ( $\gamma$ ) of  $\text{Pd}_{75}\text{Au}_{25}(111)$  on the Au-rich (a) and Pd-rich (b) limit as a function of surface composition. The black dots are the simulated geometries, and the black arrow indicates the most stable surface composition. Adapted with permission from Ref. P-7. Copyright (2015) American Chemical Society.

Then, the CO adsorption on Pd-Au alloy surface was observed up to 10 mTorr at 298 K. Figure 3.4.3 shows Pd  $3d_{5/2}$  and C 1s XP spectra taken at different CO pressures. The Pd  $3d_{5/2}$  level (a), taken from a CO saturated surface under UHV ( $p_{\text{CO}} < 10^{-8}$  Torr), shows appearance of two CO-induced components at the higher binding energy side. Based on the XPS results on CO/Pd(111) system (see Chapter 3.3), these are assigned as surface Pd atoms occupied by hollow site bonding CO ( $\text{Pd}_{1/3}$ ) and bridge site bonding CO ( $\text{Pd}_{1/2}$ ), where the index numbers indicate the number of bonding CO per Pd atom. The corresponding C 1s level (b) shows an asymmetric peak which consists of two components, CO molecules on hollow (h) and bridge (br) sites. CLS simulations well support the peak assignment discussed here (Table 3.4.1). It is noted that the CO-free surface Pd component (S) remains observable even though the surface is saturated with CO. The hollow and bridge site occupation suggests the existence of contiguous Pd sites i.e. dimer, trimer and more complex Pd domains. While, the isolated monomer-Pd site is also formed on the surface, which supplies the top site to the CO.

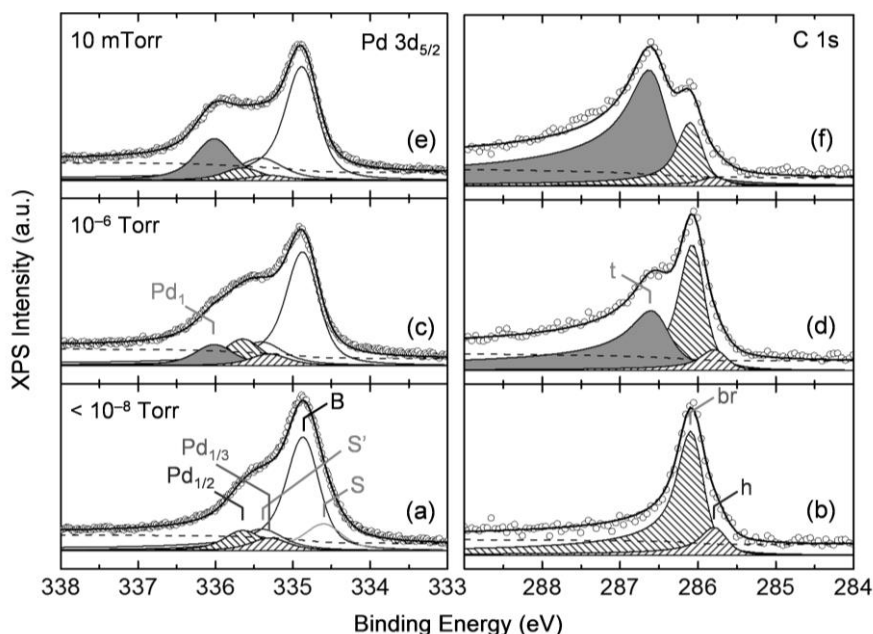


**Figure 3.4.3.** XP spectra for Pd 3d<sub>5/2</sub> and C 1s levels taken from Pd<sub>70</sub>Au<sub>30</sub>(111) surface at different CO pressures at 298 K. All the XP spectra are shown with curve fitting results, where each component indicates bulk (B), (near) surface (S and S') and CO-bonding Pd (Pd<sub>x</sub>) in Pd 3d<sub>5/2</sub> level and CO on hollow (h), bridge (br) and top (t) sites in C 1s level. Adapted with permission from Ref. P-7. Copyright (2015) American Chemical Society.

**Table 3.4.1.** Comparison between calculated and experimental CLSs for clean and CO-adsorbed Pd<sub>75</sub>Au<sub>25</sub>(111) surfaces. For the clean surface, the CLSs of the 1st layer (S) and the 2nd layer (S') atoms are calculated. For CO adsorbed surfaces, CO molecules are assumed to locate at hollow (h), bridge (br) and top (t) sites. The CO-binding Pd atoms are labelled as Pd<sub>x</sub>, where *x* is the coordination number of CO to the Pd atom. The reference species of Pd 3d and C 1s XPS are the bulk Pd and CO adsorbed at the hollow site, respectively. Adapted with permission from Ref. P-7. Copyright (2015) American Chemical Society.

system	level	label	calcd CLS (eV)	exp. CLS (eV)
Pd <sub>75</sub> Au <sub>25</sub> (111)	Pd 3d	S	-0.13 <sup>a</sup>	-0.26
		S'	+0.21 <sup>b</sup>	+0.54
CO/Pd <sub>75</sub> Au <sub>25</sub> (111)	Pd 3d	Pd <sub>1/3</sub>	+0.70	+0.45
		Pd <sub>1/2</sub>	+0.95	+0.76
		Pd <sub>1</sub>	+1.46	+1.14
	C 1s	br	+0.27	+0.30
		t	+0.75	+0.79

<sup>a</sup> the Pd atom in the 1st layer is modelled by an isolated (monomer) Pd bonding with two internal Pd atoms.

<sup>b</sup> the Pd atom in the 2nd layer is modelled by an isolated Pd atom underneath the Au surface layer.

The experimental data shows the CO molecules adsorb at the hollow and bridge sites, while the top sites are free from CO adsorption. Therefore, the CO-free surface Pd component (S) is associated with the monomer-Pd, and the CO adsorption on top site is not favored. The multiple-coordination sites consisting of both Pd and Au atoms are energetically less favored compared to those consisting of pure-Pd. The results are consistent with CO/Pd(111) system under UHV conditions as discussed in Chapter 3.3.<sup>16, 18-20.</sup>

At  $10^{-6}$  Torr CO ambient, the adsorption state is obviously changed as shown in Figure 3.4.3(c and d). The Pd  $3d_{5/2}$  level shows disappearance of S and appearance of a new component, labeled as Pd<sub>1</sub>. An additional shoulder structure at the higher binding energy side appears in C 1s level. These components are attributed to CO molecules adsorbed on top sites on monomer-Pd. The top CO component in C 1s level has a large asymmetric tail coming from the vibrational structure.<sup>23</sup> All Pd atoms on the surface interact with adsorbed CO at this moment. By increasing the background CO pressure, the top site on the monomer Pd is occupied by CO.

When the background CO pressure is increased up to 10 mTorr, the surface further changes as shown in Figure 3.4.3(e and f). The top site occupation becomes dominant, whereas the bridge and hollow occupation decrease instead. The significant increase of top CO occupation is not due to Pd segregation to the surface, because both the surface/bulk ratio of Pd and the Pd/Au ratio hardly change between  $10^{-6}$  Torr and 10 mTorr, suggesting that the surface restructuring by high-pressure CO does not occur in the present case. Site switching of adsorbed CO from multiple-coordination (hollow) sites to single-coordination (top) sites well explains this behavior.

The evolution of CO population depending on background pressure is shown in Figure 3.4.4. The CO coverages are estimated from C 1s XPS taken from CO-saturated Pd(111). The total CO coverage increases as a function of CO pressure. Under the UHV ( $p_{CO} < 10^{-8}$  Torr) condition, the estimated coverage of 0.077 monolayer (ML) on the alloy surface is significantly smaller than that on Pd(111) (0.5 ML), because the fraction of Pd to the surface is limited on the alloy and about a half of surface Pd is unavailable (monomer-Pd) in this condition. Above  $10^{-6}$  Torr, the top site occupation on monomer-Pd comes to contribute. And the increase of top site occupation stems from decrease of bridge and hollow site occupation, suggesting that the contiguous two Pd atoms accommodate two adjacent top COs at higher pressures. When the CO gas was pumped out, the surface coverage essentially goes back to the initial value. The site switching of CO is completely reversible with respect to CO pressure (the cycle 1 and 2 show similar trend). There is no segregation of dimer- nor monomer-Pd. The Pd atoms in (111) surface have nine nearest neighbors, thus is energetically more stable than those of the (100), (110) and stepped surfaces. This may explain the reason for that the Pd segregation does not occur on (111) surface.

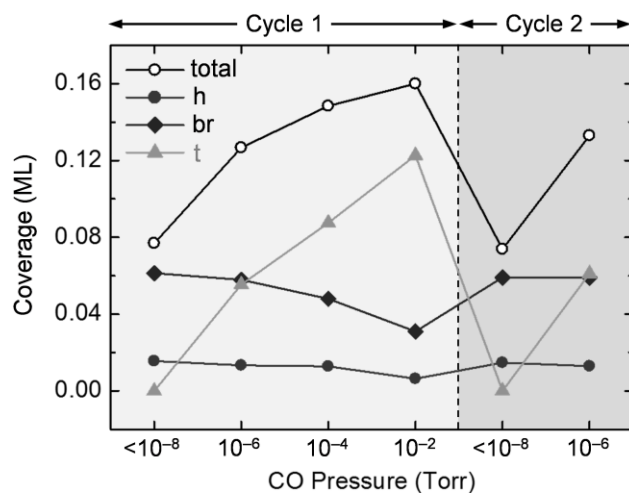


**Figure 3.4.4.** Evolution of fractional (h, br and t) and total CO coverages on a Pd<sub>70</sub>Au<sub>30</sub>(111) surface. The changes were deduced from C 1s XPS spectra. Adapted with permission from Ref. P-7. Copyright (2015) American Chemical Society.

Adsorption of CO on Au sites on CO/PdAu(100) was reported at room temperature under high CO pressures using a PM-IRAS.<sup>7</sup> To check whether there is or not a contribution of CO adsorbed on Au site, PM-IRAS measurements were performed under pressure conditions similar to those for the XPS measurements. Figure 3.4.5 shows the IRA spectra taken from Pd<sub>70</sub>Au<sub>30</sub>(111) at different CO pressures. Here the contribution from gaseous CO is cancelled out by the polarization modulation. A feature at  $\sim 1900\text{ cm}^{-1}$  is attributed to a C–O stretching mode of CO adsorbed on bridge and hollow sites. With increasing the CO pressure, the C–O stretching peak from CO on top site becomes dominant. The C–O stretching mode of CO adsorbed on Au should be observed at frequencies higher than that of Pd,  $> 2100\text{ cm}^{-1}$ . However the present result shows no such high-frequency peak. This is consistent with the XPS results. The contribution of CO adsorption on Au is negligibly small, even if it exists.

To address the effect of background pressure for switching of CO adsorption site, the atomistic thermodynamics framework was employed (Figure 3.4.6).<sup>14</sup> Here, the phase transitions for CO adsorption including only monomer Pd and dimer Pd are considered for simplicity. Under the low-pressure conditions (phase I), CO on bridge site of dimer-Pd is energetically stable, while, monomer Pd is too unstable to be adsorbed by CO. When the chemical potential increases above  $-1.2\text{ eV}$ , the CO on monomer Pd is stabilized and all the Pd sites are fully covered by CO (phase II). Further increase of chemical potential results in switching to the steeper line at  $-0.8\text{ eV}$ , from CO(br)/dimer-Pd to 2CO(t)/dimer-Pd (phase III).

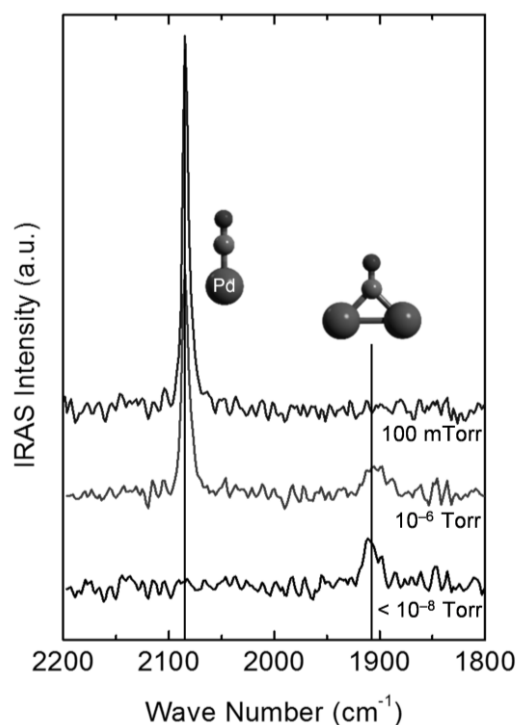


**Figure 3.4.5.** IRA spectra taken from Pd<sub>70</sub>Au<sub>30</sub>(111) under different CO pressure conditions at 298 K.

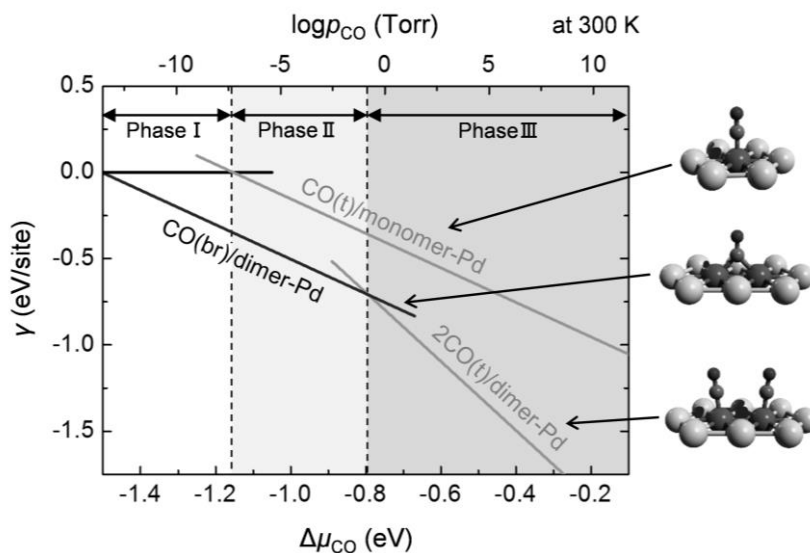


**Figure 3.4.6.** Simulated surface free energies  $\gamma$  for several CO adsorption models as a function of CO chemical potential, i.e. pressure. Here the energies are calibrated with respect to CO-free surfaces. The adsorption on top and bridge sites are indicated in gray and black lines, respectively. Corresponding model structures are shown in the right side. The fractions of Au in the first, the second and bulk layers are modeled as 75, 75 and 25%, respectively. Adapted with permission from Ref. P-7. Copyright (2015) American Chemical Society.

The top site CO is dominant on the alloy surface under 10 mTorr background, while this is minor species on the monometallic Pd(111) surface (see Chapter 3.3). This is partially due to the CO–CO steric repulsion between two adjacent on top COs. DFT calculations reveal that this repulsion is released by tilting away from each other (see model structure shown in right side). This tilting is enabled by the fact that the surface Pd ensembles are dispersed in the Au-rich surface layer.

The pressure-dependent site-switching of CO is well described by simulated surface free energies. C 1s XP spectra show the gradual site switching from bridge (hollow) to top site above  $10^{-4}$  Torr (Figure 3.4.4), while the simulation shows that the switching starts from  $10^{-1}$  Torr. This discrepancy of threshold pressure may be explained in terms that the surface consists of several local Pd configurations, for instance, 1-dimensional chain and 2-dimensional domain, which are not included in the present simulation. They exhibit different threshold pressure for the site switching.

Figure 3.4.7 shows the schematics of overall pressure dependence of adsorbed CO on the Pd<sub>70</sub>Au<sub>30</sub>(111) surface. The alloy surface has two types of Pd ensemble; namely monomer- and contiguous-Pd. In phase I ( $< 10^{-8}$  Torr), the CO molecules stably adsorb on multiple-coordination sites (bridge and hollow) formed on contiguous-Pd, whereas do not adsorb on top site on the monomer-Pd. In phase II ( $10^{-6}$  Torr), adsorption on the top site of monomer Pds is also allowed in the energetic point of view. In phase III (10 mTorr), the COs on contiguous Pd switch the adsorption sites from the multiply coordinated bridge (hollow) sites to the top site. The physical origin of site switching to the top site stems from the presence of background CO which causes changes in chemical potential. Thus the phase transition is intrinsically reversible for the background pressure.

The switch from the bridge (hollow) to the top site reduces the adsorption energy per molecule. It may alleviate the CO-poisoning effect, which leads to low-temperature CO oxidation reaction, i.e. the lower shift of light-off temperature. Recently theoretical studies on CO oxidation on PdAu surfaces proposed a unique reaction pass via a metastable state (OOCO formation), which requires the top site occupation of contiguous Pd ensembles.<sup>24-26</sup> The top site occupation is experimentally observed under the NAP condition in the present study.

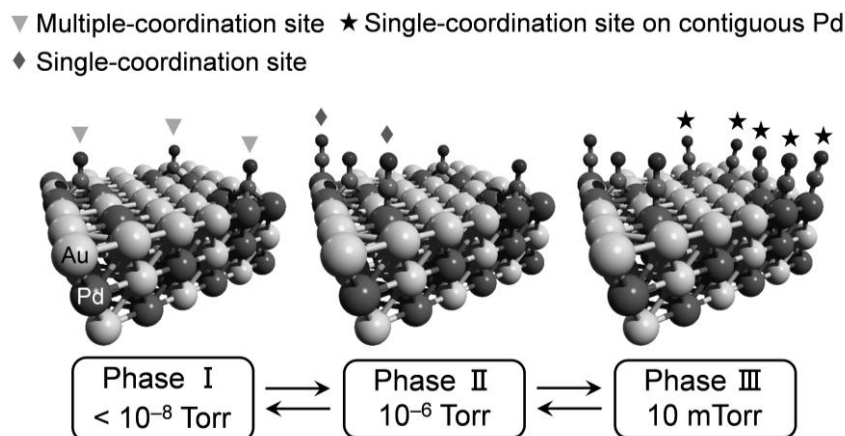


**Figure 3.4.7.** Summary of CO adsorption behavior on Pd<sub>70</sub>Au<sub>30</sub>(111) surface at different CO pressures. Phase I: CO adsorbs on bridge and hollow sites of contiguous dimer and trimer Pds dispersed on the surface. Phase II: CO adsorbs on top site on isolated monomer Pd. Phase III: The COs change adsorption sites from bridge and hollow sites to on top sites of contiguous Pds. Adapted with permission from Ref. P-7. Copyright (2015) American Chemical Society.

### 3.4.4 Conclusions

The pressure dependence of CO adsorption behavior on Pd<sub>70</sub>Au<sub>30</sub>(111) surface was investigated over the pressure range from UHV to 10 mTorr at room temperature using the combination of NAP-XPS and DFT simulation. It is found that the background CO pressure reversibly controls the CO adsorption site on the surface. The CO adsorption on top site is less favored in energetics under UHV, whereas, it dominates under 10 mTorr ambient. The DFT calculations support that the preferential top site occupation takes place at high chemical potential conditions caused by background high-pressure CO.

**References**

- [1] Hendriksen, B. L. M.; Frenken, J. W. M. *Phys. Rev. Lett.* **2002**, *89*, 046101.
- [2] Butcher, D. R.; Grass, M. E.; Zeng, Z.; Aksoy, F.; Bluhm, H.; Li, W.-X.; Mun, B. S.; Somorjai, G. A.; Liu, Z. *J. Am. Chem. Soc.* **2011**, *133*, 20319.
- [3] Toyoshima, R.; Yoshida, M.; Monya, Y.; Kousa, Y.; Suzuki, K.; Abe, H.; Mun, B. S.; Mase, K.; Amemiya, K.; Kondoh, H. *J. Phys. Chem. C* **2012**, *116*, 18691.
- [4] Blomberg, S.; Hoffmann, M. J.; Gustafson, J.; Martin, N. M.; Fernandes, V. R.; Borg, A.; Liu, Z.; Chang, R.; Matera, S.; Reuter, K. et al., *Phys. Rev. Lett.* **2013**, *110*, 117601.
- [5] Gustafson, J.; Shipilin, M.; Zhang, C.; Stierle, A.; Hejral, U.; Ruett, U.; Gutowski, O.; Carlsson, P.-A.; Skoglundh, M.; Lundgren, E. *Science* **2014**, *343*, 758.
- [6] Xu, J.; White, T.; Li, P.; He, C.; Yu, J.; Weikang, Y.; Han, Y.-F. *J. Am. Chem. Soc.* **2010**, *132*, 10398.
- [7] Gao, F.; Wang, Y.; Goodman, D. W. *J. Am. Chem. Soc.* **2009**, *131*, 5734.
- [8] Li, Z.; Gao, F.; Tysoe, W. T. *J. Phys. Chem. C* **2010**, *114*, 16909.
- [9] Chen, M.; Kumar, D.; Yi, C.-W.; Goodman, D. W. *Science* **2005**, *310*, 291.
- [10] Maroun, F.; Ozanam, F.; Magnussen, O. M.; Behm, R. J. *Science* **2001**, *293*, 1811.
- [11] Han, P.; Axnanda, S.; Lyubinetsky, I.; Goodman, D. W. *J. Am. Chem. Soc.* **2007**, *129*, 14355.
- [12] Piccolo, L.; Piednoir, A.; Bertolini, J. C. *Surf. Sci.* **2005**, *592*, 169.
- [13] Languille, M. A.; Ehret, E.; Lee, H. C.; Jeong, C. K.; Toyoshima, R.; Kondoh, H.; Mase, K.; Jugnet, Y.; Bertolini, J. C.; Aires, F. J. C. S.; Mun, B. S. *Catal. Today* **2016**, *260*, 39.
- [14] Zeng, Z.-H.; Ma, X.-F.; Ding, W.-C.; Li, W.-X. *Sci. China Chem.* **2010**, *53*, 402.
- [15] Kitchin, J.; Reuter, K.; Scheffler, M. *Phys. Rev. B* **2008**, *77*, 075437.
- [16] Surnev, S.; Sock, M.; Ramsey, M. G.; Netzer, F. P.; Wiklund, M.; Borg, M.; Andersen, J. N. *Surf. Sci.* **2000**, *470*, 171.
- [17] Chaudhuri, A.; Lerotholi, T. J.; Jackson, D. C.; Woodruff, D. P.; Dhanak, V. R. *Surf. Sci.* **2010**, *604*, 227.
- [18] Kaichev, V. V.; Prosvirin, I. P.; Bukhtiyarov, V. I.; Unterhalt, H.; Rupprechter, G.; Freund, H.-J. *J. Phys. Chem. B* **2003**, *107*, 3522.
- [19] Unterhalt, H.; Rupprechter, G.; Freund, H.-J. *J. Phys. Chem. B* **2002**, *106*, 356.
- [20] Ozensoy, E.; Meier, D. C.; Goodman, D. W. *J. Phys. Chem. B* **2002**, *106*, 9367.
- [21] Smedh, M.; Beutler, A.; Ramsvik, T.; Nyholm, R.; Borg, M.; Andersen, J. N.; Duschek, R.; Sock, M.; Netzer, F. P.; Ramsey, M. G. *Surf. Sci.* **2001**, *491*, 99.
- [22] Toyoshima, R.; Yoshida, M.; Monya, Y.; Suzuki, K.; Amemiya, K.; Mase, K.; Mun, B. S.; Kondoh, H. *Phys. Chem. Chem. Phys.* **2014**, *16*, 23564.
- [23] Föhlisch, A.; Wassdahl, N.; Hasselström, J.; Karis, O.; Menzel, D.; Mårtensson, N.; Nilsson, A. *Phys. Rev. Lett.* **1998**, *81*, 1730.
- [24] Yuan, D.; Gong, X.; Wu, R. *Phys. Rev. B* **2007**, *75*, 085428.
- [25] Yuan, D. W.; Liu, Z. R.; Chen, J. H. *J. Chem. Phys.* **2011**, *134*, 054704.
- [26] Ham, H. C.; Stephens, J. A.; Hwang, G. S.; Han, J.; Nam, S. W.; Lim, T. H. *J. Phys. Chem. Lett.* **2012**, *3*, 566.



## Chapter 4

# CO Oxidation Reaction on Low-Index Pd Surfaces: Experimental Evidence of An Alternative Reaction Mechanism

---

### Abstract

Catalytic oxidation of carbon monoxide (CO) to carbon dioxide (CO<sub>2</sub>) proceeding on Pd(111), (100) and (110) single-crystal surfaces have been investigated with near-ambient-pressure X-ray photoelectron spectroscopy under several hundred mTorr pressures. In-situ observations of the reaction revealed that two reaction pathways switch over alternatively as a function of temperature. At lower temperatures, the surfaces were dominantly covered by CO and hence the reaction rate was low (CO poisoning). At higher temperatures, the O-rich layers, surface oxides on (111) and (100), and dense chemisorbed-O phase on (110), were formed on the surface and it drastically accelerated the reaction rate. It is likely that the CO<sub>2</sub> formation rate depends on the amount of active oxygen species that form dense overlayers on Pd surfaces.

### 4.1 Introduction

Catalytic oxidation of carbon monoxide (CO) to carbon dioxide (CO<sub>2</sub>) on PGM surfaces has been extensively investigated over the past decades due to its industrial importance, for instance automotive exhaust converter. Many studies in surface chemistry have been performed on single crystal surfaces with using various surface sensitive tools in a wide pressure range. As well known, under UHV conditions, the reaction generally proceeds via the LH mechanism as discussed in Chapter 1. It is assumed that the metallic surface acts as the active sites, and no oxide species contributes to the reaction.<sup>1-5</sup> Another possible reaction mechanism is suggested for elevated pressure environments; it is so-called the M-vK mechanism, where the lattice oxygen species of the oxide reacts with chemisorbed CO. The relationship between surface condition and catalytic performance has been actively discussed. Recent in-situ surface observations performed under NAP conditions have proposed that the oxide formation accelerates the CO<sub>2</sub> formation rate.<sup>5-10</sup> While metallic surfaces

covered by a chemisorbed O is suggested as a highly active phase under similar NAP conditions.<sup>11</sup> A CO titration measurements to a partly oxidized Pt surface indicated that the reactivities of chemisorbed O and oxide were nearly equal.<sup>12</sup> Theoretical simulations have been conducted to investigate details of the reaction.<sup>15-17</sup> The atomistic understanding of CO oxidation process under ambient pressure conditions is still ambiguous.

The interactions of oxygen and further oxidation of the PGM surfaces have been investigated under various pressures and temperatures.<sup>19-25</sup> In the case of Pd(111) and (100) surfaces, it is revealed that the metal surfaces form oxidized phase with a high catalytic activity under reaction environments.

In my work, the catalytic CO oxidation reaction on Pd single-crystal surfaces under hundred mTorr pressures of CO and O<sub>2</sub> gases was studied by the synchrotron-based in-situ NAP-XPS and the differential-pumping MS. The phase transition from a CO-covered metal surface to the dense O covered surface, has close relevance to a drastic enhancement of the catalytic activity.

## 4.2 Experiment and Computational Methodology

All experiments were performed with an NAP-XPS system at beamline 13A/B at KEK-PF. Clean ordered surfaces of Pd(111), (100) and (110) single-crystals were obtained by the repeated cycles of Ar<sup>+</sup> sputtering, surface treatment under oxygen and brief annealing (e.g. 800 °C). Surface orientation and cleanness were checked by LEED and XPS. The CO and O<sub>2</sub> gases were introduced into the high-pressure analysis chamber up to hundreds mTorr via variable leak valves. The incident photon energy was tuned to 435 eV for Pd 3d<sub>5/2</sub> and C 1s, and 650 eV for O 1s levels (electron kinetic energies were approximately 100 eV). The BE scale was calibrated with respect to the Fermi edge. Because the photoemission intensity is attenuated by ambient-pressure gas, the C 1s and O 1s intensities were normalized by the integrated intensity of the Pd substrate. The catalytic conversion was simultaneously monitored by MS with in-situ XPS under the reaction conditions.

DFT simulations were employed for the Pd(100) surface to give assignments to the observed XPS peaks. DFT calculations were performed using VASP. The PAW method, which was expanded to 400 eV, and GGA-PBE were employed for the description of electron-ion interactions and the exchange-correlation functional, respectively. For the bare Pd metal, the equilibrium lattice constant is  $a_0 = 3.90 \text{ \AA}$ . The 1-ML oxide layer was modeled on slab layers with  $(\sqrt{5} \times \sqrt{5})R27^\circ$  periodicity, where the  $(5 \times 5 \times 1)$   $k$ -point mesh was used. The surface layers, and adsorbed molecules were allowed to relax. CLS simulations were carried out by using the Slater-Janak transition state approximation.

### 4.3 Results and Discussion

#### CO Oxidation on Pd(100)

Figure 4.1(a) shows the Pd 3d<sub>5/2</sub> XP spectra taken from metallic and surface oxidized Pd(100) surfaces. On the metallic surface, two distinct components assigned to bulk (B) and topmost surface (S) Pd atoms. Additional three oxygen-induced components are observed (denoted by I, 2f and 4f) on the surface oxidized surface. A LEED pattern and the corresponding model structure of surface oxide is shown in (b, c). There are two-types of Pd atoms, with an atomic ratio of 1:1, in the ( $\sqrt{5} \times \sqrt{5}$ )R27° square unit cell. The CLS calculations strongly support the assignments to the peak components obtained from the fitting analyses (Table 4.1).

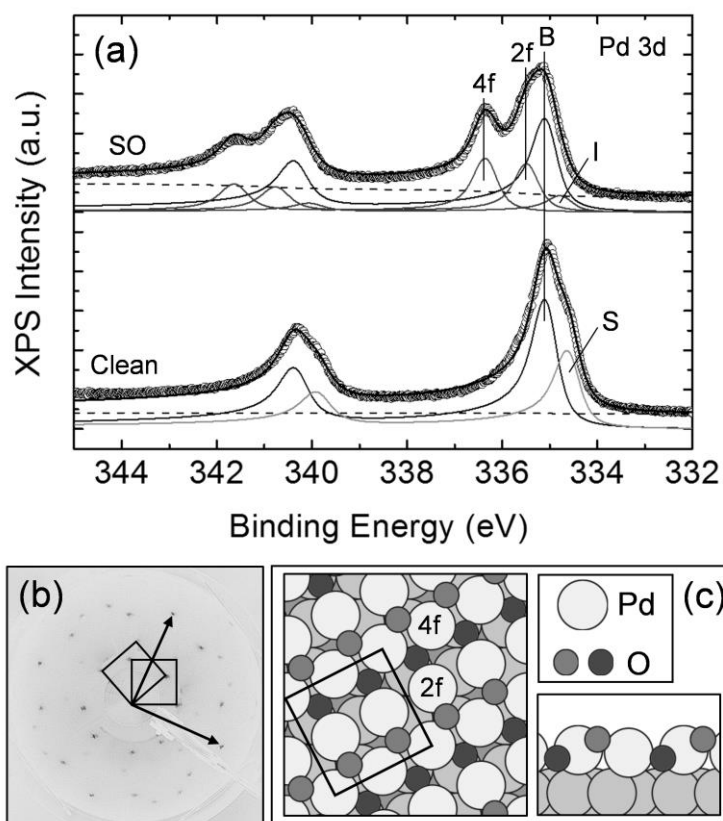


**Figure 4.1.** (a) XP spectra taken from clean metallic and surface oxide (SO) surface. (b) LEED pattern taken from SO/Pd(100) surface. (c) top and side views of model structure of SO formed on Pd(100) surface, where two types of surface Pd atoms are labeled (2f and 4f). Adapted with permission from Ref. P-2. Copyright (2012) American Chemical Society.

**Table 4.1.** Calculated and experimental CLSs of Pd 3d<sub>5/2</sub> and O 1s levels for clean and surface oxide surfaces. Adapted with permission from Ref. P-2. Copyright (2012) American Chemical Society.

System	Level	label	calcd CLS (eV)	Exp. CLS (eV)
clean	Pd 3d	B	0.0	0.0
		S	-0.47	-0.3
surface oxide	Pd 3d	I	-0.16	-0.3
		2f	+0.54	+0.5
		4f	+1.31	+1.3
		O 1s	0.0	0.0
	bottom	+0.55	+0.8	

Figure 4.2 shows the results of in-situ monitoring of MS and XPS data taken under catalytic CO oxidation reaction under NAP conditions. The dosing pressures of CO and O<sub>2</sub> gases were 20 and 200 mTorr, respectively. Figure 4.2(a) shows temperature dependence of CO<sub>2</sub> (m/e = 44) formation rate. The CO<sub>2</sub> formation rate is drastically increased above 190 °C. However, a decay of the rate is observed in the higher temperature regime. Labels (A, B, C and D) indicate the temperatures, where XP spectra are recorded, and each XP spectrum denoted by the labels in the Pd 3d<sub>5/2</sub> and C 1s levels (b and c).

At point A (room temperature), the CO<sub>2</sub> formation rate is low. The corresponding Pd 3d<sub>5/2</sub> and C 1s XP spectra indicate that a large amount of CO molecules cover the metallic Pd surface. Here it is assumed that the CO molecules form the p(3√2 × √2)R45° overlayer ( $\theta = 0.67$ ) as discussed in chapter 3. This phase can be regarded as “CO-poisoning”. Metal carbonyl species, which is a typical contaminant, is not detected in the C 1s level. It is noted that a weak and broad feature assigned to atomic carbon can be seen at around 283–285 eV in the C 1s level. Even if all of the atomic carbon locates on the surface, most of the surface is covered by CO molecules. However, the residual of atomic carbon affects the Pd 3d<sub>5/2</sub> spectra, because the Pd atoms binding to the residual carbon give a Pd 3d<sub>5/2</sub> component at around 335.4 eV. At point B (175 °C), the CO<sub>2</sub> intensity is still low, but the CO coverage on the surface is reduced, which is assigned to a p(2√2 × √2)R45°-like overlayer. These results indicate that the CO adsorption on the surface hinders the oxygen adsorption and hence the catalytic oxidation reaction is suppressed.

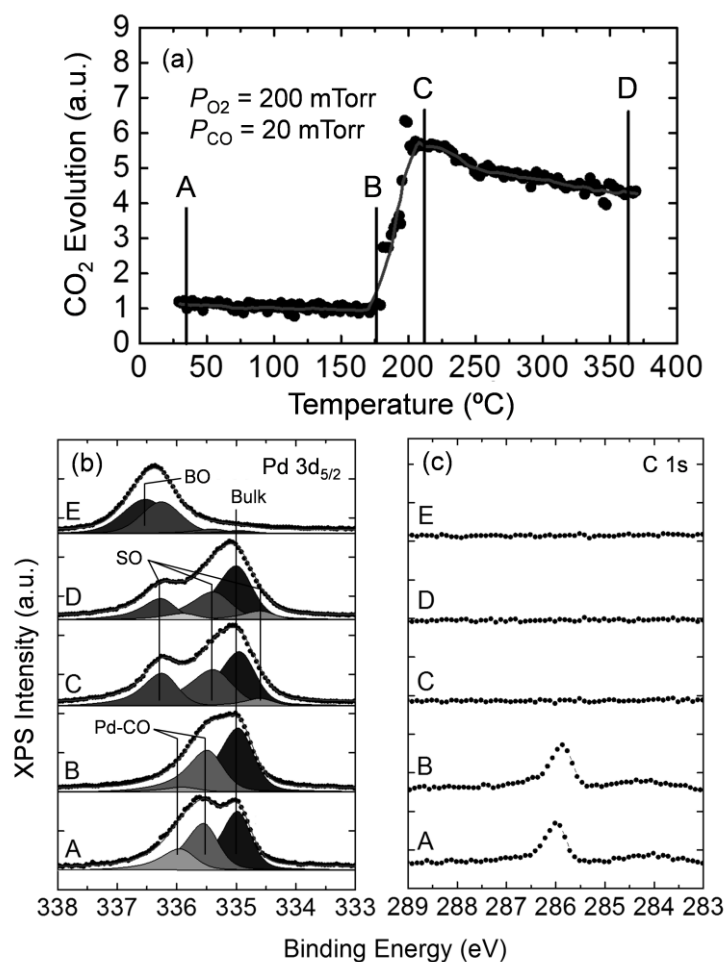


**Figure 4.2** (a) evolution of CO<sub>2</sub> production under exposure to 200 mTorr of O<sub>2</sub> and 20 mTorr of CO. Labels (A, B, C, and D) indicate temperature where XP spectra were recorded. (b, c) XP spectra for Pd3d<sub>5/2</sub> and C1s levels taken from Pd(100) surface under the reaction environments. Adapted with permission from Ref. P-2. Copyright (2012) American Chemical Society.

At point C, just above the catalytic light-off temperature (190 °C), spectral shape of Pd 3d<sub>5/2</sub> drastically changes, where three new components appear. The binding energies of these components suggest the formation of the ( $\sqrt{5} \times \sqrt{5}$ )R27° surface oxide (SO).<sup>32-3433-35</sup> CLS simulations for this surface oxide also support experimental results. At that time, C 1s XPS shows a flat feature, indicating disappearance of CO on the surface. Li et al. have found a possibility of coexistence of metallic and oxide domains under the catalytic conditions, and proposed that CO adsorbs on the metallic surface then react with oxygen atoms included in the coexisting oxide.<sup>24,25</sup> Chemisorbed O species gives peaks experimentally at 335.5 eV and 529.6 eV in the Pd 3d<sub>5/2</sub> and O 1s levels, respectively. However the present XPS results do not show evidence for coexistence of these species.

It should be noted that when only the CO gas is exposed to the metallic Pd surface above the light-off temperature, CO molecules can readily adsorb on the surface as measured in Pd 3d<sub>5/2</sub> XPS.

This indicates that the phase transition to the reactive surface condition is not induced by thermal CO desorption and consequent oxidation of the surface, but by equilibrium of adsorption of CO and O<sub>2</sub> on the surface. The CO adsorption easily proceeds even at low temperatures via the non-activated precursor-mediated mechanism. While the O<sub>2</sub> adsorption is enhanced at elevated temperatures, because it needs a thermal activation to dissociate to atomic species on the surface. Thus, at higher temperatures, the O<sub>2</sub> adsorption rate is faster than that of CO. The switchover of adsorption rate intrinsically changes the surface situation.

The catalytic performance is gradually decreased with increasing the temperature above the catalytic light-off. At point D (370 °C), the Pd 3d<sub>5/2</sub> XP spectrum shows a reduction of the surface oxide intensity. A new component appears at 335.9 eV instead, which is attributed as a “partly reduced” surface Pd species. A part of surface oxide is reduced by reaction with CO, and results in formation of less coordinated Pd. The decrease of the surface oxide causes the catalytic decay. At high temperatures, since the catalytic reaction, in other words removal of oxygen, is faster than the recovery of the oxide. If the MvK mechanism proceeds on the surface, the CO adsorbs on the oxide surface, and then reacts with an oxygen atom included in the oxide lattice. Therefore, the reduction of oxide phase decreases the amount of active center of the reaction and hence CO<sub>2</sub> formation rate. When the gas composition was switched to oxidizing condition by stopping CO supply with remaining O<sub>2</sub> exposure at 370 °C, the PdO bulk oxide (denoted as BO) was formed on the surface (point E), where the 4-fold Pd species at 336.5 eV is a sign of PdO. This result indicates that CO is continuously supplied to the surface under the reaction conditions. Therefore the surface is not under the CO depleted condition, in other word mass transfer limit, during the reaction (A–D). The bulk oxide is formed above 230 °C under O<sub>2</sub> only dose (200 mTorr) condition. However the Pd surface is covered by the surface oxide under the reaction conditions, and the bulk oxide formation at the higher temperatures above 230 °C is hindered by the reaction.

O 1s XP spectra are measured under the highly reactive condition (point C and D) (Figure 4.3). Two oxide induced components centered at 528.8 eV and 529.6 eV with almost equal intensities are obtained by curve fitting at point C, and they are associated with the ( $\sqrt{5} \times \sqrt{5}$ )R27° surface oxide.<sup>33,35,32,34</sup> The surface oxide has an O-Pd-O tri-layer structure, where The lower- and higher energy components are attributed to the outer- and inner- O species, respectively.<sup>33-35,32-34</sup> These assignments are well supported by the CLS simulations as shown in Table 4.1. At point D, where the CO<sub>2</sub> formation rate decreases compared with that at point C. At that time, the lower-energy component is weakened in intensity, while the higher-energy component essentially unchanged, suggesting that the upper-side O species is reactive and exclusively consumed. The lack of upper-side O is explained as selective reduction of the surface oxide via the MvK-like mechanism.

Numbers of previous studies have reported the drastic change from an inactive to an active surface under various O<sub>2</sub> and CO pressures.<sup>12,13,18</sup> They reported that after the catalytic light-off, the

surface are more or less covered by (some) oxide species. The surface oxide formation is the first step for further oxidation. The sudden jump of CO<sub>2</sub> formation rate as discussed in the previous studies might be correlated to the formation of the surface oxide, although further studies are necessary.

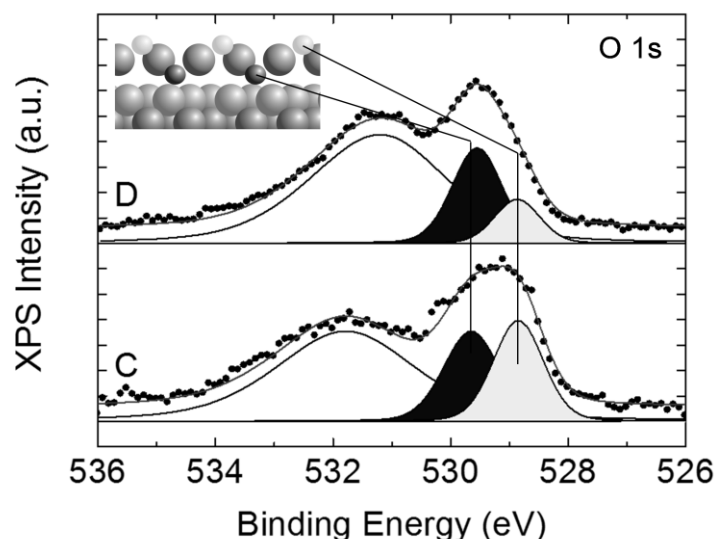


**Figure 4.3.** O1s XP spectra under catalytic conditions taken at point C and D. The CO<sub>2</sub> formation rate decreases from C to D, with increasing the temperature. Model structure of the  $(\sqrt{5} \times \sqrt{5})R27^\circ$  surface oxide formed on Pd(100) is shown in inset. A broad feature at a higher binding energy is a contribution from Pd 3p<sub>3/2</sub> level. Adapted with permission from Ref. P-2. Copyright (2012) American Chemical Society.

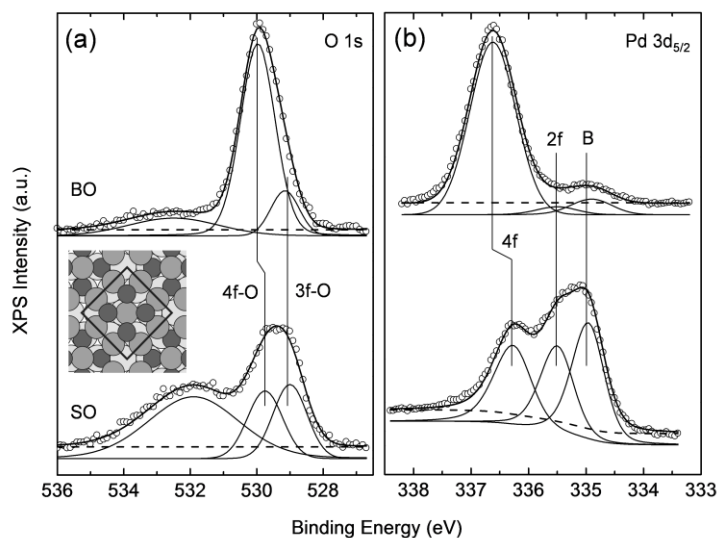
### CO Oxidation on Pd(111)

Figure 4.4 shows O 1s and Pd 3d<sub>5/2</sub> XP spectra taken from a surface oxide and a bulk oxide formed on Pd(111) surfaces. These surfaces were prepared under O<sub>2</sub> ambient ( $2 \times 10^{-1}$  Torr) by heating the surface (300–500 °C). Two distinct components assigned to 2-fold and 4-fold Pd (2f and 4f), excepting the bulk contribution are observed in Pd 3d<sub>5/2</sub> level. A model structure of the surface oxide is shown in inset. The bulk oxide formation induces an increase of the 4-fold Pd with a slight shift of binding energy.

Next, the Pd(111) surface was observed under catalytic reaction conditions. XP spectra taken from a Pd(111) surface at 200 °C with monitoring reactant and product gas compositions (O<sub>2</sub>, CO and CO<sub>2</sub>). Figure 4.5 shows evolution of MS signals (a), and O 1s and Pd 3d<sub>5/2</sub> XP spectra (b and c) under catalytic conditions at 200 °C. When the reactant O<sub>2</sub> (200 mTorr) and CO (20 mTorr) were introduced to the chamber (Region  $\alpha$ ), the CO<sub>2</sub> formation rate was quite low. At this moment the CO molecules are adsorbed at all of possible adsorption sites (hollow, bridge, and top) on the Pd(111) surface, judged from XP spectra taken from O 1s (b) and Pd 3d<sub>5/2</sub> (c) levels, which is consistent with the previous

studies.<sup>33,34</sup> C 1s XP spectra also show the adsorption of CO on the Pd surface. Whereas signals from chemisorbed O and/or oxide species are under the detection limit. In this regime, the surface are dominantly covered by the CO (CO poisoning), resulting in suppression of dissociative O<sub>2</sub> adsorption onto the surface. It is a general trend that the high-coverage CO adsorption suppresses the catalytic reaction on PGM surfaces.<sup>35</sup>

The CO<sub>2</sub> production gradually increases (Region  $\beta$ ) with increasing the O<sub>2</sub> pressure, and a new peak appears at lower-binding energy side (529.8 eV) in O 1s level. It is assumed that this peak originates from atomic O, but the binding energy is higher than that of the typical value of chemisorbed O (~529.2 eV). The subsurface O reported in a previous study<sup>36</sup> matches with the binding energy, thus the new peak is assigned to the subsurface O. This peak attribution well explains the behavior of this peak to the CO. When the O<sub>2</sub> exposure was stopped and switched to the CO titration condition (Region  $\gamma$ ), this peak remained on the surface without loss of intensity, suggesting that the species is less reactive even under the CO rich condition. The inactivity of this O suggests that it is buried underneath the surface.<sup>36</sup> It is reported that the formation of subsurface O species during the CO oxidation reaction accelerates the catalytic performance,<sup>11</sup> which is consistent with the present observation. The amount of irregular sites, e.g. defects may act as the channel for O penetration to the subsurface.



**Figure 4.4.** O 1s (a) and Pd 3d<sub>5/2</sub> (b) XP spectra taken from surface oxide (SO) and bulk oxide (BO) formed on Pd(111) surface. A model structure of the surface oxide is shown in inset. Adapted with permission from Ref. P-1. Copyright (2012) American Chemical Society.

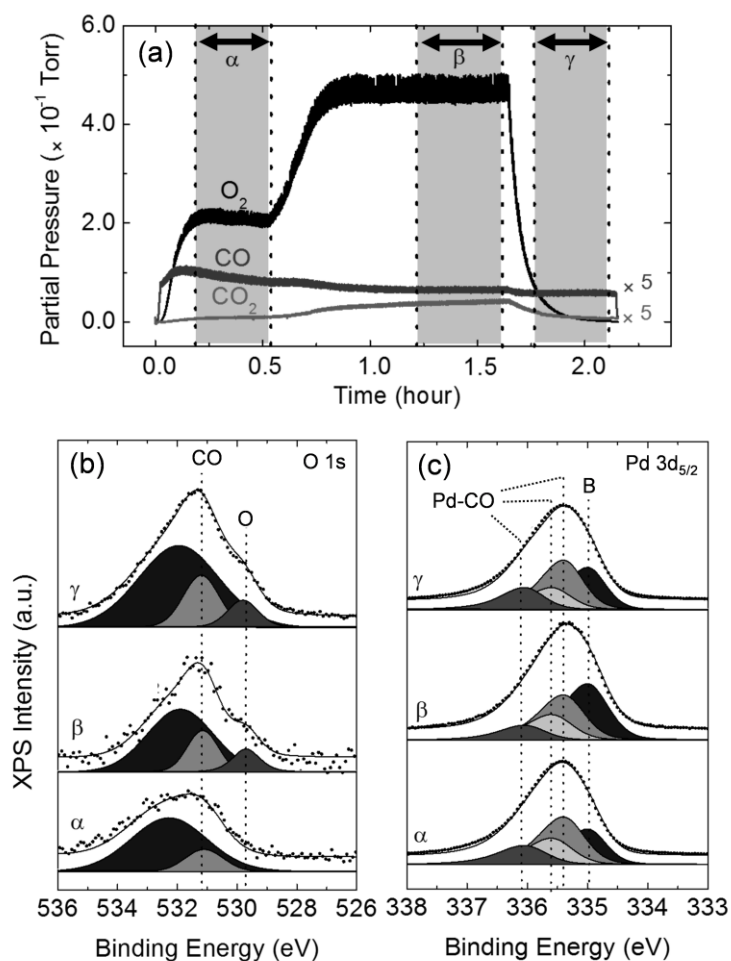


**Figure 4.5.** In-situ monitoring of catalytic CO oxidation on Pd(111) surface at 200 °C. Evolution of  $O_2$ , CO, and  $CO_2$  gases (a), and corresponding XP spectra for O 1s (b) and Pd 3d<sub>5/2</sub> (c). Adapted with permission from Ref. P-1. Copyright (2012) American Chemical Society.

Figure 4.6 shows evolution of MS signals (a) and corresponding XP spectra (b and c) under catalytic reaction conditions at 300 °C. CO does not stably adsorb on the Pd surface at this temperature. The disappearance of CO poisoning causes the drastic change of surface chemical condition with respect to that at 200 °C. The  $CO_2$  production significantly increased when the  $O_2$  and CO were introduced at a time (region  $\alpha$ ). The drop of CO partial pressure indicates that most of the introduced CO was converted to  $CO_2$ . The corresponding O 1s XP spectrum shows an appearance of a new component at around 530 eV, which is curve fitted into two components centered at 529.1 and 529.8 eV. It is a sign of the  $\sqrt{6}$  surface oxide ( $Pd_5O_4$ ) formation on the surface. The 529.1 and 529.8 eV components are associated with three-fold-coordinated oxygen (3f-O) and four-fold-coordinated oxygen (4f-O), respectively.<sup>37</sup> The 3f-O species is located at the upper side of the surface oxide and reactive to CO as confirmed below. The Pd 3d<sub>5/2</sub> XP spectrum also exhibits two oxide-induced peaks centered at 335.4 and 336.2 eV, in addition to the bulk one. The intensity ratio of the oxide peaks is almost 4:1, which

is consistent with that for the ordered surface oxide.<sup>37-39</sup> These data show that the surface oxide is formed under the highly active condition (region  $\alpha$ ). Here this surface is called as “active state”.

Next, the O<sub>2</sub> partial pressure was increased up to 600 mTorr (region  $\beta$ ). This results in a decrease of the CO<sub>2</sub> formation rate, suggesting that the surface changes to “less active state” in the O<sub>2</sub> rich feed. The O 1s XP spectrum taken under the condition (region  $\beta$ ) shows a new component centered at 530.5 eV, attributed to an O-deficient oxide, which may locate on the active  $\sqrt{6}$  surface oxide resulting in suppression of the reactivity. Thus, the difference between “active state” and “less active state” is determined by the availability of the reactive oxygen (3f-O) of the surface oxide. As the third step, the dose of O<sub>2</sub> was stopped and switched to the CO titration condition (region  $\gamma$ ).

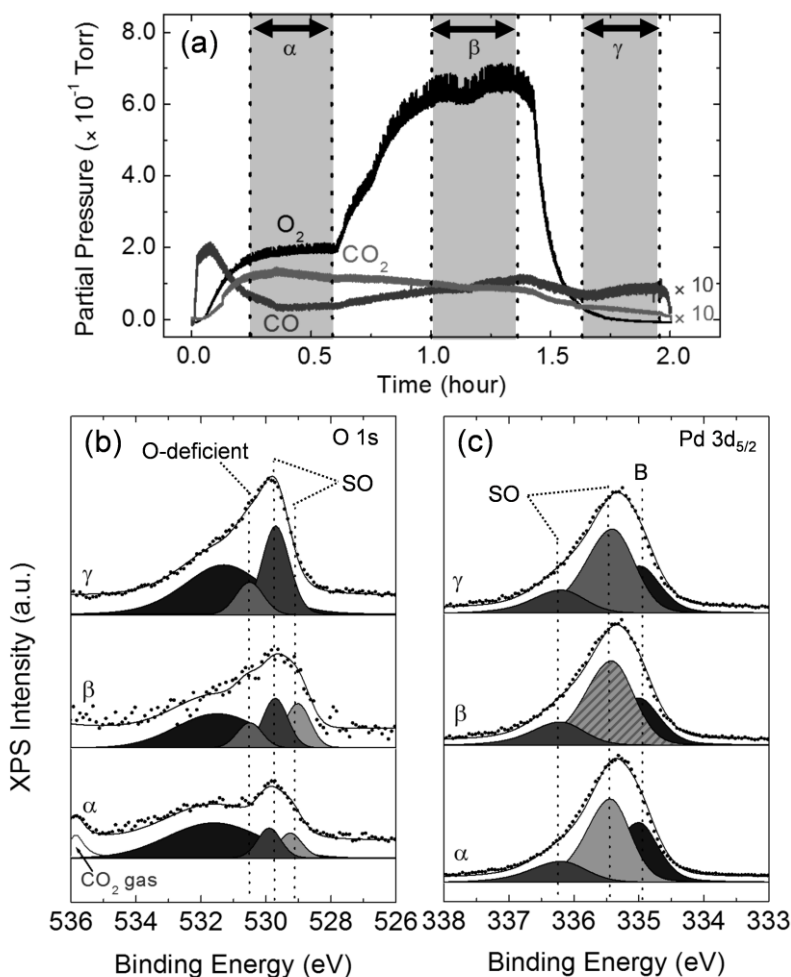


**Figure 4.6.** In-situ monitoring of catalytic CO oxidation on Pd(111) surface at 300 °C. Evolution of O<sub>2</sub>, CO, and CO<sub>2</sub> gases (a), and corresponding XP spectra for O 1s (b) and Pd 3d<sub>5/2</sub> (c). Adapted with permission from Ref. P-1. Copyright (2012) American Chemical Society.

Here the O 1s XP spectrum exhibits the complete consumption of 3f-O of the surface oxide, which confirms that the 3f-O of the surface oxide lattice react with CO. Whereas, the higher binding energy components (4f-O and O-deficient oxide) did not change under CO titration, indicating that these oxygen species are not reactive to CO.

### CO Oxidation on Pd(110)

First, the interactions between O<sub>2</sub> and Pd(110) surface were investigated. Figure 4.7 shows XP spectra of O 1s (a) and Pd 3d<sub>5/2</sub> (b) levels for a Pd(110) surface obtained at different temperature and pressure conditions. At 10<sup>-7</sup> Torr O<sub>2</sub> ambient at room temperature, the Pd 3d<sub>5/2</sub> XP spectrum was curve fitted into several O-induced components in addition to the bulk one. The O 1s XP spectrum exhibits a peak centered at 529.2 eV, which is attributed to the chemisorbed O. A broad contribution at the higher binding energy side is attributed to the Pd 3p<sub>3/2</sub> peak. Judging from the spectral features of Pd 3d<sub>5/2</sub> and O 1s levels, the O-induced c(2 × 4) overlayer is formed on the surface (Figure 4.7(c)). It consists of three types of O-bonding surface Pd atoms. The difference of these Pd species is associated with different coordination numbers of O. Bonding with an O atom leads to electron transfer from Pd to O. Therefore the higher coordinated Pd gives a higher binding energy in Pd 3d<sub>5/2</sub> level.<sup>43</sup> If the surface is completely covered by the c(2 × 4) overlayer as illustrated in Figure 4.7(c), the intensity of each peak with a different coordination number, should be same. However the actual intensity are not equal which means that a further dense O overlayer is partly formed in addition to the c(2 × 4) phase on the surface, and/or a photoelectron diffraction effect modulates the intensities.

Under 10<sup>-5</sup> Torr exposure, the O-free surface component disappears, whereas the O-induced components increases (335.4 and 335.6 eV). It suggests that the formation of a dense chemisorbed O phase. The O 1s XP spectrum was curve fitted into three components excepting the contribution of Pd 3p<sub>3/2</sub> level. Based on the previous studies, these features are a sign of the formation of the high density chemisorbed oxygen phases with (7 × √3) and (9 × √3) periodicities.<sup>42,43</sup> The component at the lower binding energy side is attributed to the Pd atoms underneath the surface Pd layer. A model structure of the (7 × √3) structure is illustrated in Figure 4.7(d). The atomic row on the (1 × 1) surface splits into strings consisting of seven Pd atoms and the O atoms sandwich the Pd strings from both sides.<sup>42,43</sup> This O species does not penetrate into the subsurface, meaning of not forming an O-Pd-O tri-layer structure. Although an appearance of four-fold coordinated Pd atom is a sign of oxide formation, the binding energies of the O-binding Pd atoms hardly change from those of the c(2 × 4) overlayer and the four-fold coordinated Pd is absent. While the two-fold coordinated Pd species are dominant even on the dense O overlayer. Therefore the chemical state of oxygen species in the dense structure measured at 10<sup>-5</sup> Torr is not associated with a surface oxide but with a chemisorbed phase. Then the O<sub>2</sub> pressure was increased up to 200 mTorr at room temperature. At this moment the spectral shapes

of Pd 3d<sub>5/2</sub> and O 1s levels essentially remain unchanged with one exception of gas-phase contributions (not shown). The dense chemisorbed phase keeps its structure even under the NAP conditions.

Next, the Pd surface was heated up to 300 °C under 200 mTorr O<sub>2</sub> ambient. The spectral shape of Pd 3d<sub>5/2</sub> level shows slight changes of surface chemical situation, where a small peak centered at 336.3 eV appears. The coordination number of Pd atom forming the bulk oxide is four, resulting in the highest binding energy. This is a sign of the PdO bulk oxide formation.<sup>43,44</sup>

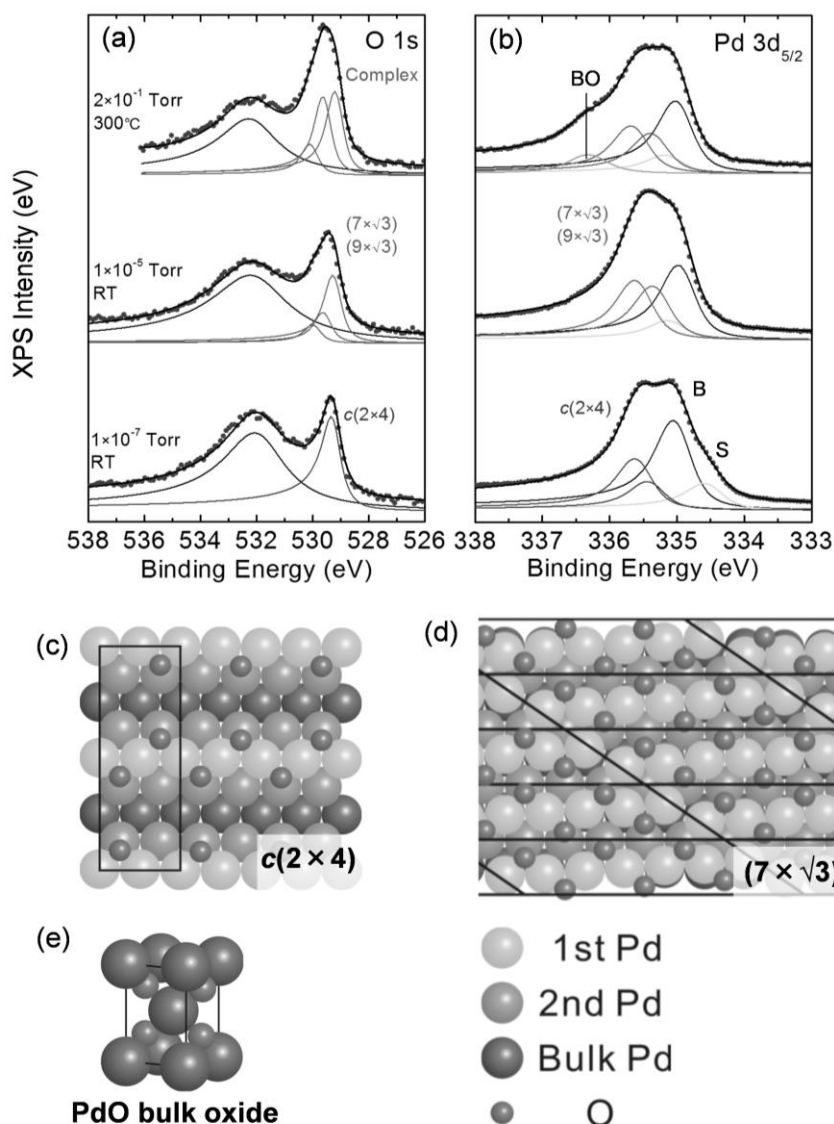


**Figure 4.7.** XP spectra of O 1s (a) and Pd 3d<sub>5/2</sub> (b) levels of the Pd(110) surface taken under various pressure and temperature conditions. The XP spectra are curve fitted into several components. Model structures of chemisorbed oxygen (c and d) and the PdO bulk oxide (BO) (e). Adapted with permission from Ref. P-4. Copyright (2013) American Chemical Society.

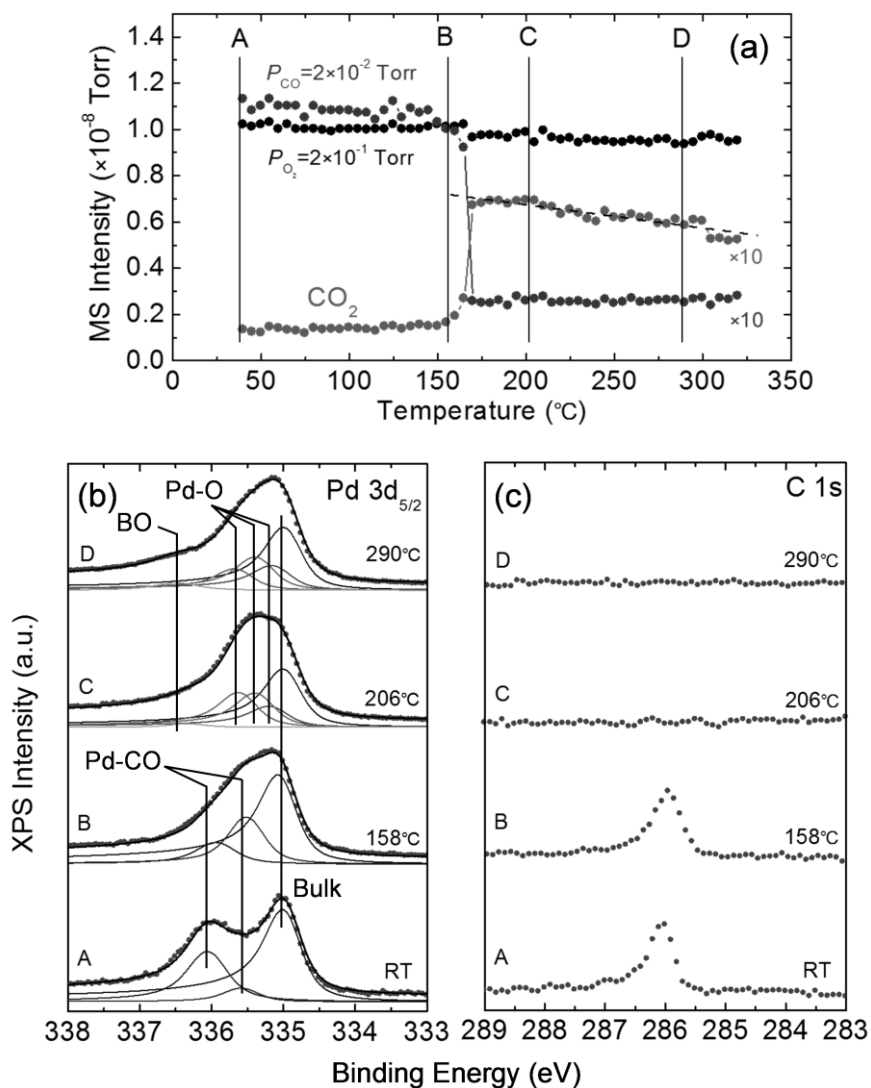
The components of the chemisorbed O phase are observable, but their relative contribution are weakened, because a part of the chemisorbed O on the surface is converted into the bulk oxide. Here the chemisorbed O and the bulk oxide coexist on the surface (complex structure).<sup>43,44</sup> The intensity ratio of the three oxygen components in O 1s is also changed, which is resulted from the contribution of the bulk oxide. A structure model of the bulk oxide is also shown in Figure 4.7(e).

Figure 4.8 presents in-situ monitoring of mass signals and corresponding XP spectra (b, and c) for catalytic CO oxidation proceeding on a Pd(110) surface under a constant reactant gas dose (O<sub>2</sub>, 200 mTorr; CO, 20 mTorr). Figure 4.8(a) shows the evolution of catalytic performance as a function of temperature by tracing the O<sub>2</sub> (m/e = 32), CO (28) and CO<sub>2</sub> (44) gases. At lower temperatures (< 165 °C), the CO<sub>2</sub> formation rate was very slow. With increasing the temperature, the reaction rate is drastically increased above 165 °C (catalytic light-off). Further heating up to 320 °C results in a 20% decrease of the reactivity with respect to the maximum (200 °C). Labels A, B, C, and D shown in Figure 4.8(a) indicate the temperatures, where XP spectra were recorded and corresponding Pd 3d<sub>5/2</sub> and C 1s XP spectra are shown in bottom panels (b and c). At room temperature (point A), judged from C 1s XP spectrum, the metallic surface is covered by the CO. Here the surface is free from atomic C and carbonyl species. By the curve fitting of Pd 3d<sub>5/2</sub> level, the overlayer structure of CO is identified as the (2 × 1)p2mg-2CO structure, suggesting CO poisoning.

At point B (158 °C), MS curves show that the CO<sub>2</sub> formation rate is still low, but the CO coverage is reduced (−8%), which is explained by the shift of adsorption/desorption equilibrium by heating. The spectral shape of C 1s becomes broad, due to a change of adsorption structure. The CO<sub>2</sub> formation rate is almost zero from room temperature to 165 °C. It suggests that the CO overlayer hinders dissociative adsorption of O<sub>2</sub> and the CO<sub>2</sub> formation rate is limited by the O<sub>2</sub> adsorption.

Above the catalytic light-off (> 165 °C), the CO<sub>2</sub> formation rate is increased about 6-times with respect to the CO-poisoning condition. Under this condition, adsorbed CO rapidly reacts with O and desorbs as CO<sub>2</sub>, since the C 1s level shows no CO peak. Since CO is not stably exist on the surface, the three new components appeared in Pd 3d<sub>5/2</sub> level are associated with the O-induced surface state(s). The binding energies of them indicate formation of the chemisorbed O phase (denoted as Pd-O). PdO bulk oxide (denoted as BO) is also detected in the higher binding energy side. Thus the surface is covered mainly by the chemisorbed O and a small amount of the bulk oxide also coexists. The corresponding O 1s level supports the assignments, where distinct three peaks are detected (not shown). Because the MS measurement indicates a high catalytic activity under this condition, the chemisorbed O phase reacts with CO. This is a contrary result compared with the Pd(111) and Pd(100) surfaces, where the surface oxide accelerates the reaction rate via the MvK mechanism. The CO<sub>2</sub> formation rate is gradually decayed with increasing the temperature above the catalytic light-off temperature. At point D, Pd 3d<sub>5/2</sub> level shows the reduction of chemisorbed O on the surface. It indicates that the amount of chemisorbed O on the surface is a key factor for the CO<sub>2</sub> formation rate. The slight decay of reactivity

above the catalytic light-off temperature is accompanied by a growth of the bulk oxide. This suggests that the bulk oxide does not contribute to the CO oxidation reaction.



**Figure 4.8.** In-situ monitoring of catalytic CO oxidation on Pd(110) surface as a function of temperature (a). Here the  $\text{O}_2$  and  $\text{CO}$  pressures are 200 mTorr and 20 mTorr, respectively. Above the catalytic light-off, the  $\text{CO}_2$  intensity increased, however further heating results in a gradual decay of the performance. Labels A, B, C, and D correspond to temperature where XP spectra were recorded. Corresponding Pd  $3d_{5/2}$  and C 1s XP spectra taken under the reaction conditions (b and c). Adapted with permission from Ref. P-4. Copyright (2013) American Chemical Society.

#### 8.4 Summary and Discussion

In summary, in-situ monitoring of catalytic CO oxidation was performed on Pd(100), (111) and (110) single-crystal surfaces to reveal the relationship between the surface chemical state and catalytic activity. It is found that the CO<sub>2</sub> formation rate has a great dependence on surface chemical states. A large amount of CO molecules fully cover the metallic surfaces at lower temperatures, The CO poisoning suppresses the efficient catalytic reaction, resulting in a low CO<sub>2</sub> formation rate. At higher temperatures above the light-off temperature the adsorbed CO molecules are replaced by the chemisorbed O or the surface oxide phases. Above the catalytic light-off, the O-Pd-O tri-layer surface oxide or the dense O chemisorption layer are formed on the surfaces and the CO oxidation rate is drastically enhanced. On the (111) and (100) surfaces, it was found that the upper-side O species of the surface oxide play a key role to the high activity (MvK mechanism). It is noted that the upper-side O species is much more reactive compared to the oxygen located underneath the surface Pd layer. While the active oxygen on the (110) surface is in a chemisorbed state different from those on the other two surfaces. Since all the O species adsorb on the reconstructed Pd(110) surface with keeping a chemisorbed state, the CO oxidation reaction proceeds via the conventional LH mechanism on a metallic surface. The light-off temperature depends on the surface orientation, but the active surfaces are covered by dense O phases regardless of the chemical condition; 0.8 ML, (111); 1.0 ML, (100); 0.86 ML, (110). The dense O phases on the surface reduce the adsorption energy per O atom, suggesting that the reaction proceeds with a small activation barrier. The experimental results evidence that both of the MvK and the LH mechanisms can be responsible for the CO oxidation reaction under NAP conditions.



## References

- [1] Campbell, C. T.; Ertl, G.; Kuipers, H.; Segner, J. *J. Chem. Phys.* **1980**, *73*, 5862.
- [2] Winterlin, J.; Völkening, S.; Janssens, T. V. W.; Zambelli, T.; Ertl, G. *Science* **1997**, *278*, 1931.
- [3] Nakai, I.; Kondoh, H.; Amemiya, K.; Nagasaka, M.; Shimada, T.; Yokota, R.; Nambu, A.; Ohta, T. *J. Chem. Phys.* **2005**, *122*, 134709.
- [4] Nakai, I.; Kondoh, H.; Shimada, T.; Resta, A.; Andersen, J. N.; Ohta, T. *J. Chem. Phys.* **2006**, *124*, 224712.
- [5] Nagasaka, M.; Kondoh, H.; Nakai, I.; Ohta, T. *J. Chem. Phys.* **2007**, *126*, 044704.
- [6] Nagarajan, S.; Thirunavukkarasu, K.; Gopinath, C. S. *J. Phys. Chem. C* **2009**, *113*, 7385.
- [7] Zheng, G.; Altman, E. I. *J. Phys. Chem. B* **2002**, *106*, 1048.
- [8] Hendriksen, B. L. M.; Frenken, J. W. M. *Phys. Rev. Lett.* **2002**, *89*, 046101.
- [9] Hendriksen, B. L. M.; Bobaru, S. C.; Frenken, J. W. M. *Surf. Sci.* **2004**, *552*, 229.
- [10] Ackerman, M. D.; Pedersen, T. M.; Hendriksen, B. L. M.; Robach, O.; Bobaru, S. C.; Popa, I.; Quiros, C.; Kim, H.; Hammer, B.; Ferrer, S. et al., *Phys. Rev. Lett.* **2005**, *95*, 255505.
- [11] Gustafson, J.; Westerström, R.; Balmes, O.; Resta, A.; van Rijn, R.; Torrelles, X.; Herbschleb, C. T.; Frenken, J. W. M.; Lundgren, E. *J. Phys. Chem. C* **2010**, *114*, 4580.
- [12] van Rijn, R.; Balmes, O.; Resta, A.; Wermeille, D.; Westerström, R.; Gustafson, J.; Felici, R.; Lundgren, E.; Frenken, J. W. M. *Phys. Chem. Chem. Phys.* **2011**, *13*, 13167.
- [13] Hendriksen, B. L. M.; Ackermann, M. D.; van Rijn, R.; Stoltz, D.; Popa, I.; Balmes, O.; Resta, A.; Wermeille, D.; Felici, R.; Ferrer, S.; Frenken, J. W. M. *Nat. Chem.* **2010**, *2*, 730.
- [14] Blume, R.; Hävecker, M.; Zafeirotos, S.; Teschner, D.; Kleimenov, E.; Knop-Gericke, A.; Schlögl, R.; Barinov, A.; Dudin, P.; Kiskinova, M. *J. Catal.* **2006**, *239*, 354.
- [15] Toyoshima, R.; Yoshida, M.; Monya, Y.; Kousa, Y.; Suzuki, K.; Abe, H.; Mun, B. S.; Amemiya, K.; Mase, K.; Kondoh, H. *J. Phys. Chem. C* **2012**, *116*, 18691.
- [15] Butcher, D. R.; Grass, M. E.; Zeng, Z.; Aksoy, F.; Bluhm, H.; Li, W.-X.; Mun, B. S.; Somorjai, G. A.; Liu, Z. *J. Am. Chem. Soc.* **2011**, *133*, 20319.
- [16] Chen, M. S.; Cai, Y.; Gath, K. K.; Axnanda, S.; Goodman, D. W. *Surf. Sci.* **2007**, *601*, 5326.
- [17] Gao, F.; McClure, S. M.; Cai, Y.; Gath, K. K.; Wang, Y.; Chen, M. S.; Guo, Q. M.; Goodman, D. W. *Surf. Sci.* **2009**, *603*, 65.
- [17] Gao, F.; Wang, Y.; Cai, Y.; Goodman, D. Y. *J. Phys. Chem. C* **2009**, *113*, 174.
- [18] Chen, M.; Wang, X. V.; Zhang, L.; Tang, Z.; Wan, H. *Langmuir* **2010**, *26*, 18113.
- [19] Chung, J. Y.; Aksoy, F.; Grass, M. E.; Kondoh, H.; Ross Jr, P.; Liu, Z.; Mun, B. S. *Surf. Sci. Lett.* **2009**, *603*, L35.
- [20] Zhang C. J.; Hu P. *J. Am. Chem. Soc.* **2001**, *123*, 1166.
- [21] Gong, X.-Q.; Liu, Z.-P.; Raval, R.; Hu, P. *J. Am. Chem. Soc.* **2004**, *126*, 8.
- [22] Hirvi, J. T.; Kinnunen, T.-J. J.; Suvanto, M.; Pakkanen, T. A.; Nørskov, J. K. *J. Chem. Phys.* **2010**, *133*, 084704.
- [23] Li, W. X.; Hammer, B. *Chem. Phys. Lett.* **2005**, *409*, 1.
- [24] Sun, D.; Gu, X. K.; Ouyang, R.; Su, H. Y.; Fu, Q.; Bao, X.; Li, W.-X. *J. Phys. Chem. C* **2012**, *116*, 7491.
- [24] Rogal, J.; Reuter, K.; Scheffler, M. *Phys. Rev. Lett.* **2007**, *98*, 046101.
- [25] Rogal, J.; Reuter, K.; Scheffler, M. *Phys. Rev. B* **2007**, *75*, 205433.
- [26] Rogal, J.; Reuter, K.; Scheffler, M. *Phys. Rev. B* **2008**, *77*, 155410.
- [27] Mars, P.; van Krevelen, D. W. *Chem. Eng. Sci.* **1954**, *3*, 41.
- [28] Vu, D. T.; Mitchell, K. A. R.; Warren, O. L.; Thiel, P. A. *Surf. Sci.* **1994**, *318*, 129.
- [29] Saïdy, M.; Warren, O. L.; Thiel, P. A.; Mitchell, K. A. R. *Surf. Sci.* **2001**, *494*, L799.
- [30] Todorova, M.; Lundgren, E.; Blum, V.; Mikkelsen, A.; Gray, S.; Gustafson, J.; Borg, M.; Rogal, J.; Reuter, K.; Andersen, J. N. et al., *Surf. Sci.* **2003**, *541*, 101.
- [31] Kostelník, P.; Seriani, N.; Kresse, G.; Mikkelsen, A.; Lundgren, E.; Blum, V.; Šikola, T.; Varga, P.; Schmid, M. *Surf. Sci.* **2007**, *601*, 1574.
- [32] Westerström, R.; Messing, M. E.; Blomberg, S.; Hellman, A.; Grönbeck, H.; Gustafson, J.; Martin, N. M.; Balmes, O.; van Rijn, R.; Andersen, J. N. et al., *Phys. Rev. B* **2011**, *83*, 115440.
- [33] Surnev, S.; Sock, M.; Ramsey, M. G.; Netzer, F. P.; Wiklund, M.; Borg, M.; Andersen, J. N. *Surf.*

- Sci.* **2000**, *470*, 171-185.
- [34] Kaichev, V. V.; Prosvirin, I. P.; Bukhtiyarov, V. I.; Unterhalt, H.; Rupprechter, G.; Freund, H. J. *J. Phys. Chem. B* **2003**, *107*, 3522-3527.
- [35] Chen, M. S.; Cai, Y.; Gath, K.K.; Axnanda, S.; Goodman, D.W. *Surf. Sci.* **2007**, *601*, 5326-5331.
- [36] Leisenberger, F. P.; Koller, G.; Sock, M.; Surnev, S.; Ramsey, M. G.; Netzer, F. P.; Klötzer, B.; Hayek, K. *Surf. Sci.* **2000**, *445*, 380-393.
- [37] Lundgren, E.; Kresse, G.; Klein, C.; Borg, M.; Andersen, J. N.; De Stantis, M.; Gauthier, Y.; Konvicka, C.; Schmid, M.; Varga, P. *Phys. Rev. Lett.* **2002**, *88*, 246103-246106.
- [38] Ketteler, G.; Ogletree, D. F.; Bluhm, H.; Liu, H.; Hebenstreit, E. L. D.; Salmeron, M. *J. Am. Chem. Soc.* **2005**, *127*, 18269-18273.
- [39] Gabasch, H.; Unterberger, W.; Hayek, K.; Klötzer, B.; Klemenov, E.; Teschner, D.; Zafeiratos, S.; Hävecker, M.; Knop-Gericke, A.; Schlögl, R. et al., *Surf. Sci.* **2006**, *600*, 2980-2989.
- [40] Tanaka, H.; Yoshinobu, J.; Kawai, M. *Surf. Sci. Lett.* **1995**, *327*, L505.
- [41] Bennett, R. A.; Poulston, S.; Jones, I. Z.; Bowker, M. *Surf. Sci.* **1998**, *401*, 72.
- [42] Kralj, M.; Pertram, T.; Seriani, N.; Mittendorfer, F.; Krupski, A.; Becker, C.; Wandelt, K. *Surf. Sci.* **2008**, *602*, 3706.
- [43] Westerström, R.; Weststrate, C. J.; Gustafson, J.; Mikkelsen, A.; Schnadt, J.; Andersen, J. N.; Lundgren, E.; Seriani, N.; Mittendorfer, F.; Kresse, G. et al., *Phys. Rev. B* **2009**, *80*, 125431.
- [44] Westerström, R.; Weststrate, C. J.; Resta, A.; Mikkelsen, A.; Schnadt, J.; Andersen, J. N.; Lundgren, E.; Schmid, M.; Seriani, N.; Harl, J. et al., *Surf. Sci.* **2008**, *602*, 2440.

## Chapter 5

### Concluding Remarks

---

PGMs exhibit catalytic activities for various chemical reactions. PGM-based TWC is widely used to convert harmful chemical compounds (CO, NO<sub>x</sub> and hydrocarbons) included in exhaust gas. To understand the reaction mechanism of catalytic conversion of CO and NO<sub>x</sub> on PGM surfaces is an important topic of surface science. Single crystal surfaces of PGMs are regarded as prototypical model catalysts for CO oxidation and NO<sub>x</sub> reduction. Although studies with surface science techniques under UHV conditions have improved our knowledge of the reaction process at the atomic level, the pressure gap prevents us from understanding the realistic phenomena proceeding under atmospheric conditions. The ambient pressure may change the surface chemical state and further catalytic reaction mechanism.

In this thesis, the physicochemical interactions between surface and molecules at elevated pressures up to sub-Torr regime were investigated using in-situ spectroscopic techniques (XPS and IRAS). Here the adsorption of CO and NO molecules on the surfaces was paid particular attention, because it is the first step for the catalytic reaction. Then the surface chemical condition and catalytic activity under the reaction conditions were observed in-situ. The DFT simulations were also employed to obtain the atomic-level understanding of structures and energetics. Spectroscopic data are spatially and temporally averaged information from ensembles on a surface, whereas theoretical simulations can shed light on each geometric and electronic structure of interest. Experimental and theoretical results were compared to understand adsorption and reactions of small molecules on the PGM surfaces.

The spectroscopic study conducted under near ambient pressure conditions reduces the pressure gap problem. The coverage of CO on Pt and Pd surfaces were reversibly controlled by the background pressures with forming a dense overlayer. The NO molecule on the Rh surface partially dissociates to nitrogen and oxygen atoms, and form a periodic coadsorption structure with the atomic species under a high-pressure NO exposure via chemical reaction. The alloying of two metal elements sometimes improves the catalytic activity, which stems from changes in the surface electronic and geometric structures. The Pd-Au bimetallic surface provides three types of isolated Pd site (hollow, bridge and top) for CO adsorption. Occupancy of each adsorption site depends on the CO pressure. Particularly high-pressure exposure induces the site switching of adsorbed CO to energetically unfavorable sites, which is associated with the high chemical potential of gas-phase CO under equilibrium with the adsorbed CO.

The catalytic CO oxidation on low-index Pd surfaces was studied with in-situ XPS observations

under near ambient pressure conditions. The results evidenced that both of chemisorbed oxygen and surface oxide can be reactive. The MvK mechanism, which is regarded as less effective under UHV conditions, seems to operate under certain conditions. The dense oxygen phases formed under the reaction condition provide reactive oxygen atoms to the adsorbed CO. It suggests that the density of oxygen is a more important factor to the catalytic activity rather than the chemical phase of surface oxygen.

As a conclusion, it was revealed that the background pressure plays decisive roles in forming adsorption structures and surface chemical states and hence in controlling active phase for the catalytic reaction. These findings obtained from high-pressure surface science technique measurements contribute to the fundamental understanding of heterogeneous catalysis.

In this thesis, the molecular adsorption and chemical reaction under steady state conditions on low-index single crystal surfaces were studied. Here the molecules are assumed to adsorb mainly on terraces defined by the surface orientation. The differences in adsorption and reaction properties are attributed to differences in structures of terraces. Although this is a common and conventional approach in surface science, this kind of view sometimes does not work well in understanding the real catalysts, because they have many irregular sites like steps and defects which act as active sites. Vicinal single crystal surfaces, e.g. fcc(553), (332) and (211) faces, are models to study the irregular-site-specific phenomena.<sup>1,2</sup> Some unique behaviors of step sites have been found using XPS under UHV condition, whereas the number of such studies under equilibrium with high-pressure gas is limited.<sup>3</sup> The use of cylinder-shape single crystals, which have various surfaces continuously arrayed on the cylinder, will enhance studies on surface-orientation dependence of a reaction. Moreover it may give insight into cooperative behavior of steps and terraces with different orientation; for example, a step acts as active center, whereas a terrace as reactant storage.

The adsorption behaviors of CO and NO were independently studied for simplicity in the present study. And the catalytic surface reaction studied here was limited to the CO oxidation only. However on the real catalyst surfaces several elementary steps proceed in parallel. If CO and NO are supplied to the surface at once, the adsorption of reactants onto the surface should become competitive.<sup>4</sup> The equilibrium surface coverage should change depending on adsorption probability and partial pressure of each species. There is a possibility that a new equilibrium surface and/or a new reaction mechanism might contribute to the reaction.

The present in-situ experimental setups gave temporally averaged data under the reaction conditions. Temporally averaged information (hundreds millisecond per data point) refers the thermodynamically stable species on the surface. Transient species cannot be detected due to a short surface residence time. Time-resolved observation with the pump-and-probe technique enabled to observe molecular dynamics of such a short-lived species involved in a surface reaction directly.<sup>5</sup> However, this sort of experiments has been mostly conducted under UHV conditions. In future, the

combination of the high-pressure-compatible spectroscopy and the pump-and-probe technique will advance our understanding of dynamic processes involved in catalytic surface reactions on practical catalysts.



## References

- [1] Wang, J. G.; Li, W. X.; Borg, M.; Gustafson, J.; Mikkelsen, A.; Pedersen, T. M.; Lundgren, E.; Weissenrieder, J.; Klikovits, J.; Schmid, M.; Hammer, B.; Andersen, J. N. *Phys. Rev. Lett.* **2005**, *95*, 256102.
- [2] Westerström, R.; Gustafson, J.; Resta, A.; Mikkelsen, A.; Andersen, J. N.; Lundgren, E.; Schmid, M.; Klikovits, J.; Varga, P.; Ackermann, M. D.; Frenken, J. W. M.; Kasper, N.; Stierle, A. *Phys. Rev. B* **2007**, *76*, 155410.
- [3] Tao, F.; Dag, S.; Wang, L.-W.; Liu, Z.; Butcher, D. R.; Bluhm, H.; Salmeron, M.; Somorjai, G. A. *Science* **2010**, *327*, 850.
- [4] Requejo, F. G.; Hebenstreit, E. L. D.; Ogletree, D. F.; Salmeron, M. *J. Catal.* **2004**, *226*, 83.
- [5] Dell'Angela, M.; Anniyev, T.; Beye, M.; Coffee, R.; Föhlisch, A.; Gladh, J.; Katayama, T.; Krupin, O.; LaRue, J.; Møgelhøj, A.; Nordlund, D.; Nøskov, J. K.; Öberg, H.; Ogasawara, H.; Öström, H.; Pettersson, L. G. M.; Schlotter, W. F.; Sellberg, J. A.; Sorgenfrei, F.; Turner, J. J.; Wolf, M.; Wurth, W.; Nilsson, A. *Science* **2013**, *339*, 6125.



## Publications

Most of the works described in Chapter 3 and Chapter 4 have been published in the following scientific papers.

- [P-1] Toyoshima, R.; Yoshida, M.; Monya, Y.; Kousa, Y.; Suzuki, K.; Abe, H.; Mun, B. S.; Mase, K.; Amemiya, K.; Kondoh, H. In Situ Ambient Pressure XPS Study of CO Oxidation Reaction on Pd(111) Surfaces. *The Journal of Physical Chemistry C* **2012**, *116* (35), 18691–18697.
- [P-2] Toyoshima, R.; Yoshida, M.; Monya, Y.; Suzuki, K.; Mun, B. S.; Amemiya, K.; Mase, K.; Kondoh, H. Active Surface Oxygen for Catalytic CO Oxidation on Pd(100) Proceeding under Near Ambient Pressure Conditions. *The Journal of Physical Chemistry Letters* **2012**, *3* (21), 3182–3187.
- [P-3] Toyoshima, R.; Yoshida, M.; Monya, Y.; Suzuki, K.; Amemiya, K.; Mase, K.; Mun, B. S.; Kondoh, H. Photoelectron Spectroscopic Study of CO and NO Adsorption on Pd(100) Surface under Ambient Pressure Conditions. *Surface Science* **2013**, *615* (1), 33–40.
- [P-4] Toyoshima, R.; Yoshida, M.; Monya, Y.; Suzuki, K.; Amemiya, K.; Mase, K.; Mun, B. S.; Kondoh, H. In Situ Photoemission Observation of Catalytic CO Oxidation Reaction on Pd(110) under Near-Ambient Pressure Conditions: Evidence for the Langmuir–Hinshelwood Mechanism. *The Journal of Physical Chemistry C* **2013**, *117* (40), 20617–20624.
- [P-5] Toyoshima, R.; Yoshida, M.; Monya, Y.; Suzuki, K.; Amemiya, K.; Mase, K.; Mun, B. S.; Kondoh, H. A High-Pressure-Induced Dense CO Overlayer on a Pt(111) Surface: a Chemical Analysis Using In situ Near Ambient Pressure XPS. *Physical Chemistry Chemical Physics* **2014**, *16* (43), 23564–23567.
- [P-6] Toyoshima, R.; Yoshida, M.; Monya, Y.; Suzuki, K.; Amemiya, K.; Mase, K.; Mun, B. S.; Kondoh, H. High-Pressure NO-Induced Mixed Phase on Rh(111): Chemically Driven Replacement. *The Journal of Physical Chemistry C* **2015**, *119* (6), 3033–3039.
- [P-7] Toyoshima, R.; Hiramatsu, N.; Yoshida, M.; Amemiya, K.; Mase, K.; Mun, B. S.; Kondoh, H. CO Adsorption on Pd-Au Alloy Surface: Reversible Adsorption Site Switching Induced by High-Pressure CO. *The Journal Physical Chemistry C* **2016**, *120* (1), 416–421.



## **Acknowledgements**

I would like to show my appreciation to the people who have supported to the thesis, especially Prof. Kondoh and Dr. Yoshida. The experiments were performed under the approval of the Photon Factory Program Advisory Committee (PF PAC 2010G151, 2012G093, 2012S2-006 and 2015S2-008). These studies were supported by the Grants-in-Aid for scientific research (Nos. 20245004 and 26248008) and the MEXT-Supported Program for the Strategic Research Foundation at Private Universities, 2009-2013. I acknowledge the support from JSPS Research Fellowship for Young Scientist.



# Appendix A

## Fermi's golden rule

Fermi's golden rule is the basic principle for transition from an eigenstate  $i$  to  $f$ . It is derived from the time-dependent Schrödinger equation (eq. A1 and A2).

$$i\hbar \frac{\partial}{\partial t} |\psi(t)\rangle = H'(t)|\psi(t)\rangle, \quad (\text{A1})$$

$$|\psi(t)\rangle = \sum_m c_m(t) |\varphi_m\rangle \exp\left(\frac{-iE_m t}{\hbar}\right). \quad (\text{A2})$$

Here the wave function  $|\psi(t)\rangle$  is an orthonormal system.  $H'(t)$  is a time-dependent Hamiltonian.  $c_m(t)$  is time-dependent expansion coefficient,  $E_m$  is corresponding eigenvalue. By multiplying the term  $\exp(iE_n t/\hbar)\langle\varphi_n|$  from the left side, and continuous orthogonalization, the eq. A2 is transformed to A3.

$$i\hbar \frac{\partial}{\partial t} c_n(t) = \sum_m c_m(t) \langle\varphi_n|H'|\varphi_m\rangle \exp\left\{\frac{i(E_n - E_m)t}{\hbar}\right\}. \quad (\text{A3})$$

If initially it is assumed that  $|\psi(t=0)\rangle = |\varphi_i\rangle$ , the expansion coefficient of a final state  $|\varphi_f\rangle$  at particular time  $t$  ( $i \rightarrow f$  transition) is represented as follows;

$$\frac{d}{dt} c_f(t) = \frac{1}{i\hbar} \langle\varphi_f|H'|\varphi_i\rangle \exp\left\{\frac{i(E_f - E_i)t}{\hbar}\right\}, \quad (\text{A4})$$

$$c_f(t) = \frac{1}{i\hbar} \int_0^t \langle\varphi_f|H'|\varphi_i\rangle \exp\left\{\frac{i(E_f - E_i)t'}{\hbar}\right\} dt' \quad (\text{A5})$$

$$= \langle\varphi_f|H'|\varphi_i\rangle \frac{1 - \exp\left\{\frac{i(E_f - E_i)t}{\hbar}\right\}}{E_f - E_i}.$$

Moreover, The existence probability at that time is expressed by the  $|c_f(t)|^2$ .

$$|c_f(t)|^2 = |\langle\varphi_f|H'|\varphi_i\rangle|^2 \left[ \frac{2 \sin \frac{t}{2\hbar} (E_f - E_i)}{E_f - E_i} \right]^2. \quad (\text{A6})$$

Then, the eq. A6 is transformed to the eq. A7 to clarify the features.

$$\left[ \frac{2 \sin \frac{t}{2\hbar} (E_f - E_i)}{E_f - E_i} \right]^2 = \frac{\pi t}{\hbar^2} F(s), \quad (\text{A7})$$

$$F(s) = \frac{\sin^2 ts}{\pi t s^2}, \quad s = \frac{E_f - E_i}{2\hbar}.$$

The equation  $F(s)$  becomes to the delta function at  $t \rightarrow \infty$ . Therefore the transition probability per unit time between interested eigenstates  $i \rightarrow f$  results in as follow;

$$\lim_{t \rightarrow \infty} \frac{1}{t} |c_f(t)|^2 = \lim_{t \rightarrow \infty} \frac{\pi}{\hbar^2} F(s) |\langle \varphi_f | H' | \varphi_i \rangle|^2 = \frac{2\pi}{\hbar} |\langle \varphi_f | H' | \varphi_i \rangle|^2 \delta(E_f - E_i). \quad (\text{A8})$$

Here, it is assumed that the  $H'(t)$  is a kind of photon (the electric dipole transition).

$$H'(t) = \sum_j q_j z_j E_0 \exp i\omega t. \quad (\text{A9})$$

$$\langle \varphi_f | H'(t) | \varphi_i \rangle = \langle \varphi_f | \sum_j q_j z_j E_0 | \varphi_i \rangle \exp i\omega t. \quad (\text{A10})$$

The eq. A10 is assigned to the eq. A5, then the existence and transition probabilities are estimated to the following equations.

$$|c_f(t)|^2 = \left| \langle \varphi_f | \sum_j q_j z_j E_0 | \varphi_i \rangle \right|^2 \left[ \frac{2 \sin \frac{t}{2\hbar} (E_f - E_i - \hbar\omega)}{E_f - E_i - \hbar\omega} \right]^2, \quad (\text{A11})$$

$$T_{i \rightarrow f} = \lim_{t \rightarrow \infty} \frac{1}{t} |c_f(t)|^2 = \frac{2\pi}{\hbar} \left| \langle \varphi_f | \sum_j q_j z_j E_0 | \varphi_i \rangle \right|^2 \delta(E_f - E_i - \hbar\omega) \quad (\text{A12})$$

This means the transition is allowed, when the transition moment is not equal to zero and the energy conservation law is satisfied.

Besides, the profile function  $F(s)$  eq. A7 describes an important aspect of the transition between interested eigenstates. Figure A1 shows the graph of function. Here the variable  $s$  is the energy discrepancy. If the lift time of excitation is infinity ( $t \rightarrow \infty$ ), the energy conservation law is completely satisfied. However it is finite, for example  $10^{-15}$  s for electron excitation, in real systems. Therefore there is an excitation probability at  $S \neq 0$ . This is the origin that the experimental spectral line shape intrinsically has a width (Lorentzian width).

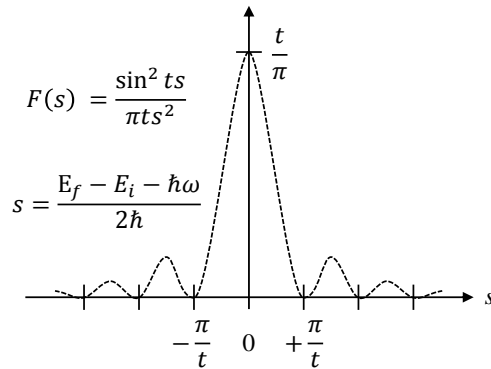


**Figure A1.** The graph of function  $F(s)$ .

## Appendix B

### Photoionization cross-section

The photoionization intensity  $I$  per unit time and unit area is defined as follows;

$$I = I_0 N \sigma_{nl}, \quad (\text{B1})$$

where  $I_0$  is incident X-ray intensity,  $N$  is the number of atom per unit area and  $\sigma_{nl}$  is photoionization cross-section labeled by principal and azimuthal quantum number  $n$  and  $l$ . The photoionization cross-section from an eigenstate  $i$  to  $f$  per unit volume is described as follows;

$$\frac{d\sigma_{nl}}{d\Omega} = \frac{C m_e}{g_i \hbar^2} \left| \langle \varphi_f | \sum_j q_j z_j | \varphi_i \rangle \right|^2, \quad (\text{B2})$$

where,  $g_i$  is degree of degeneracy of initial state  $i$ ,  $C$  is a constant,  $m_e$  is electron mass and  $\hbar$  is Planck constant. Here the electric dipole transition is considered. This means the photoemission intensity depends on the size of transition moment.

In the case of photoemission process, the initial state  $i$  is a core-orbital, whereas the final state  $f$  is a plane wave (free electron). The wave function of plane wave is expanded as follows;

$$|\varphi_f\rangle = \exp(i\mathbf{k} \cdot \mathbf{r}) = \exp(ikr \cos \theta) = A \sum_{l=0}^{\infty} (2l+1) i^l j_l(kr) P_l(\cos \theta). \quad (\text{B3})$$

The  $\mathbf{k}$  is a wave vector and  $\mathbf{r}$  is a position vector. The third form is gained via the partial wave expansion, where  $A$  is a constant, the  $j_l(kr)$  is the sphere Bessel function and  $P_l(\cos \theta)$  is the Legendre polynomial. It indicates the plane wave consists of all azimuthal quantum number  $l$ . Therefore the photoemission process is allowed for all core-orbitals. It guarantees that every core-orbital can be observed by XPS.

$$\langle \exp(i\mathbf{k} \cdot \mathbf{r}) | \sum_j q_j z_j | \varphi_i \rangle \neq 0. \quad (\text{B4})$$



## Appendix C

### Surface free energy modified for alloy material

The surface free energy  $\gamma$  is appropriate method to discuss the surface structure at given conditions. The basics of the theory is described in section 2.5.3. If the bimetallic material is applied to the theory, some additional procedures are requested. As discussed above, it is defined as normalized Gibbs free energy by surface area  $A$  at a given temperature ( $T$ ) and a pressure ( $p$ ). The surface free energy of bimetallic material is written as follows;

$$\begin{aligned}\gamma(T, \{p_j\}, \{N_i\}, \{N_j\}) &= \frac{1}{A} \left[ G(T, \{p_j\}, \{N_i\}, \{N_j\}) - \sum_i N_i \mu_i - \sum_j N_j \mu_j \right] \quad (C1) \\ &= \frac{1}{A} \left[ G(T, \{p_j\}, N_A, N_B, \{N_j\}) - N \chi_A \mu_A - N \chi_B \mu_B - \sum_j N_j \mu_j \right].\end{aligned}$$

Here the bimetallic material consists of two metal elements A and B.  $N$  is the total number of substrate atom,  $\chi_A$  and  $\chi_B$  are the mole fractions of metal element A and B, respectively, i.e.  $\chi_A + \chi_B = 1$ .  $\mu_A$ ,  $\mu_B$  and  $\mu_j$  are the corresponding chemical potentials.

The chemical potential of bulk reservoir of the alloy ( $\mu_{\text{bulk}}$ ) can be expressed by the chemical potentials of metal species included in the alloy ( $\mu_A$  and  $\mu_B$ ) as shown below.  $\chi_{A(\text{bulk})}$  and  $\chi_{B(\text{bulk})}$  are the mole fraction of the bulk alloy. However, surface segregation causes a difference in the surface and bulk stoichiometries, which alters  $\mu_A$ ,  $\mu_B$  and  $\mu_{\text{bulk}}$ , and hence the difference of the chemical potentials  $\Delta\mu_{A-B}$  ( $= \mu_A - \mu_B$ ). Destruction of the bulk alloy proceeds when the chemical potentials of each component exceeds the potential of pure metal,  $\mu_A > \mu_{A,\text{pure}}$  or  $\mu_B > \mu_{B,\text{pure}}$ . The range of  $\Delta\mu_{A-B}$  where the alloy can be stably maintained is described as follows;

$$\mu_{\text{bulk}} = \chi_{A(\text{bulk})} \mu_A + \chi_{B(\text{bulk})} \mu_B = \chi_{A(\text{bulk})} (\mu_A - \mu_B) + \mu_B \quad (C2)$$

$$= \chi_{A(\text{bulk})} \Delta\mu_{A-B} + \mu_B,$$

$$\Delta\mu_{A-B(\text{A-rich})} \geq \Delta\mu_{A-B} \geq \Delta\mu_{A-B(\text{B-rich})}, \quad (C3)$$

$$\Delta\mu_{A-B(\text{A-rich})} = \left( \frac{\mu_{A,\text{pure}} - \mu_{\text{bulk}}}{1 - \chi_{A(\text{bulk})}} \right), \quad (C4)$$

$$\Delta\mu_{A-B(\text{B-rich})} = \left( \frac{\mu_{\text{bulk}} - \mu_{B,\text{pure}}}{1 - \chi_{B(\text{bulk})}} \right). \quad (C5)$$

Taking into accounts of above equations, eq. C1 is rewritten as follows;

$$\gamma = \frac{1}{A} \left[ E_{j/AB} - N E_{\text{bulk}} - N \Delta\mu_{A-B} (\chi_A - \chi_{A(\text{bulk})}) - N_j \mu_j(T, p_j) \right] \quad (C6)$$



# Appendix D

## Details of CLS simulations

The CLS ( $E_{\text{CLS}}$ ) is determined by the energy change of core-BEs between the interested ( $BE$ ) and referenced ( $BE_{\text{ref.}}$ ) atoms, which indicates the difference of chemical environment.

$$E_{\text{CLS}} = BE - BE_{\text{ref.}} \quad (\text{D1})$$

The BE is defined as the energy to remove an electron from an interested core orbital (Koopmans' theorem). It is necessary to get accurate BE values for reliable CLS simulation. The simulated absolute BE includes some artificial effects, which comes from the basis of DFT, while the CLS (relative BE) cancels out these effects, leading to a good agreement with experimental results. There are three ways to estimate the BE. The Initial State (IS) approximation assumes that the BE is the eigenvalue of interested core orbital ( $-\varepsilon$ ) without electron excitation. Whereas, the final state (FS) approximation is more complex, here the BE is defined as the difference of total electron energies between unexcited ( $n_i$ ) and excited ( $n_i - 1$ ) systems, where the electron is excited from interested core orbital to the valence for the electro-neutrality. It can take into account of the electron relaxation/screening process, but needs somewhat high computational cost.

$$BE_i^{\text{IS}} = -\varepsilon_i^{\text{IS}}, \quad (\text{D2})$$

$$BE_i^{\text{FS}} = [E(n_i - 1) - E(n_i)]. \quad (\text{D3})$$

The transition state (TS) approximation is widely applied to simulate the BE. It is estimated from the calculated eigenvalue, but includes the so-called FS effect. In DFT, the total electron energy is the integral of calculated eigenvalue (Janak's theorem).

$$\varepsilon_i = \partial E / \partial n_i, \quad (\text{D4})$$

When a fractional electron  $x$  is excited, the corresponding total energy  $E(q_i = n_i - x)$  and an eigenvalue  $F(x)$  are written as eq. D5 and D6, via the Taylor expansion.

$$E(q_i = n_i - x) = E(n_i) + \lambda_1 x + \lambda_2 x^2 + \dots + \lambda_m x^m \quad (\text{D5})$$

$$\lambda_m = (-1)^m E^{(m)}(n_i) / m!$$

$$F(x) = -\varepsilon_i(x) = \lambda_1 + 2\lambda_2 x + \dots + m\lambda_m x^{m-1} + \dots \quad (\text{D6})$$

The TS approximation assumes the half electron is excited from the core orbital to the valence band, and the BE is represented by the eigenvalue. The energy difference compared to the FS method is estimated in eq. D8. The TS approximation does not treat the electron relaxation, but gives an adequate result.

$$BE_i^{\text{TS}} = -\varepsilon_i\left(\frac{1}{2}\right) = \lambda_1 + \lambda_2 + \frac{3}{4}\lambda_3 + \dots + \frac{m}{2^{m-1}}\lambda_m + \dots \quad (\text{D7})$$

$$\delta^{\text{TS}} = BE_i^{\text{FS}} - BE_i^{\text{TS}} = \sum_{m=1} \lambda_m - BE_i^{\text{TS}} = \frac{1}{4}\lambda_3 + \dots + \frac{2^{m-1} - m}{2^{m-1}}\lambda_m + \dots \quad (\text{D8})$$